Dissertation
submitted to the
Combined Faculty of Mathematics, Engineering and Natural Sciences
of Heidelberg University, Germany
for the degree of
Doctor of Natural Sciences

Put forward by
Quentin Coppée
born in: Brussels, Belgium
Oral examination: July 15th, 2025

Characterising the suppression of non-radial modes in red giants

Quentin Coppée

SUPERVISOR

Prof. Dr. Ir. Saskia Hekker

EXAMINATION COMMITTEE

Prof. Dr. Ir. Saskia Hekker (referee)

Prof. Dr. Simon Glover (referee)

Prof. Dr. Jochen Heidt

Prof. Dr. Astrid Eichhorn

Summary

Magnetic fields are thought to play a significant role in various phenomena in the Universe, in particular in the evolution and the structure of stars. With asteroseismology, it is possible to probe the inner structure of stars. In this thesis, we investigate the properties of the oscillations of red giants that show signs of energy loss. We observationally constrained the mechanism causing this energy loss and found that it is consistent with the predicted effect of magnetic field in the core of the red giant. Using recent developments, we were also able to observe frequency shifts due to a magnetic field in the core of stars. We analysed stars with both magnetic frequency shifts and energy loss in the oscillations and showed that both phenomena can be explained by a magnetic field with the same field strength located in the core of the stars.

Zusammenfassung

Es wird angenommen, dass Magnetfelder bei verschiedenen Phänomenen im Universum eine wichtige Rolle spielen, insbesondere bei der Entwicklung und dem Aufbau von Sternen. Mit der Asteroseismologie ist es möglich, die innere Struktur von Sternen zu untersuchen. In dieser Arbeit untersuchen wir die Eigenschaften der Schwingungen von Roten Riesen, die Anzeichen von Energieverlust zeigen. Wir haben den Mechanismus, der diesen Energieverlust verursacht, durch Beobachtungen eingegrenzt und festgestellt, dass er mit dem vorhergesagten Effekt des Magnetfeldes im Kern des Roten Riesen übereinstimmt. Dank neuester Entwicklungen konnten wir auch Frequenzverschiebungen aufgrund eines Magnetfelds im Kern von Sternen beobachten. Wir analysierten Sterne, bei denen sowohl magnetische Frequenzverschiebungen als auch Energieverluste in den Oszillationen auftreten, und zeigten, dass beide Phänomene durch ein Magnetfeld mit der gleichen Feldstärke im Kern der Sterne erklärt werden können.

List of abbreviations

CHeB	Core-Helium burning
MCMC	Markov-Chain Monte Carlo
PDS	Power density spectrum
RGB	Red Giant Branch
TACO	Tool for the Automated Characterisation of Oscillations
UP	Universal Pattern

List of physical constants

symbol	name	value in SI units
$M_\odot$	Solar mass	1.988410×10^{30} kg
$L_\odot$	Solar luminosity	3.828×10^{26} W
$R_\odot$	Solar radius	6.957×10^{8} m
σ	Stefan-Boltzmann constant	$5.670374419184431 4 \times 10^{-8}\,\mathrm{W\,m^{-2}\,K^{-4}}$
c	Speed of light in vacuum	$2.99792458 \times 10^{8}\,\mathrm{m\,s^{-1}}$
G	Gravitational constant	$6.6743 \times 10^{-11}\,\mathrm{m^{3}\,kg^{-1}\,s^{-2}}$

Contents

I dedicate this thesis to my grandparents who, each in their own way, inspired me to pursue my dreams.

1

Context and theoretical background

Almost a century ago, Eddington (1926) deplored the fact that mankind would never be able to unravel the mysteries of the interior of the stars from observations. What he found particularly unfortunate was that – at least, within the scope of knowledge at the time – we can never verify calculations of the internal structure (from first principles) using observations. However, Christensen-Dalsgaard and Gough (1976) realised fifty years later that geophysical methods can be applied to stars showing pulsations (i.e. small periodic variations in the observed intensity of the Sun) in order to infer the internal structure of a star from these pulsations. The field of *helioseismology* was born. Further developments of the theoretical and observational methods permitted the identification of these pulsations as resonant modes in the Sun that are repeatedly stochastically excited and damped in the convective outer regions of the Sun (see e.g. Goldreich and Keeley, 1977; Goldreich and Kumar, 1988; Balmforth, 1992). Evidently, *asteroseismology* was developed by applying the same physical principles to stars outside our solar system. The advent of space missions such as CoRoT (Baglin et al., 2006), *Kepler* (Koch et al., 2010; Borucki et al., 2010) and TESS (Ricker et al., 2014) lead to an important leap forward in the number of target stars (see e.g. Bowman et al., 2020). Space missions also greatly improved the data quality as the targets can be observed for a longer time without interruptions such as the day/night cycle (i.e. better resolution of the oscillation frequencies) and without the noise contribution of the Earth's atmosphere (see e.g. Bowman et al., 2020). A succinct introduction to the observational methods can be found in Sect. 1.2. We refer the reader to reviews such as Aerts et al. (2010); Hekker and Christensen-Dalsgaard (2017); Basu and Chaplin (2018, and references therein) for additional information.

One characteristic type of pulsating star is a solar-like oscillator. These stars exhibit oscillation modes driven by turbulent convection in their convective outer regions, similar to the Sun (see e.g. Houdek et al., 1999; Samadi and Goupil, 2001; Dupret et al., 2009). The internal structure of solar oscillators at various evolutionary stages can however greatly differ from the Sun. Red giants are a particularly interesting type of solar-like oscillator because their non-radial oscillation modes have a mixed oscillation character which results from the coupling of oscillation modes from different mode cavities (see Sect. 1.2). Due to this mixed character, the oscillation modes carry information from the inner and outer regions of the star. Since their detection (Hekker et al., 2009; De Ridder et al., 2009) specific methods have been developed that allowed to precisely determine the evolutionary stage of a red giant (see e.g. Bedding et al., 2011; Mosser et al., 2011b; Kallinger et al., 2012; Vrard et al., 2016) as well as, for example, its core-rotation rate (see e.g. Beck et al., 2011; Deheuvels et al., 2014; Gehan et al., 2018).

Over a decade ago, Mosser et al. (2012) analysed over a thousand red giants and identified a subset of 50 stars with signs of energy dissipation in certain oscillation modes. Up until today, the source of this additional damping of these specific modes remains unclear. In an attempt to explain the observed reduction of the mode amplitudes, Fuller et al. (2015) developed the *magnetic greenhouse effect*, which models the complete dissipation of the mode energy of a non-radial mode by conversion into Alfvén waves due to a strong magnetic field in the central regions of the star (i.e. in the core). We can generalise this framework by not making any assumptions on the source of the additional damping, which we subsequently called the *full dissipation framework*. Although the global features of a large sample of stars (over 600 with signs of energy dissipation) seem to be in agreement with the predictions of the full dissipation framework (see Stello et al., 2016a,b), the analysis of the individual modes in several stars (Mosser et al., 2017a; Arentoft et al., 2017) challenges the main assumption of the framework: complete mode energy dissipation. A framework considering partial dissipation has been developed recently (Loi and Papaloizou, 2017; Loi, 2020; Müller et al., 2025). These new developments however still have to be confronted to observations. Moreover, futher theoretical analysis is required to assess the validity of this new framework under more general assumptions (see e.g. Loi and Papaloizou, 2018). As the presence of a magnetic field in the core has been suggested to explain the observed dissipation of mode energy, it is important to search for other observational magnetic effects on the properties of the oscillation modes in red giants (Mathis et al., 2021; Bugnet et al., 2021; Bugnet, 2022; Li et al., 2022; Deheuvels et al., 2023; Hatt et al., 2024). If we can observe these effects and mode-energy dissipation simultaneously for a star, we can observationally link the mode-energy dissipation to the presence of a magnetic field. In this thesis, we will mainly focus on obtaining new observational constraints on the damping mechanism at play in these stars. We are also particularly interested to what extent magnetic fields play a role in this mechanism.

In the following sections, we briefly summarise the stellar evolution for the low-mass stars up to the CHeB phase (Sect. 1.1), introduce the basic concepts of red-giant asteroseismology (Sects 1.2.1 and 1.2.2) and discuss the observational effects of a magnetic field in the core on the observed oscillation modes (Sect. 1.2.3).

1.1. Low-mass star evolution

In this section, we briefly describe the evolution of low-mass stars (0.8 -2.5 $M_\odot$) up to the core-Helium burning (CHeB) phase. After its formation thorugh the collapse of giant molecular cloud, the protostar accretes mass and contracts to attain hydrostatic equilibrium before being able to start nuclear fusion in the core (Kippenhahn et al., 2013). The star is said to have reached the main sequence (Kippenhahn et al., 2013). We mainly focus on the changes in the stellar structure during the main sequence and the red-giant-branch (RGB) phase to better understand the properties of solar-like oscillation modes (Sect. 1.2.1). A more detailed description may be found in Kippenhahn et al. (2013).

1.1.1. Main sequence

The main sequence is characterised by a stable phase of nuclear hydrogen-burning (i.e. nuclear fusion reactions) in the core. For stars at the lower end of the mass range (0.8 -1.2 $M_{\odot}$), the central temperature is not high enough, so that the temperature-sensitive nuclear reaction rates of the *CNO* cycle are low compared to those of the *pp*-chain (Kippenhahn et al., 2013). The nuclear reactions of the *pp*-chain are therefore the main source of nuclear energy. These nuclear reactions gradually deplete the hydrogen content in the central regions of the star (Kippenhahn et al., 2013). The temperature gradient allows for a radiative core (i.e. energy is transported throught the core by radiation, see Kippenhahn et al., 2013), while the outer envelope is fully convective (i.e. energy is transported through large convective motions, see Kippenhahn et al., 2013). The change in composition due to nuclear fusion in the core perturbs the hydrostatic equilibrium causing the core to contract, increasing the temperature and thus the nuclear reaction rates of the *pp*-chains (Kippenhahn et al., 2013). The gradual contraction eventually leads to a more efficient energy transport and an increase in the luminosity.

For the higher-mass end of the mass range of interest for red giants (1.2-2.5 $M_{\odot}$), the central temperature is so high that the nuclear reaction rates of the *CNO*-cycle are large and the cycle can efficiently generate nuclear energy. Due to the high energy flux of this chain of nuclear reactions, only convection can efficiently transport the energy, resulting in a convective core (Hekker and Christensen-Dalsgaard, 2017). To maintain hydrostatic and thermal equilibrium of the star during the nuclear burning through the *CNO*-cycle, the outer envelope has to expand and cools down (Kippenhahn et al., 2013). Due to convection in the core, the hydrogen depletion occurs homogeneously in the entire core. When almost all core-hydrogen is depleted, the entire star contracts to counteract the decreasing energy production rate in the central regions of the star (Hekker and Christensen-Dalsgaard, 2017).

The main sequence, independent of the stellar structure of the star, ends once hydrogen is fully depleted in the core. Before the ignition of the inert helium core, the energy production of contraction and H-shell burning allows the star to maintain hydrostatic and thermal equilibrium (Kippenhahn et al., 2013).

1.1.2. Stellar evolution after the main sequence until helium-ignition in a degenerate way

After central hydrogen depletion, the core of stars with $M \lesssim 1.4\,M_{\odot}$ starts contracting as the core mass increases due to hydrogen shell burning. The central density increases during the contraction and becomes so large that the core becomes degenerate (Hekker and Christensen-Dalsgaard, 2017). Along with the core contraction, the envelope expands and cools down (Kippenhahn et al., 2013).

The stellar envelope reaches to deeper shells as a lower temperature leads to higher opacity. As the fraction of the star that is convective increases, it quickly reaches the *Hayashi line*, which is the locus in the Hertzsprung-Russell diagram of fully convective stars of a given mass M and a given chemical composition according to Kippenhahn et al. (2013). It can be shown that stars cannot be found on the right of this line if they are in hydrostatic and convective equilibrium (Kippenhahn et al., 2013). At this point in its evolution the star has a radiative degenerate helium core and a deep-reaching envelope that is largely convective. The star is said to have reached the Red Giant Branch (RGB).

As the star is situated close to its Hayashi line, its effective temperature will remain almost constant as long as the star is dominantly convective in its envelope. This means that any change in radius will immediately affect the luminosity by virtue of the Stefan-Boltzmann law (Kippenhahn et al., 2013). The core is significantly more dense than the envelope and predominantly determines the luminosity of the star (Kippenhahn et al., 2013). Due to the ongoing nuclear burning the core mass increases and consequenly so does the luminosity of the star (Hekker and Christensen-Dalsgaard, 2017). As the convective region reaches very deep into the star and material from the central regions reach the surface, called the first dredge-up event (Hekker and Christensen-Dalsgaard, 2017). After the first dredge-up event, the star continues climbing the RGB as the mass of the core increases and at a certain point the hydrogen burning region attains the discontinuity generated by the convective outer envelope. Due to the change in chemical composition the luminosity decreases briefly and starts increasing again as the composition in the convectively well-mixed envelope is homogeneous. It is not clear how the chemical discontinuity affects the onset and the extend of the variation of the luminosity (Hekker et al., 2020).

During the hydrogen shell burning, the temperature of the core continues to increase until helium ignition at the tip of the RGB (Hekker and Christensen-Dalsgaard, 2017). In the degenerate core, the pressure only depends on the core density. Nuclear energy produced by helium burning is transformed into the internal energy of the non-degenerate ions (Kippenhahn et al., 2013). This increase in temperature leads to an even more efficient helium burning. In other words, the star goes through a thermonuclear runaway (Hekker and Christensen-Dalsgaard, 2017). The core temperature gets so high that the degeneracy is lifted and the stellar core expands (Kippenhahn et al., 2013). This burst in nuclear energy is known as the *Helium flash* at the tip of the RGB.

Once the degeneracy is completely lifted, thermal equilibrium in the now convective core is restored and a combination of core helium burning together with hydrogen shell burning can start (Hekker and Christensen-Dalsgaard, 2017). The star is said to have reached the Zero Age Horizontal Branch or ZAHB, the equivalent of the Main Sequence for central helium burning.

1.1.3. Stellar evolution after the main sequence until helium-ignition in a non-degenerate way

At the end of the Main Sequence the helium core of stars with $M \gtrsim 1.4\,M_\odot$ is not degenerate. At first, the star remains in thermal equilibrium at the beginning of the hydrogen shell burning. Due to a growing core mass, the star gets out of thermal equilibrium. The outer regions of the star will therefore cool down as they are expanding as long as the temperature in the core is not high enough to ignite helium (Kippenhahn et al., 2013). The expansion of the envelope results, by virtue of the virial theorem, in a decreasing effective temperature and luminosity. Moreover, the opacity of the envelope will increase leading to the formation of a convective region at the surface growing to deeper layers (Hekker and Christensen-Dalsgaard, 2017). The formation of this convective region is related to a strong luminosity dip. The star has become a red giant with a deep convective envelope and is located close to its Hayashi line. The envelope is so extended that the luminosity is mainly determined by the mass of the core. Due to the nuclear burning, the mass of the core increases as well as the luminosity. As the convective region reaches very deep into the star the star goes through the first dredge- up event (Kippenhahn et al., 2013). After core-helium ignition, the envelope contract as the core expands. The expansion of the core results in a decrease of the temperature and density in the hydrogen-burning shell. This decrease in temperature is linked to a decrease in the production rate of the hydrogen burning and thus of the luminosity. Once helium is depleted in the core the star starts expanding again.

1.2. Asteroseismology: staring into the deep

In this section, we describe important concepts from the theory of stellar oscillations. These theoretical concepts are of great use to interpret the observed oscillations in red giants. We emphasise the effect that a core-magnetic field exerts on the oscillation modes to help us develop tests to assess the potential presence of a core-magnetic field in red giants that show signs of mode-energy loss.

1.2.1. Theoretical stellar oscillations

We briefly describe how to derive a crude approximation to the equations describing stellar oscillations in the following section (see e.g. Unno et al., 1989; Aerts et al., 2010; Basu and Chaplin, 2018). We note that the simplifications are necessary to make the system analytically solvable. In practice, the full system of equations is solved using numerical methods (see e.g. Townsend and Teitler, 2013).

The oscillations are considered to be small, linear perturbations to the equilibrium state of a star. The equilibrium solution of the stellar equations (conservation of mass, momentum and energy, together with Poisson's equation) is spherically symmetric, time-independent and typically static. We can describe a perturbation Q' to the equilibrium state $Q_0(r)$ of the quantity Q either from a fixed position in space (i.e. an *Eulerian* perturbation)

$$Q(r,t) = Q_0(r) + Q'(r,t) \tag{1.1}$$

or moving along with a perturbed mass element (i.e. a *Lagrangian* perturbation)

$$\delta Q(r,t) = Q'(r,t) + \xi(r,t) \cdot \nabla Q_0. \tag{1.2}$$

Here $\xi(r,t)$ is the Lagrangian displacement from equilibrium.

By perturbing all equilibrium quantities in the stellar structure equations and expressing the quantities in spherical polar coordinates, we obtain a set of fourth-order differential equations. This set of equations constitutes an eigenvalue problem where each eigenfunction and eigenvalue ω describe a mode of oscillation.

The eigenfunctions of this system can be separated in time and spatial variables (see e.g. Basu and Chaplin, 2018). The time-dependence is typically expressed as $\exp(i\omega t)$ with a complex eigenvalue $\omega = \omega_r + \omega_i i$. The real part of ω, ω_r, is the frequency of the oscillatory behaviour, while its complex part ω_i describes the contribution from excitation (i.e. growth) and damping (i.e. decay) processes (see e.g. Hekker and Christensen-Dalsgaard, 2017, and references therein). Here, we derive the oscillation equations in the adiabatic case and we therefore do not expect damping or excitation (i.e. energy exchange with the surroundings), resulting in a real frequency ω. The spatial part of the eigenfunctions of this system can be described with radial displacement functions together with horizontal displacement functions in the form of spherical harmonics $Y_l^m(\theta,\phi)$ of spherical degree l and azimuthal order m as a function of the co-latitude θ (measured from the pole) and longitude ϕ. The spherical degree l and azimuthal order m, together with the *radial order* n (or overtone) specify the geometry of each oscillation mode.

The radial order n can be seen as the labels for the different eigenfrequencies of the system for a given spherical degree l (Basu and Chaplin, 2018). Conventionally, we define the radial order n as the number of nodes in the radial direction. The spherical degree l indicates how many nodal lines are visible at the stellar surface and $|m|$ how many of these surface nodal lines are parallel to the equator (Aerts et al., 2010). It should be noted that since we assumed spherical symmetry, the definition of the equator is ambiguous (i.e. any great circle could be defined as the equator) and therefore the eigenfrequencies and eigenfunctions will not depend on the azimuthal order m. Rotation or magnetism, for example, can break the spherical symmetry, rendering the eigenfrequencies and eigenfunctions dependent on m.

To reduce the order of the system of differential equations, we can ignore the perturbation of the gravitational potential, the so-called *Cowling approximation* (see e.g. Basu and Chaplin, 2018). This approximation is valid for high radial order n or high spherical degree l. For high radial order (i.e. high number of nodes for the eigenfunction in the radial direction), the eigenfunctions vary more rapidly than the equilibrium quantities (Aerts et al., 2010). Assuming high radial order, the so-called asymptotic approximation, and being far enough from the stellar centre (Aerts et al., 2010; Basu and Chaplin, 2018), we can further simplify the system of equations to

$$\frac{d^2\xi_r}{dr^2} = -K(r)\xi_r \tag{1.3}$$

with

$$K(r) = \frac{\omega^2}{c_s^2}\left(\frac{N^2}{\omega^2} - 1\right)\left(\frac{S_l^2}{\omega^2} - 1\right). \tag{1.4}$$

The function $K(r)$ depends on the angular frequency ω, the adiabatic sound speed c_s and the Lamb and buoyancy frequencies S_l and N, defined respectively as

$$S_l^2 \equiv \frac{l(l+1)c_s^2}{r^2} \tag{1.5}$$

and

$$N^2 \equiv g\left(\frac{1}{\Gamma_1}\frac{\partial \ln p}{\partial r} - \frac{\partial \ln \rho}{\partial r}\right) \tag{1.6}$$

where g is the local gravitational acceleration, p is pressure and Γ_1 is the first adiabatic exponent. We note that N^2 indicates if a layer at position r is unstable against convection ($N^2 < 0$, see e.g. Hekker and Christensen-Dalsgaard, 2017).

The sign of the function $K(r)$ determines the (exponential or periodic) behaviour of the perturbation (see also Aerts et al., 2010; Basu and Chaplin, 2018). When $\omega^2 > S_l^2, N^2$ or $\omega^2 < S_l^2, N^2$, the last two factors in Eq. (1.4) have the same sign and $K(r)$ is positive. We expect an oscillatory behaviour in these regions of the star. The boundaries of these are set by the turning points (where $K(r) = 0$) of the characteristic frequencies S_l^2 and N^2 or the physical boundaries of the star (the stellar centre and surface). The standing waves forming through the reflection of the waves at these boundaries of the propagative regions are the global oscillations of the star (Unno et al., 1989). The oscillations are said to be trapped within these so-called mode cavities. Outside of the propagative regions, we expect an exponentially damped behaviour in the evanescent zone (i.e. last two factors in Eq. (1.4) have opposite signs).

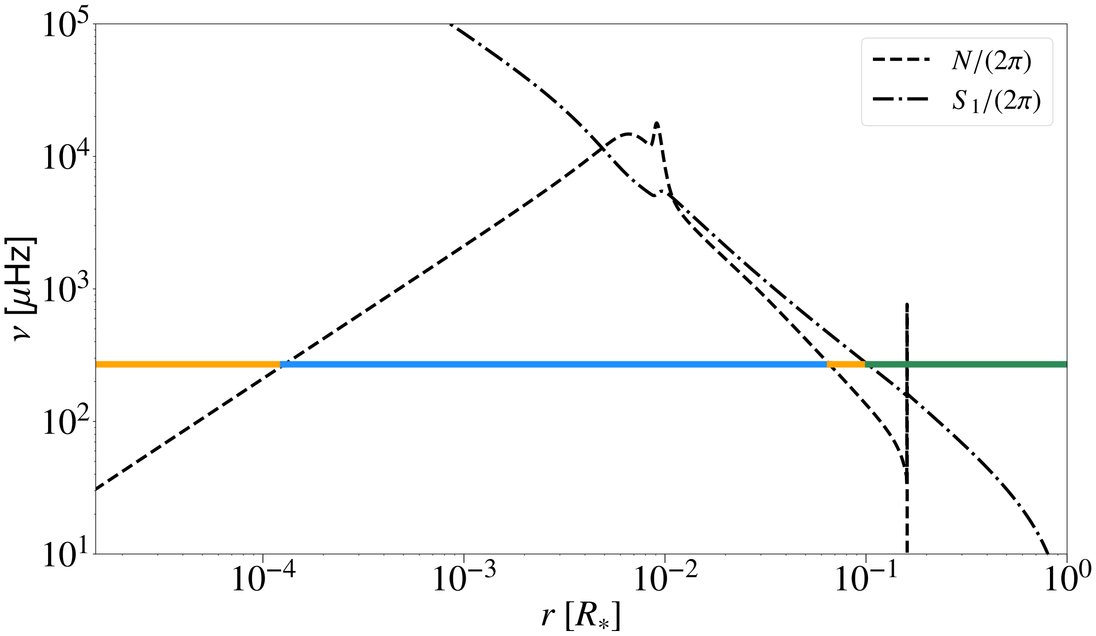

Figure 1.1: Propagation diagram for a 1.0 $M_\odot$ star at the start of the RGB phase, with the radial profiles (in units of the stellar radius R_*) of $S_1/(2\pi)$ (dash-dotted) and $N/(2\pi)$ (dashed) determining the mode cavities. At a typical oscillation frequency for this star (horizontal solid line) we mark the g-mode cavity (blue), the p-mode cavity (green) and the evanescent zones (orange) for a dipole mode.

The physical conditions in such a mode cavity determine the properties of the trapped oscillations (Aerts et al., 2010). To determine these properties, we have to solve Eq. (1.3) within the mode cavity. The general solutions can be obtained using the JWKB method (after Jeffreys, Wentzel, Kramers, and Brillouin, see Aerts et al., 2010, in particular their Appendix E). By matching the solutions at the different turning point, we can obtain the condition for standing waves in a mode cavity:

$$\int_{r_l}^{r_u} K(r)^{1/2} dr = \left(n - \frac{1}{2}\right)\pi \tag{1.7}$$

where r_l and r_u are the boundaries of the considered mode cavity. In other words, the standing waves in a mode cavity (i.e. the global oscillations) fulfil the condition set by Eq. (1.7).

In Fig. 1.1, the radial profiles of the frequencies $S_l/(2\pi)$ and $N/(2\pi)$ are shown for a 1.0 $M_\odot$ star at the start of the RGB phase. We see that the regions where $\omega^2 > S_l^2, N^2$ and $\omega^2 < S_l^2, N^2$, the so-called mode cavities, are found in the inner and outer regions of the star.

We also define the normalised mode inertia I_{nl} of a oscillation mode of radial order n and l as (Hekker and Christensen-Dalsgaard, 2017)

$$I_{nl} = \frac{\int_V \rho |\xi(r,t)|^2 dV}{M|\xi(R)|^2}, \tag{1.8}$$

where V, M and R are the total volume, mass, and radius of the star, and where $|\xi(R)|^2$ represents the average squared photospheric displacement (Hekker and Christensen-Dalsgaard, 2017). The mode inertia is useful to characterise the contributions of the different stellar regions to the oscillation mode (Hekker and Christensen-Dalsgaard, 2017).

1.2.1.1 Pressure modes (p-modes)

For high frequencies $\omega^2 > S_l^2, N^2$, we can approximate K as

$$K(r) \simeq \frac{1}{c_s^2}\left(\omega^2 - S_l^2\right). \tag{1.9}$$

This expression is strongly dependent on the sound speed and can be obtained from the dispersion relation of plane sound waves (Aerts et al., 2010). We identify these modes as standing acoustic waves with the pressure gradient as the restoring force. These modes are therefore called *pressure* modes, or p-modes.

Expanding the condition for standing waves in Eq. (1.7), we find the following expression for the frequencies (see e.g. Aerts et al., 2010):

$$\nu_{n_p l} = \frac{\omega_{n_p l}}{2\pi} \simeq \left(n_p + \frac{l}{2} + \epsilon_p\right)\Delta\nu - d_{0l}, \tag{1.10}$$

with n_p the acoustic radial order (an integer value), ϵ_p a phase shift, d_{0l} a small second-order correction and the large frequency separation $\Delta\nu$ defined as (see e.g. Hekker and Christensen-Dalsgaard, 2017)

$$\Delta\nu \equiv \left[2\int_0^R \frac{dr}{c_s}\right]^{-1}. \tag{1.11}$$

From the expression for the frequencies of p-modes (Eq.(1.10)), we deduce that p-modes of the same spherical degree l are equally spaced in frequency in successive acoustic radial orders (by the large frequency separation $\Delta\nu$).

1.2.1.2 Gravity modes (g-modes)

We also expect an oscillatory behaviour of the eigenfunctions if $\omega^2 < S_l^2, N^2$. Taking the limit $\omega^2 \ll S_l^2$, we can approximate K by

$$K(r) \simeq \frac{l(l+1)}{r^2}\left(\frac{N^2}{\omega^2} - 1\right). \tag{1.12}$$

We can relate this expression to the dispersion relation for gravity waves (at least for the radial component, see e.g. Aerts et al., 2010). The restoring force of the oscillations is thus gravity, hence the name *gravity* modes, or g-modes. A thorough asymptotic analysis (Tassoul, 1980) based on Eq. (1.7) shows that the matching condition for standing waves is

$$\nu_{n_g l} = \frac{\omega_{n_g l}}{2\pi} \simeq \frac{1}{\Delta\Pi_l\left(n_g + l/2 + \epsilon_g\right)} \tag{1.13}$$

with n_g the radial order (an integer value), ϵ_g a phase shift and the asymptotic period spacing for g-modes of spherical degree l (see e.g. Aerts et al., 2010)

$$\Delta\Pi_l \equiv \frac{2\pi^2}{\sqrt{l(l+1)}}\int_{r_1}^{r_2} \frac{N dr}{r}. \tag{1.14}$$

where r_1 and r_2 are the inner and outer turning points of the g-modes (i.e. the boundaries of the g-mode cavity). From Eq. (1.13), we see that g-modes in successive radial orders are equally spaced in period.

1.2.1.3 Mixed modes

From the propagation diagram of a RGB star shown in Fig. 1.1, it is clear that mode propagation through both cavities at a given frequency is possible. If a mode from one cavity has enough energy to travel through the evanescent zone without being completely damped, it could keep an oscillatory behaviour in the other cavity. Such modes are called mixed modes since they behave as p-modes in the outer layers of the star and as g-modes in the innermost regions of the star.

We can describe those modes in the asymptotic limit in a similar fashion as the pure p- and g-modes. It can be shown that the frequencies of the mixed modes fulfil the following matching conditions (see Shibahashi, 1979; Unno et al., 1989):

$$\cot\left(\int_{r_a}^{r_b} K(r)^{1/2} dr\right) \tan\left(\int_{r_c}^{r_d} K(r)^{1/2} dr\right) = q \tag{1.15}$$

with r_a and r_b the inner and outer limit of the g-mode cavity, r_c and r_d the inner and outer limit of the p-mode cavity, and the coupling factor (i.e. how much energy is transported between the mode cavities)

$$q_l = \frac{1}{4} \exp\left(-2 \int_{r_c}^{r_b} |K(r)^{1/2}| dr\right). \tag{1.16}$$

We note that the expression for q_l is only an approximation of the true coupling strength between the mode cavities (Basu and Chaplin, 2018).

Using a similar approach as for the derivation of the pure p- and g-mode frequencies, we can rewrite Eq. (1.15) as

$$\tan\left(\pi\left[\frac{\nu}{\Delta\nu} - \frac{l}{2} - \epsilon_p\right]\right) = q_l \tan\left(\pi\left[\frac{1}{\nu\Delta\Pi_l} - \epsilon_g\right]\right). \tag{1.17}$$

The solutions of this equation are the asymptotic mixed-mode frequencies of spherical degree l.

1.2.1.4 Mode excitation and damping of oscillations in red giants

The oscillations observed in red giants and solar-like stars are stable (see e.g. Samadi et al., 2015, and references therein). The driving mechanism operating in red giants is called stochastic driving. Turbulent motions in the outer convective regions of the star are sufficiently strong to transfer acoustic energy into the energy of the global oscillations (Aerts et al., 2010). Hence, the modes are of a stochastic nature. As the modes are mainly excited and damped by the turbulent motions, their resulting mode amplitudes will be small (Basu and Chaplin, 2018). The solar-like oscillations are also damped by radiative losses in the central regions of the star (Basu and Chaplin, 2018).

1.2.2. Observational asteroseismology

To extract the frequencies from a variable quantity, we have to transform our dataset (i.e. varying measurements as a function of time) from the time-domain into the frequency-domain by applying a Fourier transform (see e.g. Aerts et al., 2010; Basu and Chaplin, 2018, for more information). Since the oscillations are not coherent over the length of the observations, the phase of the oscillations is not maintained (Basu and Chaplin, 2018). We can therefore compute the frequency power spectrum (i.e. the squared norm of the Fourier Transform) without loss of information (Aerts et al., 2010; Basu and Chaplin, 2018). The frequency power spectrum is typically computed in units of power per unit frequency (i.e. ppm^2 Hz^{-1}), which is the frequency power spectrum divided by the frequency resolution $\delta\nu = 1/T$ with T the total timespan of the dataset (Hekker and Christensen-Dalsgaard, 2017; Basu and Chaplin, 2018). We therefore call it the power density spectrum (PDS) or simply *power spectrum*. The highest frequency of the power spectrum is the *Nyquist frequency* $\nu_{\mathrm{Nyq}} = 1/(2\delta t)$ where δt is the sampling rate of the data (Hekker and Christensen-Dalsgaard, 2017).

The varying quantity for oscillation modes is either the stellar intensity (i.e. periodic increases and decreases in the observed intensity) or the radial velocity of the star (i.e. the inward and outward motions of the stellar surface). Intensity measurements will be more affected by the convective motions at the stellar surface than the radial-velocity measurements while the radial-velocity measurements have a lower sensitivity to the stellar limb (Hekker and Christensen-Dalsgaard, 2017; Basu and Chaplin, 2018). The intensity measurements of stars (except the Sun) are integrated over the stellar disk causing a geometrical cancellation effect that renders it difficult to observe oscillation modes with a spherical degree $l > 3$ (see e.g. Aerts et al., 2010; Basu and Chaplin, 2018). This cancellation effect occurs because a higher degree l results in more nodal lines dividing the stellar surface into zones. Neighbouring zones have opposite signs, so that the contributions of these zones to the integral over the stellar disk cancel each other out (see e.g. Aerts et al., 2010).

If observational gaps and aliases (e.g. from the motions of the instrumentation or observation conditions such as day/night cycles) are present in the observed dataset, the observed profiles of the oscillations are affected. It can be shown that the gaps will generate sidebands in the observed profiles in the power spectrum of the star. The number of gaps and their length compared to the total timespan T determines how strong these sidebands in the power spectrum are compared to the intrinsic profile of the oscillation mode.

1.2.2.1 Power spectrum of a typical red giant

Other periodical variations contribute to the power spectrum of a red giant in addition to stellar oscillations. The main additional constributions are attributed to the granulation from the convective motions on the surface, magnetic surface activity, and rotation.

The effect of granulation in the power spectrum has been empirically modelled (Kallinger et al., 2014) as a sum of three so-called *granulation components*:

$$P_{\mathrm{bgr}}(\nu) = \sum_{j=1}^{3} \frac{H_j}{1 + \left(\frac{\nu}{b_j}\right)^4}, \tag{1.18}$$

with H_j and b_j are the height and characteristic frequency (related to the characteristic timescale of motion of the granules) of the jth granulation component. This is equivalent to modelling the granulation process at the stellar surface as a combination of damping processes (see e.g. Basu and Chaplin, 2018).

The effect of surface magnetic activity (i.e. stellar spots) will be observed at lower frequency and is typically incorporated within the granulation component with the lowest characteristic frequency (Basu and Chaplin, 2018).

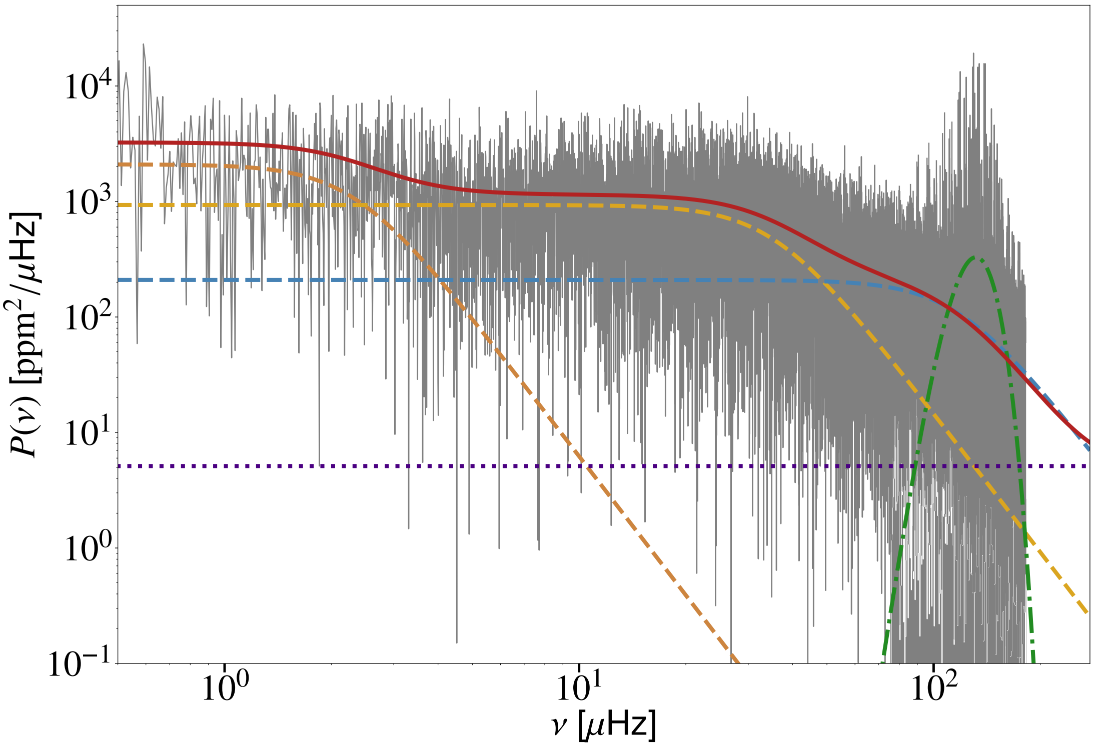

Figure 1.2: Power spectrum $P(\nu)$ of the red giant KIC 9145955 as a function of cyclic frequency ν. The granulation components are respresented by the three dashed curves (orange, yellow and blue). we also show the photon noise contribution (purple dotted line) and the bell-shaped power envelope (green dashed-dotted curve). The total background model for the power spectrum is shown by the red solid curve.

In addition to all the physical processes that are related to stellar activity at the surface, we also have to consider the contribution of the photon noise in the instrumentation (Hekker and Christensen-Dalsgaard, 2017). As the length of the timeseries from spatial missions are typically of the order of years, the photon count is so high that the Poisson's distribution of the photon noise is approximately gaussian (Basu and Chaplin, 2018). A normally distributed noise contribution to the signal has a constant contribution P_n to the power spectrum (Basu and Chaplin, 2018).

Lastly, the combined contribution of all solar-like oscillations to the power spectrum has a bell shape that is centred around the frequency of maximum oscillation power ν_max (Hekker and Christensen-Dalsgaard, 2017). We describe this power excess in the power spectrum as a Gaussian function of the form

$$P_\mathrm{osc}(\nu) = P_\mathrm{g} \exp\left[-\frac{(\nu - \nu_\mathrm{max})^2}{2{\sigma_\mathrm{env}}^2}\right], \tag{1.19}$$

with P_g and σ_env the height and width of the power excess.

Our total background model for the power spectrum is (see also Fig. 1.2)

$$P_\mathrm{B}\,(\nu) = P_\mathrm{n} + \eta_a^2(\nu) P_\mathrm{bgr}(\nu). \tag{1.20}$$

we note that the contribution of the oscillations is not part of the background model. We however have to consider this contribution to correctly model the background contribution in the power spectrum.

The factor $\eta_a^2(\nu)$, called the *apodization*, is needed to account for the fact that the integration time of the instrument (the time needed to integrate the signal in the detector) is not infinitely small. It can be shown that this attenuation factor can be written as

$$\eta_a^2(\nu) = \mathrm{sinc}^2\,(\pi\nu\delta t) = \mathrm{sinc}^2\left(\frac{\pi\nu}{2\nu_\mathrm{Nyq}}\right) \tag{1.21}$$

with $\mathrm{sinc}(\nu) = \sin(\nu)/\nu$ and $\mathrm{sinc}(0) = 1$ (Hekker and Christensen-Dalsgaard, 2017).

1.2.2.2 Signal of oscillation mode in power spectrum

The different contributions being identified, we now focus on the information that we can extract from the signal of individual oscillation modes in the power spectrum. An oscillation mode in a star can be described as the solution to the equation for a damped and driven harmonic oscillator (e.g. Samadi et al., 2015):

$$\frac{d^2\xi_r}{dr^2} + 2\eta_p \frac{d\xi_r}{dr} + \omega_p^2 \xi_r = f(t) \tag{1.22}$$

with η_p the damping rate of the mode, $\omega_p = 2\pi\nu_p$ the angular eigenfrequency of the mode and $f(t)$ the forcing term. The Fourier Transform of an infinitely long timeseries of such a mode would have the form (see Eq. (5.56) from Aerts et al., 2010)

$$P(\nu) = \frac{1}{16\pi^2\nu_p^2\eta_p^2} \frac{P_f(\nu)}{1 + \frac{8\pi^2(\nu-\nu_p)^2}{2\eta_p}}. \tag{1.23}$$

where $P_f(\nu)$ is the average power spectrum of the forcing term $f(t)$ and $\nu = \omega/2\pi$. This Lorentzian profile only occurs for time series with an infinitely large timespan. The frequency resolution $\delta\nu$ of the power spectrum of an observed time series determines how well the shape of the Lorentzian profile can be resolved. If $\eta/\delta\nu \gg 1$, the mode peak in the frequency spectrum resembles a Lorentzian profile as the frequency resolution is small enough to resolve the entire profile in the frequency spectrum (Aerts et al., 2010). In other words, the timespan of the observations is long enough to extend over a large number of independent realisations of the mode (Basu and Chaplin, 2018). We therefore model individual resolved mode oscillations in the power spectrum of a red giant using the Lorentzian function (see e.g. Hekker and Christensen-Dalsgaard, 2017):

$$P(\nu) = \frac{H_p}{1 + \left(\frac{2(\nu-\nu_p)}{\Gamma_p}\right)^2}\,. \tag{1.24}$$

Here H_p, ν_p and Γ_p are the height, central frequency and linewidth of the Lorentzian profile. We note that we can directly relate the mode linewidth measured in the power spectrum to the mode damping rate η_p, namely

$$\Gamma_p = \frac{\eta_p}{\pi}. \tag{1.25}$$

The mode amplitude of a resolved mode in the power spectrum $A_{p,\mathrm{res}}$ is defined as the square root of the area under the Lorentzian profile:

$$A^2_{p,\mathrm{res}} = \frac{\pi\Gamma_p H_p}{2}. \tag{1.26}$$

If, $\eta/\delta\nu \ll 1$, the Lorentzian profile will be unresolved and therefore the observed profile of the mode resembles a sinc^2-function:

$$P\,(\nu) = H_p\ \mathrm{sinc}^2\left(\pi\frac{\nu-\nu_p}{\delta\nu}\right). \tag{1.27}$$

Similarly as for a resolved mode, the mode amplitude $A_{p,\mathrm{unres}}$ of an unresolved mode is defined as the square root of the area under the profile:

$$A^2_{p,\mathrm{unres}} = H_p\delta\nu. \tag{1.28}$$

1.2.2.3 Interpretation of the oscillation power spectrum

After dividing the power spectrum by the background contribution in Eq. (1.20) and limiting the frequency range to the range where the contribution of the solar-like oscillations dominates the power spectrum, we obtain a normalised power spectrum, as shown in Fig. 1.3.

To interpret the observed power spectrum, let us recall that the asymptotic frequencies of pure pressure radial ($l = 0$), dipole ($l = 1$), and quadrupole ($l = 2$) modes in red giants are (i.e. Eq. (1.10), see also Tassoul, 1980):

$$\begin{aligned}
\nu_{n_p0} &= \left(n_p + \epsilon_p\right)\Delta\nu \\
\nu_{n_p1} &= \left(n_p + 1/2 + \epsilon_p\right)\Delta\nu - d_{01} \\
\nu_{n_p2} &= \left(n_p + 1 + \epsilon_p\right)\Delta\nu - d_{02}
\end{aligned} \tag{1.29}$$

We thus expect that the radial and quadrupole pressure modes are located close to each other in frequency, because $\nu_{n_p+1\,0} - \nu_{n_p2} \simeq d_{02}$ (second-order term in the asymptotic expression). In other words, we expect to detect a repeating pattern of radial and quadrupole pairs of modes.

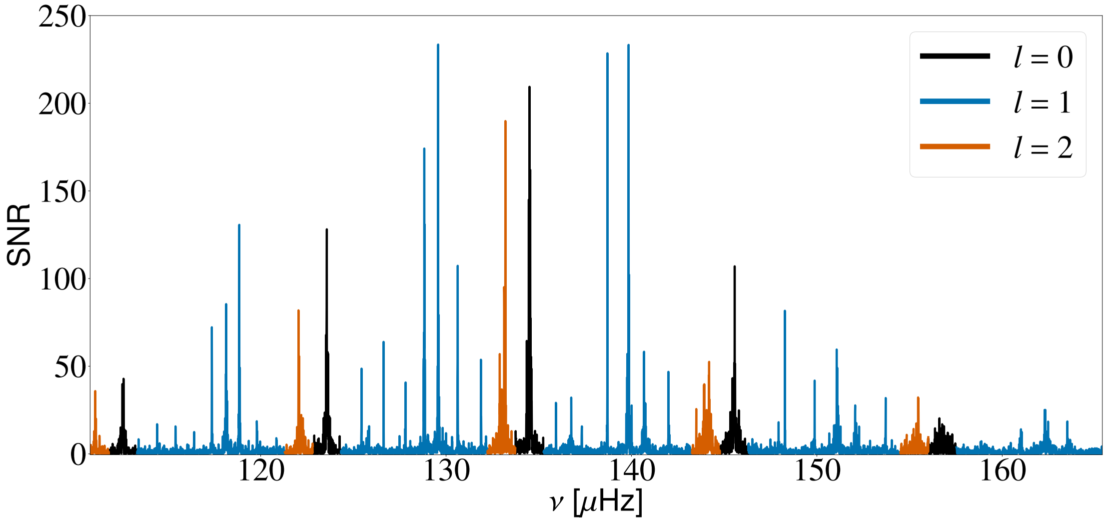

Figure 1.3: Power spectrum of the red giant KIC 9145955 normalised by the background model, shown for the frequency range in which oscillations are observed. We specifically show the frequency ranges derived from the universal pattern (see text for more details) where we expect radial ($l = 0$), dipole ($l = 1$), and quadrupole ($l = 2$) modes in respectively black, blue and orange. we note that octupolar ($l = 3$) modes are most likely also present within the dipole-mode frequency ranges.

Since successive pure pressure modes of the same spherical degree are almost always separated in frequency by the large frequency separation $\Delta\nu$, it is convenient to construct the échelle diagram (Grec et al., 1983) of the power spectrum. This diagram consists of stacked segments of the frequency range of length $\Delta\nu$. In Fig. 1.4, we show such a diagram for the power spectrum in Fig. 1.3 and we observe that the radial modes do not align vertically in the échelle diagram as predicted by the asymptotic frequencies in Eq. (1.29). Based on the observations of hundreds of stars, Mosser et al. (2011b) confirmed that the deviation from the linear alignment in the échelle diagram is due to a second-order term in the radial order in the asymptotic expressions in Eq. (1.29). The authors derived the so-called *universal pattern* to describe the frequencies of pure pressure modes of spherical order l in the power spectrum of any red giant as a function of $\nu_{\max}$ and $\Delta\nu$:

$$\nu_{n_p l} = \left[n_p + \frac{l}{2} + \epsilon_p + \frac{\alpha}{2}\left(n_p - \frac{\nu_{\max}}{\Delta\nu}\right)^2 \right] \Delta\nu - d_{0l}, \tag{1.30}$$

where α is the curvature of the frequency pattern of pure pressure modes. A recent study suggests that there is a connection between the curvature of the large frequency separation and the structure in the outer regions of the star (see Hekker et al., in prep.). We show the expected location of the pure pressure modes in the échelle diagram in Fig 1.4. Two main ridges describe the radial and quadrupole modes. The dipole-mode spectrum is much richer than predicted by the universal pattern. For this particular star, we observe dipole mixed modes suggesting that the coupling between the mode cavities for the dipole modes is strong enough to allow dipole modes to propagate through both mode cavities. To simplify the description of the universal pattern and the identified modes, we omitted to show the octupolar modes in Figs 1.3 and 1.4.

Let us now focus on the pure g-modes to further interpret the remaining observed modes in the power spectrum in Fig. 1.3. The asympotic expression for the frequency of a g-mode

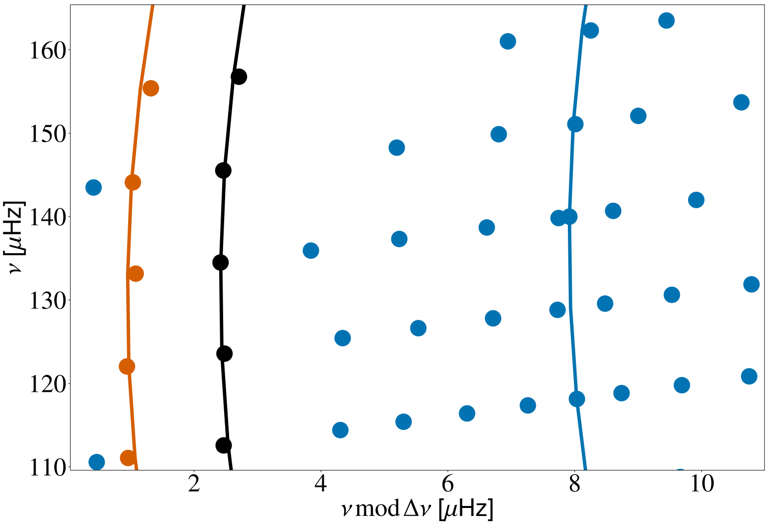

Figure 1.4: Frequency échelle diagram for the star KIC 9145955 with a large frequency separation $\Delta\nu$ of 11 μHz. We show the identified radial ($l = 0$), dipole ($l = 1$), and quadrupole ($l = 2$) modes as respectively black, blue and orange dots. The theoretical ridges derived from the universal pattern are shown as full curves.

$\nu_{n_g l}$ of spherical degree l is

$$\frac{1}{\nu_{n_g l}} = \left[n_g + \frac{1}{2} + \epsilon_g \right] \Delta\Pi_l, \tag{1.31}$$

with $\Delta\Pi_l$ the asymptotic period spacing.

In a similar way as what was done for the frequencies of the pure p-modes, we can construct a period échelle diagram (P = $1/\nu$) of the dipole modes to help us interpret the detected oscillation frequencies. We see in Fig. 1.5 that the observed dipole modes do not align vertically as expected for pure g-modes. The deviation from the central alignment is strongest at the frequencies of the pure pressure modes (indicated with blue dashed lines in Fig. 1.5). This is a clear indication that these modes are mixed, since these modes have most likely a strong contribution from the p-mode cavity (i.e. behaving mainly as a p-mode). Furthermore, we observe a recurring pattern in each radial order (i.e. between successive acoustic radial modes, indicated with black dashed lines in in Fig. 1.5). The analytical expression for the mixed modes Eq. (1.17) describes this observed pattern.

Based on the deviation of the observed period from the asymptotic period spacing of pure g-modes, Mosser et al. (2015) derived an expresssion for the observed period spacing ΔP between successive mixed modes together with its relation to the asymptotic g-mode period spacing $\Delta\Pi_1$ through the ζ-function:

$$\Delta \mathrm{P} = \zeta(\nu)\Delta\Pi_1. \tag{1.32}$$

The ζ-function is defined as

$$\zeta(\nu) = \left[1 + \frac{\nu^2 \, q \, \Delta\Pi}{q^2 \Delta\nu + \left(1 - q^2\right)^2 \Delta\nu \sin^2 \theta_p} \right]^{-1}, \tag{1.33}$$

where θ_p is taken to be

$$\theta_p \equiv \frac{\pi \left(\nu - \nu^p_{n_p 1} \right)}{\Delta\nu}, \tag{1.34}$$

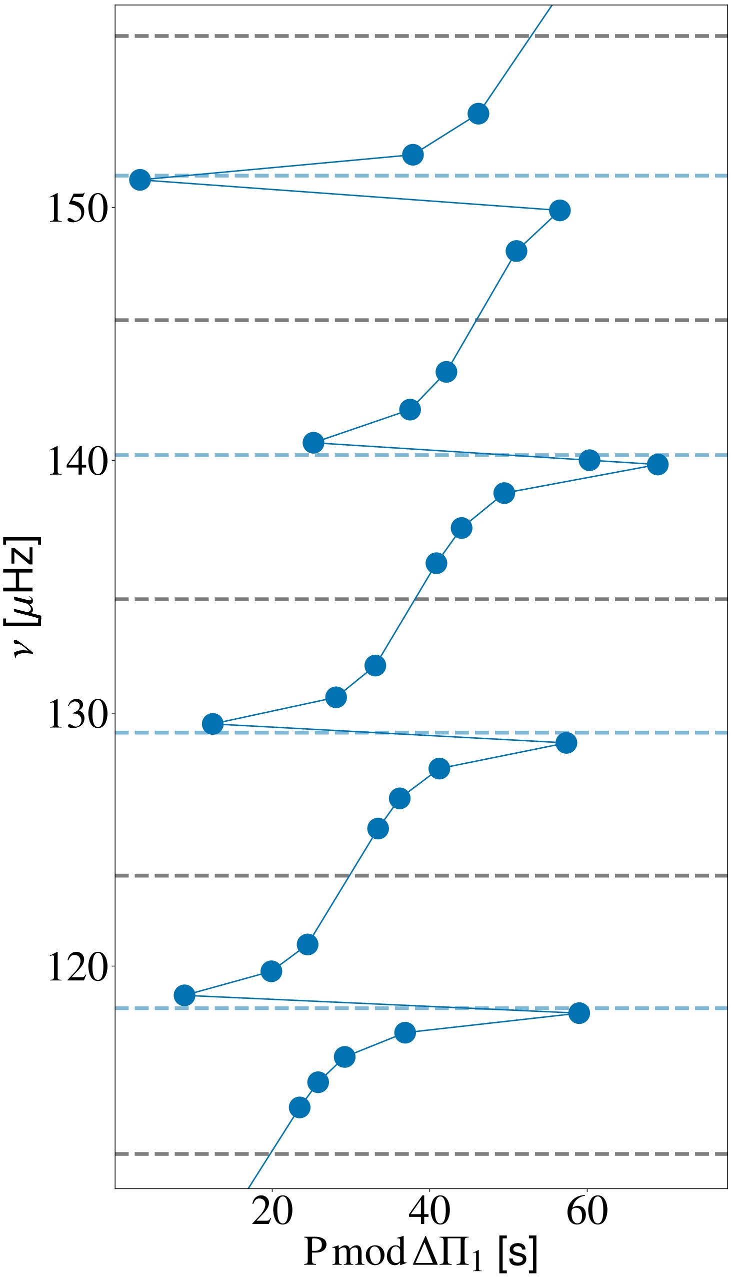

Figure 1.5: Period échelle diagram for the star KIC 9145955 with an asymptotic period spacing $\Delta\Pi_1$ of 76.9 s. We show the observed dipole modes (blue dots) as well as the frequencies of the pure pressure dipole modes (blue dashed lines). Different acoustic radial orders are indicated by the frequencies of the radial modes (black dashed lines).

with $\nu^p_{n_p 1}$ the frequency of the pure pressure dipole mode in radial order n_p.

From Goupil et al. (2013) and later Deheuvels et al. (2014, 2015) we can relate the function $\zeta(\nu)$ to the inertia of the mixed modes and in particular to the ratio of the mode inertia in the g-mode cavity (I_g) to the total mode inertia ($I_g + I_p$, i.e. over the g- and p- mode cavities respectively):

$$\zeta(\nu) \simeq \frac{I_g}{I_g + I_p}. \tag{1.35}$$

This means that this function can be used to quantify the contribution from the mode cavities to the mode properties. If $\zeta \simeq 1$ for a mode, this mode has a predominant g-mode character (i.e. $I_g \gg I_p$). From Eq. (1.32), we deduce that g-dominated modes have a period spacing close to the asymptotic period spacing of g-modes. If however $\zeta \simeq 0$ the mode has a predominant p-mode character (i.e. $I_g \ll I_p$). According to Eq. (1.32), these modes aslo have the largest deviation from the asymptotic period spacing as seen in Fig. 1.5. Dipole modes with a predominant p-mode character are almost equally spaced in frequency by the large frequency separation $\Delta\nu$.

1.2.3. Effect of a magnetic field on mixed oscillation modes

In this thesis, we aim to assess if a magnetic field in the core can explain the observed mode-energy loss in non-radial modes of red giants. We therefore focus in this section on the observational effects that a magnetic field can have on the mixed modes of red giants.

We typically distinguish two regimes for magnetic fields when evaluating their effect on oscillations. Firstly, weak magnetic fields are described as a perturbation to the restoring forces of the oscillations, similar to what is done for so-called slow rotation (see e.g. Bugnet et al., 2021; Mathis et al., 2021; Li et al., 2022). Recent developments indicate that these weak magnetic fields shift the frequencies of all non-radial modes; even zonal modes ($m = 0$) (Mathis et al., 2021). In contrast to rotationally induced frequency shifts, the magnetic frequency shift is always positive and only depends on the absolute value of the azimuthal order m. The properties of the magnetic shift imply that weak magnetic fields inherently lead to asymmetric multiplets (modes with same radial order n and spherical degree l but different m) of non-radial mixed modes (Bugnet et al., 2021; Mathis et al., 2021; Li et al., 2022) that can be observed (see e.g. Li et al., 2022, 2023; Hatt et al., 2024). In general, we expect to observe the combined effect of rotation and magnetism (see Fig. 7 of Bugnet et al., 2021, for a representative sketch of the effect of magnetic and rotation frequency shifts on the mixed-mode frequency of non-radial modes). Disentangling the contribution from both effects remains a complex problem (see e.g. Bugnet et al., 2021; Li et al., 2022; Hatt et al., 2024).

Secondly, strong magnetic fields are able to efficiently dissipate mode energy in the central regions of a star (see e.g. Fuller et al., 2015; Loi and Papaloizou, 2017; Loi, 2020; Rui and Fuller, 2023; Müller et al., 2025). The threshold field strength at which the mode energy entering the g-mode cavity is fully dissipated is called the critical field strength B_{crit}. Due to this full dissipation of the g-mode character, we expect to only detect pure pressure-modes. To investigate the mode properties when the g-mode character is fully dissipated (independently of the source of the additional damping) the full dissipation framework was developed (see Chapter 3).

1.2.3.1 Weak magnetic field in the core: magnetic shift

Mathis et al. (2021) derived the asymptotic magnetic shift for pure pressure and pure gravity modes. Similar as for rotation (Goupil et al., 2013), the magnetic shift of mixed modes is a combination of the pure p- and g-mode magnetic shifts. The contribution of the shift in in each mode cavity is set by the mode character, which is represented by the function $\zeta(\nu)$. Because the field is strongest in the core, Bugnet (2022) showed that the magnetic shift is dominated by the contribution from the g-mode cavity. Following the theoretical developments by Mathis et al. (2021) and Bugnet (2022), we can write the observed frequency ν_{obs} of a mixed dipole mode affected by the magnetic shift as

$$\nu_{\mathrm{obs}} = \nu + \left(\frac{|m|+1}{2}\right)\zeta(\nu)\delta\nu_{\mathrm{mag,g}}(\nu) \tag{1.36}$$

with ν the asymptotic unperturbed mixed dipole-mode frequency, m the azimuthal order of the dipole mode, and $\delta\nu_{\mathrm{mag,g}}(\nu)$ the frequency-dependent shift on the pure g-mode frequencies due to the magnetic field in the core.

Li et al. (2022) as well as Mathis et al. (2021); Bugnet et al. (2021) independently derived that the frequency-dependence of $\delta\nu_{\mathrm{mag,g}}$ can be written as

$$\delta\nu_{\mathrm{mag,g}}(\nu) = \left(\frac{\nu_{\mathrm{max}}}{\nu}\right)^3 \delta\nu_{\mathrm{mag,g}}\left(\nu = \nu_{\mathrm{max}}\right) = \left(\frac{\nu_{\mathrm{max}}}{\nu}\right)^3 \delta\nu_{\mathrm{mag}} \tag{1.37}$$

where $\delta\nu_{\mathrm{mag}}$ is the intrinsic magnetic shift measured at ν_{max}.

Using Eq. (1.37) to rewrite the observed frequency in Eq. (1.36), we find

$$\nu_{\mathrm{obs}} = \nu + \left(\frac{|m|+1}{2}\right)\left(\frac{\nu_{\mathrm{max}}}{\nu}\right)^3 \zeta(\nu)\delta\nu_{\mathrm{mag}} \tag{1.38}$$

It is not always straightforward to determine $|m|$ observationally and we therefore define the effective magnetic shift $\delta\nu_{\mathrm{mag,eff}}$ as

$$\delta\nu_{\mathrm{mag,eff}} \equiv \left(|m|+1\right)\delta\nu_{\mathrm{mag}}. \tag{1.39}$$

We can now describe observed frequencies as a function of the unperturbed asymptotic mixed-mode frequencies, the ζ-function, and the effective magnetic shift:

$$\nu_{\mathrm{obs}} = \nu + \frac{\zeta(\nu)\delta\nu_{\mathrm{mag,eff}}}{2}\left(\frac{\nu_{\mathrm{max}}}{\nu}\right)^3. \tag{1.40}$$

The expression in Eq. (1.40) can be fitted to the observed dipole-mode frequencies to obtain the effective magnetic shift $\delta\nu_{\mathrm{mag,eff}}$.

1.2.3.2 Strong magnetic field in the core: the full dissipation framework

To determine the effects of a strong magnetic field in the core on the mode properties, we can use the predictions in the general full dissipation framework. We briefly summarise the main predictions in the following paragraphs and refer the reader to Chapter 3 for more detailed information about the framework. We note that a magnetic field is considered strong for a mode of spherical degree l if the magnetic field strength is larger than the critical magnetic field at the radial coordinate r_H (the radial coordinate of the hydrogen-burning shell, as (Fuller et al., 2015; Rui and Fuller, 2023):

$$B_{\rm crit} = 2\pi^2 \sqrt{\mu_0 \rho} \frac{\nu_{\rm max}^2}{\sqrt{l(l+1)}N} r_H, \tag{1.41}$$

where ρ is the mass density, r_H the radial coordinate of the H-burning shell and μ_0 the magnetic permeability in vacuum.

To quantify the effect of the full dissipation of the g-mode character we require a proxy for the energy in an oscillation mode. We define for this purpose the normalised visibility v_{nl} of a non-radial oscillation mode of spherical degree l in the acoustic radial order n as

$$v_{nl} \equiv \frac{A_{nl}^2}{A_{n0}^2 \mathcal{G}_l}, \tag{1.42}$$

with A_{nl} the amplitude of the mode, A_{n0} the amplitude of the radial mode of the same acoustic radial order and $\mathcal{G}_l$ a geometrical factor depending on spherical degree, limb-darkening effects and the bolometric correction (see e.g. Ballot et al., 2011). In this study, we use the mean observed visibility of stars with typical dipole modes as the geometrical factor $\mathcal{G}_l$ in Eq. (1.42) ($\mathcal{G}_1 \approx 1.35$ and $\mathcal{G}_2 \approx 0.688$, see e.g. Mosser et al., 2012; Stello et al., 2016b). These values are roughly similar to the values that Ballot et al. (2011) obtained for pure p-modes considering the spectral response function of the *Kepler* instrumentation.

Since the g-mode character is fully dissipated, we only observe one mode of spherical degree l per acoustic radial order (i.e. no mixed character). In other words, all the observed oscillation modes will be pure pressure modes. Within this framework, we can also relate the normalised visibility to the ratio of the radial-mode linewidth to the non-radial-mode linewidth:

$$v_{nl} = \frac{\Gamma_{n0}}{\Gamma_{nl}}. \tag{1.43}$$

Lastly, we can express the normalised visibility in this framework as a function of the radial-mode linewidth, the coupling factor q_l (i.e. how strongly the mode cavities couple which acts as a proxy for the fraction of energy transmitted to the g-mode cavity) and the large frequency separation $\Delta\nu$ (Takata, 2016; Mosser et al., 2017a):

$$v_l \simeq \left[1 - \ln\left(\frac{1-q_l}{1+q_l}\right)\frac{\Delta\nu}{\pi\Gamma_0}\right]^{-1}. \tag{1.44}$$

In the limit of a thick evanescent zone (i.e. $q_l \ll 1$, see e.g. Unno et al., 1989, for more information), the expression in Eq. (1.44) can be approximated as

$$v_l \simeq \left(1 + \frac{2q_l\Delta\nu}{\pi\Gamma_0}\right)^{-1} = (1 + 4q_l\Delta\nu\tau)^{-1}, \tag{1.45}$$

with the radial-mode lifetime $\tau = (2\pi\Gamma_0)^{-1}$ (see Fuller et al., 2015; Mosser et al., 2017a, and references therein).

1.3. Aim and overview of the thesis

Over ten years ago, red giants with very low dipole-mode visibility, the so-called *suppressed dipole-mode stars*, were mentioned for the first time. Various mechanisms, such as rapid rotation (García et al., 2014) or non-linear coupling (Weinberg and Arras, 2019; Weinberg et al., 2021) have been proposed to explain the observed mode-energy dissipation. Even if some of these mechanisms can explain the dissipation, they are typically not able to reproduce the observed individual mode properties (frequencies, linewidths or amplitudes) of the non-radial modes. An example of such a mechanism is the *magnetic greenhouse effect* proposed by Fuller et al. (2015) and further developed by Cantiello et al. (2016) and Rui and Fuller (2023). With this mechanism, the energy entering the g-mode cavity is fully dissipated (by a magnetic field in the core). This result can in fact be used as the main assumption for a theoretical framework, the full dissipation framework. In this framework the nature of the full dissipation is not specified allowing for global predictions. These predictions for the normalised visibility seem to agree with the observations of Stello et al. (2016a,b). When Mosser et al. (2017a) analysed the power spectra of individual stars, the authors found that the majority of the stars still exhibit mixed non-radial modes. Since the g-mode character should be fully dissipated, Mosser et al. (2017a) concluded that we cannot interpret the observed mode properties within the full dissipation framework. As the observations suggest only partial dissipation of the g-mode character, we can further generalise the framework to allow for partial dissipation (see e.g. Loi and Papaloizou, 2017; Loi, 2020; Müller et al., 2025). The so-called *partial dissipation framework* can be interpreted as an intermediate regime in between full dissipation and no dissipation of the g-mode character (see e.g. Mosser et al., 2017a, for more information about these edge cases). If this interpretation is correct, it implies that a fraction of the stars with lower visibility can still be described within the so-called full dissipation framework (i.e. a fraction of the stars exhibits signs of very efficient damping leading to strong partial dissipation). Identifying this small number of stars within the suppressed dipole-mode stars would help to constrain the applicability of the full and partial dissipation frameworks. The main aim of this thesis is to obtain observational constraints on the mechanism causing the mode suppression in the non-radial modes of suppressed dipole-mode stars. A subsequent aim is to confirm or disprove that the observed mode suppression is the result of a magnetic field in the core of the star using the new observational constraints.

Before testing if the full dissipation framework can be used the describe a number of suppressed dipole-mode stars, it is important to observationally confirm that the mode-energy is indeed dissipated in the central regions of the star (i.e. the main assumption of the full and partial dissipation frameworks). To this end, we compared the radial-mode properties of suppressed dipole-mode stars to the properties of stars with typical dipole-mode visibility (see Chapter 2).

To verify the validity of the full dissipation framework and its applicability, we can assess three main predictions of this framework (see Chapter 3). Firstly, we only observe pure pressure modes, as the g-mode character is fully dissipated. Furthermore, pure pressure modes that are damped compared to the no-dissipation case should have a visibility that is directly equal to the ratio of the radial-mode linwidth to the linwidth of the non-radial mode in the same acoustic radial order (see e.g. Benomar et al., 2014; Mosser et al., 2017a, and references therein). Lastly, within the full dissipation framework, the normalised visibility can be expressed as a function of radial-mode properties and the coupling factor (see Eqs (1.44) and (1.45) Takata, 2016). By comparing the predicted visibility from this expression to the observed visibility, we can assess if the full dissipation framework can explain the observed visibility of suppressed dipole-mode stars.

Lastly, it would be valuable to connect the detection of mode-energy dissipation to the presence of a magnetic field in the core of a star. If we furthermore can estimate the field strength of the magnetic field and compare it to the critical magnetic field, we even could confirm that the observed mode suppression is consistent with the observed strength of the magnetic field in the core of the star. (see e.g. Li et al., 2022, 2023; Deheuvels et al., 2023; Hatt et al., 2024) already confirmed the presence of magnetic fields based on observed magnetic shifts in the dipole modes (Mathis et al., 2021; Bugnet et al., 2021; Bugnet, 2022; Li et al., 2022). The stars analysed by Deheuvels et al. (2023) are of particular interest as they do not show any contribution from rotation and thus allow for a more precise estimation of the magnetic field strength. These stars are thus the perfect testing ground to assess if mode suppression can indeed be observationally linked to a magnetic field in the core of a star. From the dipole modes, we can indeed confirm the presence of the magnetic field and estimate its strength. From the properties of the quadrupole modes, we can infer if these quadrupole modes experience full or partial dissipation of their g-mode character. We therefore computed our own field strength estimates from the magnetic shifts obtained from a fit to the dipole modes following the approach developed by Mathis et al. (2021); Bugnet et al. (2021); Bugnet (2022) (see Chapter 4) and furthermore compared our quadrupole-mode visibility to the predictions in the full dissipation framework (see Chapter 4).

2

The radial modes of stars with suppressed dipole modes

Authors Quentin Coppée, Jonas Müller, Michaël Bazot and Saskia Hekker

Chapter info This chapter is a reproduction of the first paper I published as part of my doctoral studies Coppée et al. (2024), A&A, 690 A324. We showed that the mode suppression in the suppressed dipole-mode stars is due to addtional damping in the central regions of the star by analysing and comparing the radial-mode properties of stars with suppressed and typical dipole modes. I was the main author of this paper and I computed, analysed and interpreted the results. The original idea of this project came from my supervisor, Saskia Hekker. Together with Michaël Bazot and Jonas Müller, they helped me with the interpretation of the results and provided useful comments and suggestions for the text and figures.

Abstract The *Kepler* space mission provided high-quality light curves for more than 16 000 red giants. The global stellar oscillations extracted from these light curves carry information about the interior of the stars. Several hundred red giants were found to have low amplitudes in their dipole modes (i.e. they are suppressed dipole-mode stars). A number of hypotheses (involving e.g. a magnetic field, binarity, or resonant mode coupling) have been proposed to explain the suppression of the modes, yet none has been confirmed. In this study, we aim to gain insight into the mechanism at play in suppressed dipole-mode stars by investigating the mode properties (linewidths, heights, and amplitudes) of the radial oscillation modes of red giants with suppressed dipole modes. We selected from the literature suppressed dipole-mode stars and compared the radial-mode properties of these stars to the radial-mode properties of stars in two control samples of stars with typical (i.e. non-suppressed) dipole modes. We find that the radial-mode properties of the suppressed dipole-mode stars are consistent with the ones in our control samples, and hence not affected by the suppression mechanism. From this we conclude that (1) the balance between the excitation and damping in radial modes is unaffected by the suppression, and by extrapolation the excitation of the non-radial modes is not affected either; and (2) the damping of the radial modes induced by the suppression mechanism is significantly less than the damping from turbulent convective motion, suggesting that the additional damping originates from

the more central non-convective regions of the star, to which the radial modes are least sensitive.

2.1. Introduction

The space missions CoRoT (Michel et al., 2006) and *Kepler* (Borucki et al., 2010) transformed asteroseismology into a field of observation-driven research by providing high-quality light curves for more than 100 000 stellar objects, including more than 16 000 red giants (Yu et al., 2018). This transformation is reflected in the major developments of red-giant asteroseismology over the last ten years (see e.g. Chaplin and Miglio, 2013; Hekker and Christensen-Dalsgaard, 2017; García and Ballot, 2019, for reviews). In red giants we observe stochastically excited oscillations undergoing inherently convective damping in the outer regions and diffusive damping in the core (e.g. Houdek et al., 1999; Samadi and Goupil, 2001; Dupret et al., 2009). Advancements in the field are mostly due to the detection of non-radial modes in the spectrum of these stars (Hekker et al., 2006; De Ridder et al., 2009). These modes have a mixed character (Beck et al., 2011; Bedding et al., 2011; Mosser et al., 2011a): they behave as gravity modes in the core region (the g-mode cavity) and as pressure modes in the outer layers of the star (the p-mode cavity). These mixed modes therefore carry information from both the p- and g-mode cavities (e.g. Beck et al., 2011; Bedding et al., 2011), while the radial modes that are pure p-modes only carry information from their p-mode cavity, which makes up nearly the entire star (see e.g. Ong and Basu, 2019).

Over a decade ago, Mosser et al. (2012) identified a set of red giants with dipole modes with unexpectedly low amplitudes. They showed that, except for the dipole-mode amplitudes, the stars have similar global properties as the other red giants in their sample. An observational analysis of a larger sample of stars with longer light curves was performed by Stello et al. (2016b). They selected red-giant-branch (RGB) stars and computed for each star the dipole-mode visibility (i.e. the ratio of the total power in the dipole modes to the total power in the radial modes). This measurement revealed that the suppression of the dipole modes relative to the radial modes decreases as stars ascend the RGB (i.e. there is less suppression for stars with a weaker coupling between the p- and g-mode cavity; see Stello et al., 2016b). The same methodology applied to quadrupole and octupole modes showed that the suppression is less pronounced for higher spherical degrees (Stello et al., 2016b).

So far, the power in the radial modes of suppressed dipole-mode stars has not been studied. In this work we investigated whether the energy of the radial modes in suppressed dipole-mode stars is different than the energy of the radial modes in stars with dipole modes with typical visibility. We aim to gain insight into the balance between the excitation and damping of these modes as well as into the potential region where the suppression mechanism dominates (i.e. either in the outer regions or in the core) by investigating the total mode power (as per the amplitude and the height) and the mode lifetime (as per the linewidth) of the radial modes.

One mechanism proposed to explain the suppression of the dipole modes is the presence of an internal magnetic field that dominates the regions of the star below a critical depth (Fuller et al., 2015). This depth can be linked to a critical frequency, below which the inward travelling gravity waves are refracted as magnetic waves over a broad range of spherical degrees. This means that the core magnetic field suppresses all contributions from the central regions to the observed non-radial oscillation modes (the ‘magnetic greenhouse effect’). The radial modes remain unaffected. The prediction for the dipole-mode visibilities of red giants made by Fuller et al. (2015) is in agreement with the observed visibilities of Mosser et al. (2012) and Stello et al. (2016b).

Using the individual frequencies of suppressed dipole-mode stars, Mosser et al. (2017a) show that some of these stars still have a significant number of mixed dipole modes, albeit with lower amplitudes. This means that the central regions still contribute to the observed non-radial modes. Loi and Papaloizou (2017) propose a mechanism that induces additional damping of the non-radial modes in the presence of a core magnetic field. They show that the contribution of the central regions of the star to the non-radial modes can be partially suppressed through resonances with torsional Alfvén waves. These results suggest that the dipole modes can experience additional damping caused by a core magnetic field and still retain their mixed character. In the case of a strong core magnetic field, Rui and Fuller (2023) show that the contribution of gravity modes should be completely suppressed in red giants. They note that a more general approach (e.g. considering higher-order WKB terms or a non-harmonic time dependence) could potentially allow dipole modes to conserve a mixed character in the presence of a strong core magnetic field.

It is also worth noting that such strong core magnetic fields have been observed in red giants using magnetic frequency splittings (see e.g. Deheuvels et al., 2023). For one of the analysed stars, the reported field is stronger than the critical field derived by Fuller et al. (2015), suggesting that gravity waves should not be able to propagate in the central regions of that particular star. Upon analysis of its power spectrum, Deheuvels et al. (2023) found mixed-mode suppression only at low frequencies. This result is an indication that strong core magnetic fields may be linked to mixed-mode suppression.

Another mechanism that can explain the suppression of dipole modes is the non-linear mode coupling between mixed modes as proposed by Weinberg and Arras (2019). The non-radial-mode visibilities computed with this mechanism (Weinberg et al., 2021) quantitatively match the visibilities of the more evolved red giants reported by Stello et al. (2016b). For this mechanism as well as for the core magnetic field, the radial modes are predicted to be unaffected.

Alternatively, mode suppression could potentially be explained by the presence of a stellar companion as its tidally induced effect can excite non-radial oscillation modes (see e.g. Ivanov et al., 2013), indirectly impacting the properties of the stochastically excited oscillation modes. Statistical results also suggest that the fraction of stars with suppressed dipole modes is larger in binary stars compared to stars that are not known to be part of a binary (see e.g. Themeßl et al., 2017). Due to the non-radial nature of tidal effects, the radial modes are not affected by the tidally induced oscillations (see e.g. Beck et al., 2019, and references therein).

Finally, strong surface magnetic fields inhibit convection in the upper stellar layers, resulting in less stochastic excitation and thus smaller amplitudes for radial and non-radial modes (e.g. Chaplin et al., 2011). Hence, this will have an impact on both the non-radial and radial modes, which is confirmed by Gaulme et al. (2014) and Schonhut-Stasik et al. (2020), who found red giants in eclipsing binaries with no or reduced observable oscillations (i.e. the tidal effect causes enhanced magnetic activity). The presence of a surface magnetic field is the only mechanism that would impact the radial as well as the non-radial modes.

We note here that a high core-rotation rate has also been proposed to explain the suppression of the dipole modes (see e.g. García et al., 2014). García et al. (2014), however, dismissed this mechanism as the cause of the suppression of the dipole modes for KIC 8561221. It is therefore most likely not the main reason for the suppression in the population of suppressed dipole-mode stars, and we do not consider it further here.

In Sect. 2.2 we specify how we selected RGB stars for our low dipole-mode visibility sample and our control samples, and in Sect. 2.3 we describe the method we applied to obtain the radial-mode properties of the selected stars. We define the metrics we used to investigate the radial-mode properties in Sect. 2.4 and present the results of our comparisons thereof in Sect. 2.5. We dedicate Sect. 2.6 to the discussion of our results and the conclusions.

2.2. Sample selection

In this section we describe the selection of stars for our low-visibility sample and how we constructed the control samples. We selected two control samples based on different approaches to compare the distributions of the radial-mode properties of the suppressed dipole-mode stars to those of stars with typical, non-suppressed dipole modes.

For all the stars considered in this work, we used long-cadence *kepseismic* light curves[1]. We only selected stars for which we have time series data with a time span longer than 1230 days and a filling factor larger than 0.77. These constraints ensure a high frequency resolution and avoid aliasing effects due to a window effect. We also cross-matched our set of stars with the APOGEE Data Release 17 (DR17) catalogue (Blanton et al., 2017; Abdurro'uf et al., 2022) to obtain stellar effective temperature $T_{\rm eff}$ and metallicity [Fe/H].

We adopted the evolutionary stage (ES) provided by Kallinger (2019) to distinguish between RGB and core-He-burning (CHeB) stars in our sample. If Kallinger (2019) did not provide an ES determination, we determined the ES with the same methodology (Kallinger et al., 2012; Kallinger, 2019). This method relies on the frequencies of the three radial modes closest to the frequency of maximal oscillation power, $\nu_{\rm max}$, and can therefore be applied to all stars in our samples consistently, irrespective of their dipole-mode visibility.

2.2.1. Low-visibility sample

In the literature we find two main sources of stars with suppressed dipole modes, Mosser et al. (2012) and Stello et al. (2016a,b). With the available data of Stello et al. (2016a) and Mosser et al. (2017a), we selected the candidates for our sample of suppressed dipole-mode stars. As shown by Stello et al. (2016a,b), the distribution in visibility of dipolar modes in their sample of stars is mostly bimodal: one subset of stars centred around 1.5 (typical visibility, Ballot et al., 2011) and another at lower visibility (see Fig. 2.1). We divided the sample of Stello et al. (2016b) into two regimes using the frequency of maximal oscillation power, $\nu_{\rm max}$, since the bimodality is less pronounced for the most evolved stars ($< 70\,\mu$Hz),

- low, $50\,\mu\text{Hz} \leq \nu_{\rm max} < 70\,\mu\text{Hz}$,

- high, $\nu_{\rm max} \geq 70\,\mu\text{Hz}$.

In each $\nu_{\rm max}$ regime, we fitted a bimodal Gaussian distribution to the dipole-mode visibility distribution and used the intersection of the two Gaussian components as the threshold visibility (see Figs. 2.1 and 2.2) and consider the stars with a dipole-mode visibility lower than

---

[1] `http://dx.doi.org/10.17909/t9-mrpw-gc07`

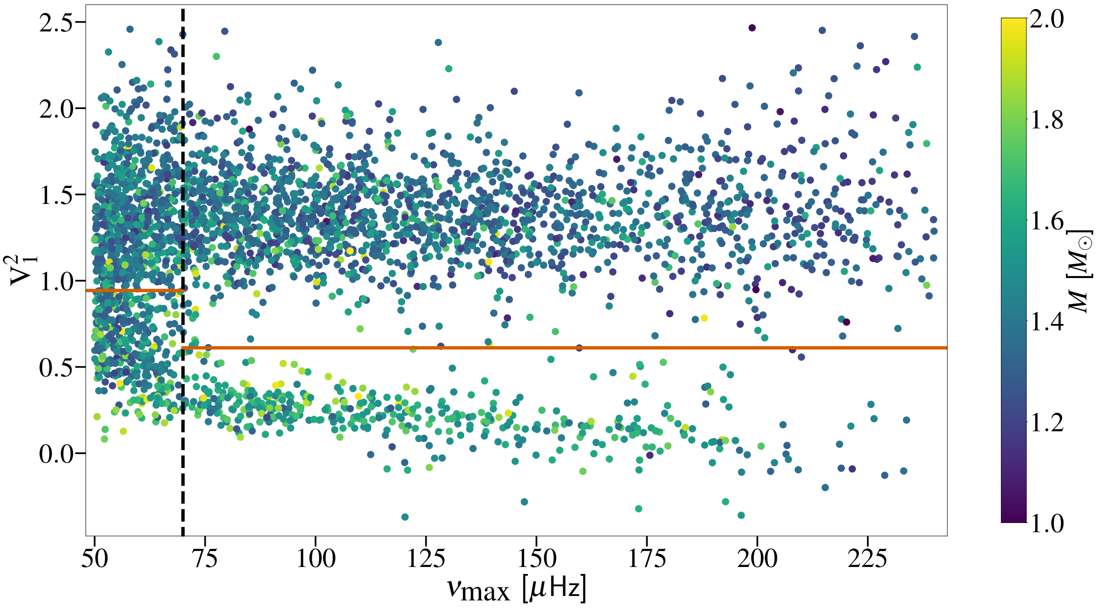

Figure 2.1: Dipole-visibility distribution as a function of $\nu_{\rm max}$ colour-coded by mass (all data from Stello et al., 2016b). The vertical dashed line indicates the boundary between the two $\nu_{\rm max}$ regimes, for which the computed visibility thresholds are indicated with horizontal orange lines (see the main text for more details). Note that the negative visibilities are attributed to measurement scatter caused by the uncertainty in the estimation of the background model (see Stello et al., 2016b, for further details).

these thresholds as candidates for our low-visibility sample. In this way, we selected in total 759 stars with low dipole-mode visibility from the sample of Stello et al. (2016a,b). We further included about 40 red giants analysed by Mosser et al. (2017a) that are not present in the sample of Stello et al. (2016a,b).

After cross-matching with the stars in the APOGEE DR17 our sample consists of 494 red giants, 451 RGB and 43 CHeB stars, with low dipole-mode visibility and spectroscopic parameters from APOGEE DR17. Since the number of RGB stars is an order of magnitude larger than the number of CHeB stars, we focus on the RGB stars for the remainder of this paper.

2.2.2. Control samples S_p and S_c

For our control samples, we pre-selected RGB stars from the APOKASC2 catalogue (Pinsonneault et al., 2019) with a typical dipole-mode visibility (around 1.5; see e.g. Ballot et al., 2011). From this, we constructed a control sample, S_p, of stars with observed stellar properties similar to those of suppressed dipole-mode stars. To this end, we selected stars by assigning to each star in our low-visibility sample a star with a typical dipole-mode visibility, similar $T_{\rm eff}$, [Fe/H], and $\nu_{\rm max}$, and large frequency separation, $\Delta\nu$ (see Sect. 2.3 for details on how we obtained the last two parameters). To identify the most suitable configuration for our control sample S_p, we used the Kuhn-Munkres algorithm (Kuhn, 1955, 1956; Munkres, 1957)[2]. This algorithm pairs up elements from two distinct sets and finds the configuration of pairs where the sum of the distances d between elements in a pair is the smallest. We

---

[2] *Python package munkres*, `https://github.com/bmc/munkres`, © Brian M. Clapper

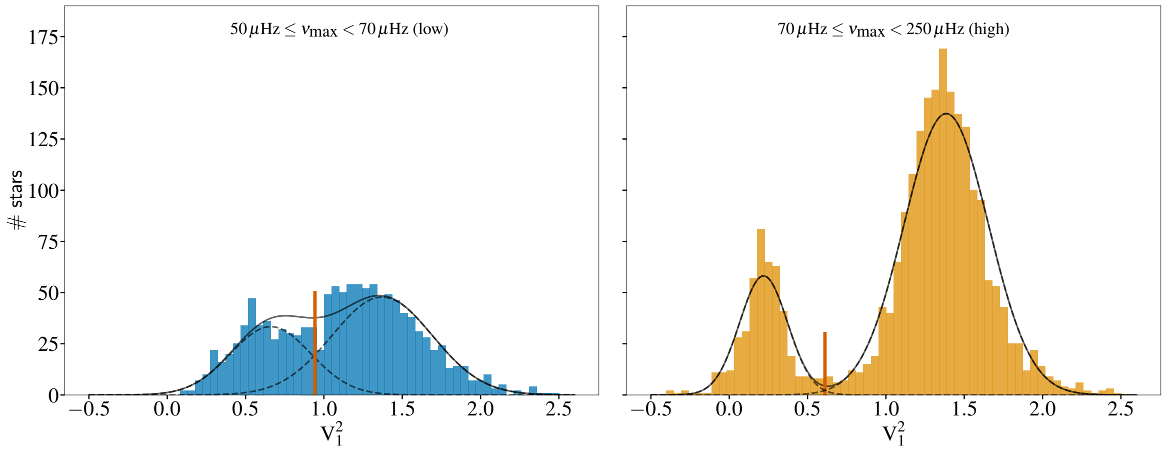

Figure 2.2: Dipole-mode visibility distribution in the different $\nu_{\max}$ regimes for the RGB and CHeB stars analysed by Stello et al. (2016b). The thresholds for the visibility are highlighted with a vertical red line. In the low $\nu_{\max}$ regime, we selected a higher visibility threshold than that obtained from the intersection of the Gaussian components. The dipole-mode visibilities are taken from Stello et al. (2016b).

defined the distance between two stars in a pair as

$$\begin{aligned} d^2 =& \frac{(T_{\mathrm{eff,T}} - T_{\mathrm{eff,\,L}})^2}{\sigma^2_{T_{\mathrm{eff}}}} + \frac{(\nu_{\mathrm{max,T}} - \nu_{\mathrm{max,\,L}})^2}{\sigma^2_{\nu_{\max}}} \\ &+ \frac{(\Delta\nu_{\mathrm{T}} - \Delta\nu_{\mathrm{L}})^2}{\sigma^2_{\Delta\nu}} + \frac{([\mathrm{Fe/H}]_{\mathrm{T}} - [\mathrm{Fe/H}]_{\mathrm{L}})^2}{\sigma^2_{[\mathrm{Fe/H}]}}, \end{aligned} \tag{2.1}$$

where the subscript T (L) denotes parameters of the star with typical (low) visibility. For the uncertainties, σ_i, we adopted the following definitions:

$$\sigma_{T_{\mathrm{eff}}} = \sqrt{\sigma^2_{T_{\mathrm{eff,\,T}},\mathrm{intr}} + \sigma^2_{T_{\mathrm{eff,\,L}},\mathrm{intr}} + 2\sigma^2_{T_{\mathrm{eff}},\mathrm{emp}}}, \tag{2.2}$$

$$\sigma_{[\mathrm{Fe/H}]} = \sqrt{\sigma^2_{[\mathrm{Fe/H}]_{\mathrm{T}},\mathrm{intr}} + \sigma^2_{[\mathrm{Fe/H}]_{\mathrm{L}},\mathrm{intr}} + 2\sigma^2_{[\mathrm{Fe/H}],\mathrm{emp}}}, \tag{2.3}$$

$$\sigma_{\nu_{\max}} = \sqrt{\sigma^2_{\nu_{\max},\mathrm{T}} + \sigma^2_{\nu_{\max},\mathrm{L}}}, \tag{2.4}$$

$$\sigma_{\Delta\nu} = \sqrt{\sigma^2_{\Delta\nu,\mathrm{T}} + \sigma^2_{\Delta\nu,\mathrm{L}}}. \tag{2.5}$$

We combined in quadrature the intrinsic uncertainties (subscript intr) of the spectroscopic parameters from APOGEE DR17 and the empirical uncertainties determined to mitigate the discrepancy between asteroseismic and spectroscopic ES classifications ($\sigma_{T_{\mathrm{eff}},\mathrm{emp}} = 44$ K, $\sigma_{[\mathrm{Fe/H}],\mathrm{emp}} = 0.04$ dex; see Elsworth et al., 2019). For the asteroseismic parameters, we combined in quadrature the uncertainties from our code TACO ($\sigma_{\nu_{\max},\mathrm{L}}$, and $\sigma_{\Delta\nu,\mathrm{L}}$; see Sect. 2.3 for more information) and the APOKASC2 catalogue ($\sigma_{\nu_{\max},\mathrm{T}}$, and $\sigma_{\Delta\nu,\mathrm{T}}$; see Pinsonneault et al., 2019).

Having similar spectroscopic and asteroseismic properties does not mean that the masses of the stars in our samples are similar as well. To assure that a different mass distribution does not affect our conclusions, we also generated a second control sample, S_c, by randomly selecting 450 RGB stars with typical dipole-mode visibilities following the cumulative density function (CDF) of the stellar mass distribution observed in the low dipole-mode visibility sample. We estimated the masses M from the asteroseismic scaling relation (see e.g.

Ulrich, 1986; Brown et al., 1991; Kjeldsen and Bedding, 1995) with reference values from Themeßl et al. (2018).

2.3. Frequency analysis

We performed the frequency analysis of the light curves of the stars in our samples with our peakbagging code TACO (Tools for the Automated Characterisation of Oscillations, Hekker et al., in prep.). In this section we provide an overview of the different steps we took to obtain the radial-mode properties.

First we describe the power density distribution (PDS) with a global model comprising the contribution of the oscillations and of the background (see Kallinger et al., 2014, for more details). We performed the remaining steps in the analysis on the background normalised PDS.

We applied the peak detection method developed by García Saravia Ortiz de Montellano et al. (2018) to detect the peaks in the normalised PDS. We fitted a Lorentzian function,

$$P_{\rm peak}\left(\nu\right) = \frac{H_{\rm peak}}{1 + \left(\frac{\nu - \nu_{\rm peak}}{\gamma_{\rm peak}}\right)^2}, \tag{2.6}$$

to each individual detected peak with $\nu_{\rm peak}$, $H_{\rm peak}$, and $\gamma_{\rm peak}$ the central frequency, height, and half width at half maximum (HWHM) of the peak. We used a maximum likelihood estimation optimisation and computed lower limits of the uncertainties for each peak using a Hessian matrix. Finally, to identify the radial and quadrupole modes, we cross-correlated the observed normalised PDS with a synthetic normalised PDS based on the universal pattern (Mosser et al., 2011b).

We compared the values of $\nu_{\rm max}$ and $\Delta\nu$ obtained with our code to the results obtained using ABBA (Kallinger, 2019) and the FREQ method (Vrard et al., 2018). The comparison shows that our results are in agreement with the results of ABBA and the FREQ method. For $\nu_{\rm max}$ the agreement is within one $\Delta\nu$ and for $\Delta\nu$ within 3σ. Graphical representations of, and additional information about this comparison can be found in Appendix A.1.

2.4. Radial-mode properties

The width, height and amplitude of the Lorentzian function (Eq. 2.6) describing an oscillation mode carry information about the excitation and damping processes affecting this mode (see e.g. Hekker and Christensen-Dalsgaard, 2017, and references therein).

The HWHM $\gamma_{\rm peak}$ or linewidth $\Gamma_{\rm peak}$ (full width at half maximum) of a mode are directly related to the mode-damping rate, η, and the mode lifetime, τ,

$$\gamma_{\rm peak} = \frac{\Gamma_{\rm peak}}{2} = \frac{\eta}{2\pi} = \frac{1}{2\pi\tau}, \tag{2.7}$$

while $A^2_{\rm peak}$ (the square of the mode amplitude, i.e. the area under the Lorentzian) and $H_{\rm peak}$ (the height of the Lorentzian; see Eq. 2.6) are related to the total energy of the mode and are defined as

$$A^2_{\rm peak} = \pi\gamma_{\rm peak}H_{\rm peak}. \tag{2.8}$$

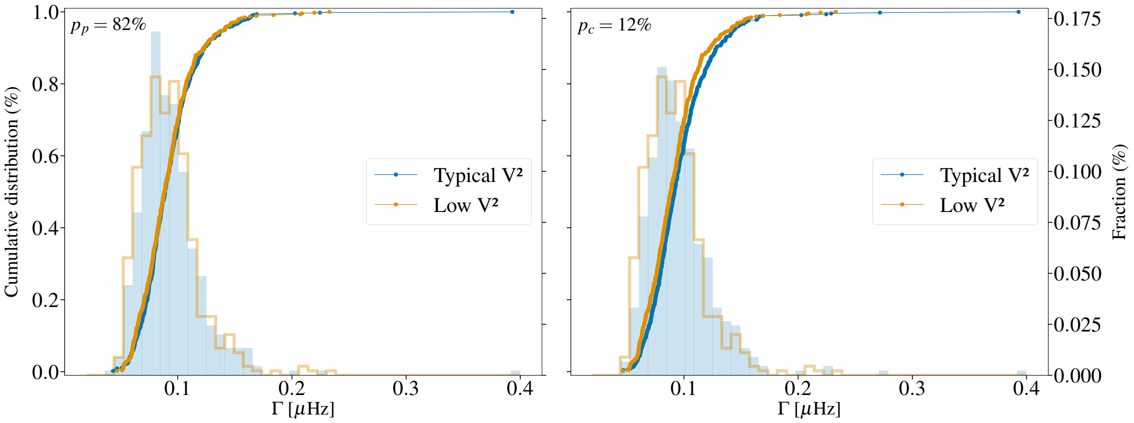

Figure 2.3: Cumulative distributions of the global linewidth, Γ, for the S_p (left) and S_c (right) control samples (blue) compared to the low-visibility sample (orange). The distributions are shown as histograms in the background (see the right vertical axis for the fraction of stars per bin). The respective p-values of the KS test are shown in the top-left corner of the panels.

To condense the information of the different radial modes per star into a single value for the linewidth, amplitude, and height, we defined a global radial linewidth (Γ), amplitude (A), and height (H) as the classical weighted average properties of the three radial modes closest to $\nu_{\rm max}$, namely the modes for which we typically obtain the most precise mode parameters:

$$\Gamma \equiv \frac{w_1\Gamma_1 + w_2\Gamma_2 + w_3\Gamma_3}{w_1 + w_2 + w_3} \tag{2.9}$$

$$A \equiv \frac{W_1A_1 + W_2A_2 + W_3A_3}{W_1 + W_2 + W_3} \tag{2.10}$$

$$H \equiv \frac{\mathcal{W}_1H_1 + \mathcal{W}_2H_2 + \mathcal{W}_3H_3}{\mathcal{W}_1 + \mathcal{W}_2 + \mathcal{W}_3}, \tag{2.11}$$

with the weights $w_i = \sigma_{\Gamma_i}^{-2}$, $W_i = \sigma_{A}^{-2}$, and $\mathcal{W}_i = \sigma_{H_i}^{-2}$ defined as a function of the uncertainties σ_{Γ_i}, σ_{A_i}, and σ_{H_i} of the ith radial mode. To take the spectral response of the *Kepler* instrumentation into account, we applied the bolometric correction from Ballot et al. (2011) to the global radial amplitude. In other words, we computed the bolometric amplitude $A_{\rm Bol}$ for each star:

$$A_{\rm Bol} = A \cdot \left(\frac{T_{\rm eff}}{5934\ {\rm K}}\right)^{0.8}. \tag{2.12}$$

We compared our resulting amplitudes and linewidths with values available in the literature. We find that the individual and global radial-mode properties for the stars in our samples are similar to the ones computed in the same way based on the linewidths and amplitudes reported by Kallinger (2019, ABBA). We find agreement with the results based on the data from Kallinger (2019) within 10%, which is within the typical uncertainties. Furthermore, our bolometric amplitudes are consistent with the results obtained by Vrard et al. (2018). However, our global radial-mode linewidths are about 40% smaller than the ones reported by Vrard et al. (2018, i.e. the FREQ method). By comparing the linewidths obtained by Vrard et al. (2018) and Kallinger (2019), we also observe that the linewidths in Vrard et al. (2018) are systematically broader. Although we find that our linewidths are overall narrower for the stars we have in common, the distributions in the global radial-mode parameters are still consistent independent of the datasets that were chosen (the dataset resulting from our code or the datasets from Vrard et al. 2018 or Kallinger 2019). Comparisons of the differences between the datasets can be found in Appendix A.2.

2.5. Results

In this section we present the comparison of the CDFs of global radial-mode properties (Γ, H, and A_{Bol}) from each control sample to the ones from the low dipole-mode visibility sample (see Figs. 2.3, 2.4, and 2.5). For a quantitative comparison, we used the p-values of the Kolmogorov-Smirnov two-sample test (the KS test hereafter; Hodges, 1958), that is, the probability that the two samples are taken from the same underlying distribution (the null hypothesis). A p-value smaller than 1 % indicates that we can reject the null hypothesis.

We find that we cannot reject the hypothesis that the distributions in Γ for stars in S_p and S_c are similar to the distribution for suppressed dipole-mode stars (see Fig. 2.3, where the p-values of the KS test are 82 and 12 %, respectively). Since Γ can be related to the average mode-damping rate η, and consequently to the average mode lifetime, τ (see Eq. 2.7), we conclude that the convective damping of the radial modes is not altered by the suppression mechanism in suppressed dipole-modes stars.

We additionally find that we cannot reject the hypothesis that the distribution in the bolometric amplitude A_{Bol} and H observed in S_p and S_c are similar to the distribution observed for suppressed dipole-mode stars (see Fig. 2.4, where the p-values of KS test are 27 and 4 %, respectively, and Fig. 2.5, where the p-values are 24 and 53 %). This indicates that the total power in the radial modes (scaling as A_{Bol}^2 and as H) is comparable for stars with low and typical dipole-mode visibility.

We checked that the conclusions we draw from the KS test are not influenced by the randomness implemented in our selection procedures. We therefore generated 5000 realisations of S_p and S_c by randomly selecting a value in the uniformly distributed interval $[x - \sigma_x, x + \sigma_x]$ for parameter x (T_{eff}, [Fe/H], ν_{max}, $\Delta\nu$, M, Γ, H, and A_{Bol}) with uncertainty σ_x. If we cannot reject the null hypothesis of the KS test for a large majority of these realisations compared to the distribution observed in the low-visibility sample for a given parameter, we conclude that this parameter has a similar distribution for both control and low-visibility sample. For all our parameters we can conclude that the low-visibility and control samples are drawn from the same underlying distribution.

Additionally, we repeated the selection procedure to generate four additional control samples S_c to investigate the influence of the random selection of stars for our control sample. It is important to mention that the same star can be selected for different samples. Again, we find no significant difference in the distributions of the radial-mode properties of low- and typical-visibility stars for any of these samples.

Finally, we checked if our results are independent of the chosen metric in Eqs. 2.9, 2.10, and 2.11. We repeated our comparison with the properties of the three central radial modes, and with the arithmetic mean instead of a weighted mean. For all metrics, we obtain the same results: the distributions of the radial-mode properties for our low-visibility stars are consistent with the properties of the stars in our control samples.

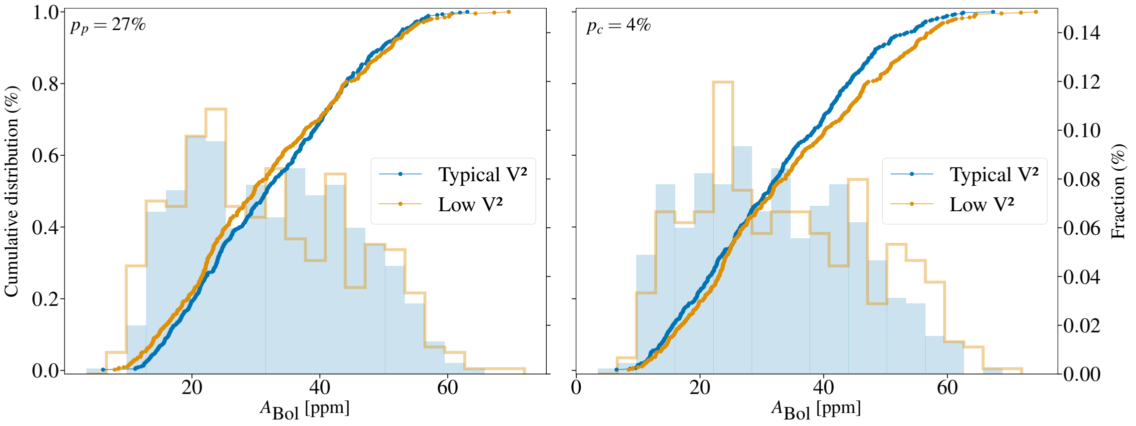

Figure 2.4: Same as Fig. 2.3, but now for bolometric amplitude, A_{Bol}.

2.6. Discussion and conclusions

In this study we measured and compared the radial-mode properties of stars with suppressed and non-suppressed dipole modes. We find that the linewidths, and by extension the radial-mode damping rates of the radial modes (see Eq. 2.7), are similarly distributed for both types of stars.

We also show that the bolometric amplitudes and the heights of the radial modes are distributed similarly for suppressed and non-suppressed dipole-mode stars. Moreover, since the radial-mode height is independent of the mode inertia, our results show that the mode energy (related to the height and the squared bolometric amplitude) is similarly distributed for both types of stars.

As the mode energy represents the balance between damping and excitation processes (see e.g. Hekker and Christensen-Dalsgaard, 2017), we infer from our results that the excitation of the radial modes is unaffected by the mechanism causing the suppressed-dipole modes. Assuming that modes of different spherical degrees are excited in a similar manner, this means that all modes are excited similarly in stars with suppressed and non-suppressed dipole modes. This then leads us to conclude that the observed suppression is caused by additional damping and not by lack of excitation.

The additional source of damping does not significantly affect the radial modes (i.e. the convective damping in radial modes seems unaffected). Under the assumption that the convective damping of the dipole modes is similar to the convective damping of the radial modes (see e.g. Mosser et al., 2017a), the additional damping is likely taking place in the stellar core, to which mixed modes are more sensitive than the radial modes.

Since we find that the excitation of the radial modes remains unaffected by the suppression mechanism, our results suggest that a mechanism impacting the mode excitation, such as the presence of a strong surface magnetic field, is likely not the cause of the suppression of the dipole modes in low-visibility stars. For the core magnetic field mechanism, Fuller et al. (2015) note that the magnitude of the core magnetic field is assumed to be too low to affect the radial modes. Different theoretical approaches, such as those developed by Lecoanet et al. (2017) or Loi and Papaloizou (2017), confirm that the presence of a core magnetic field can reduce the dipole-mode amplitudes without affecting the radial modes. Additionally, Cantiello et al. (2016) extended the theoretical analysis of Fuller et al. (2015)

by investigating the generation, evolution, and detectability of core magnetic fields and corroborated the results from Fuller et al. (2015). Based on a more general analysis, Rui and Fuller (2023) conclude that above a given magnetic field strength, inward travelling gravity waves will indeed be refracted at a critical depth and will be converted to outgoing slow magnetic waves that dissipate before reaching the stellar surface, leaving the radial-mode properties unaffected.

The resonant mode coupling is a three-wave interaction between mixed modes where a non-radial mode destabilises two other modes with an initially low amplitude (Weinberg and Arras, 2019). According to Weinberg et al. (2021), the relatively small displacements near the stellar centre and the large damping rate dominated by convective damping prevent the radial modes from being impacted by this interaction. For red giants in binaries, Beck et al. (2019) conclude that the tidal effects do not significantly impact the radial modes, as no change in the large frequency separation and no radial-mode amplitude modulation were observed. Based on the binary fraction (about 10 %) in our low dipole-mode visibility sample, it appears nevertheless unlikely that binarity alone can cause the suppression.

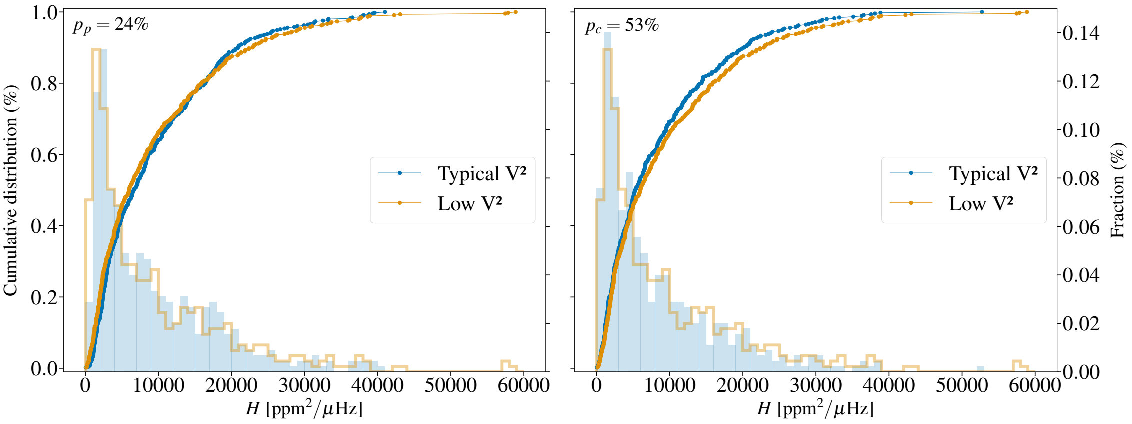

Figure 2.5: Same as Fig. 2.3, but now for height, H.

In summary, our findings support either a strong core magnetic field or resonant mode coupling as the suppression mechanism, while surface-magnetic fields seem rather unlikely. According to the binary fraction in the suppressed dipole-mode sample, tidal effects are likely not the cause of the mode suppression. Further investigations into core magnetic fields will be presented in a forthcoming work by Müller et al. (in prep.).

Acknowledgments Original paper acknowledgements.

We thank the referee for their useful comments and remarks that considerably improved the manuscript. We acknowledge funding from the ERC Consolidator Grant DipolarSound (grant agreement # 101000296).

3

Full and partial dissipation of g-mode character in the non-radial modes of suppressed dipole-mode stars

Authors Quentin Coppée, Jonas Müller, Jeong Yun Choi and Saskia Hekker

Chapter info This chapter is based on the second paper I submitted as part of my doctoral studies. With this study, we showed that a combination of the full and partial dissipation frameworks are needed to explain the mode properties of the suppressed dipole-mode stars. I was the main author of this paper and I computed, analysed and interpreted the results. The original idea of this project came from my supervisor, Saskia Hekker. I was able to identify new canditates for my sample with the help of my collaborator, Jeong Yun Choi, and developed the concept of the full dissipation framework together with Jonas Müller. All co-authors (Jonas Müller, Jeong Yun Choi and Saskia Hekker) helped me with the interpretation of the results and provided useful comments and suggestions for the text and figures.

Abstract Over ten years ago, a subset of red giants with reduced dipole-mode amplitudes was detected, the so-called suppressed dipole-mode stars. The reduced mode amplitudes indicate mode energy loss, recently confirmed to be due to additional damping in the central regions of the stars. To explain the reduced mode amplitudes (i.e. the suppression), a framework was proposed in which all the mode energy entering the inner mode cavity is dissipated. Further observational analysis of these stars challenged the full dissipation assumption revealing contributions from the inner mode cavity in the observed dipole modes. A framework considering partial dissipation has subsequently been developed. In this study, we aim to verify the validity and the extent of the framework assuming all the mode energy in the inner mode cavity to be dissipated (i.e. the full dissipation framework).

Based on the mode properties (frequencies, amplitudes and linewidths) and the visibilities of the non-radial modes of a set of about 450 suppressed dipole-mode stars, we verified three predictions of the full dissipation framework. We firstly should only detect pure pressure modes (i.e. no contribution from the central regions of the star) in the power spectrum. Secondly, we expect the visibility and the ratio of the radial-mode damping rate to non-

radial mode damping rate to be lower than unity, and we expect a linear relation between these two quantities. Finally, we can predict the visibility using an expression depending on the radial-mode damping rate, the coupling between the mode cavities and the frequency separation between radial modes and compare these predictions to the observed normalised visibility.

Analysing the power spectra of the suppressed dipole-mode stars, we find three main morphologies based on the number of dipole modes observed per acoustic radial order: the fully suppressed (no dipole modes in any acoustic radial order), p-dominated only (one dipole mode per radial order) and the partially suppressed dipole-mode stars (more than one dipole mode in at least one radial order). For the fully suppressed and p-dominated only stars, the non-radial mode properties are in line with the predictions of the full dissipation framework. The partially suppressed dipole-mode stars have quadrupole-mode properties in line with the full dissipation framework while their dipole-mode properties are not consistent with the predictions of the full dissipation framework.

We conclude that the effect and the onset of the additional damping mechanism in suppressed dipole-mode stars depends on spherical degree. Our findings indicate that a combination of full and partial energy dissipation within the same star is needed to explain the diversity observed in the suppressed dipole-mode stars. For example, the additional source of damping would cause full dissipation of the g-mode character for the quadrupole modes of a given star while it only causes partial dissipation of the g-mode character in the dipole modes of the same star.

3.1. Introduction

The *Kepler* space-borne mission (Borucki et al., 2010) provided light curves for more than 16 000 red giants (Yu et al., 2018), greatly contributing to the development of red-giant asteroseismology (see e.g. Hekker and Christensen-Dalsgaard, 2017; García and Ballot, 2019, for reviews). Red giants exhibit solar-like oscillations driven by turbulent convection in their envelope (see e.g. Houdek et al., 1999; Samadi and Goupil, 2001; Dupret et al., 2009). The non-radial oscillation modes of these stars have a mixed oscillation character; they behave like a pressure mode in the outer layers of the star (p-mode cavity) and like a gravity mode in the core regions (g-mode cavity) of the star. These modes are therefore of particular interest as they carry information about the inner and outer regions of a star. The detection of these mixed modes in red giants (Hekker et al., 2009; De Ridder et al., 2009) enabled among others the precise determination of evolutionary stages (see e.g. Bedding et al., 2011; Mosser et al., 2011b; Kallinger et al., 2012; Vrard et al., 2016) and core-rotation rates (see e.g. Beck et al., 2011; Deheuvels et al., 2014; Gehan et al., 2018).

The study of red giants performed by Mosser et al. (2012) reveals the existence of red giants with reduced dipole-mode visibility (i.e. a reduction in the mode energy in the dipole modes compared to the mode energy in the radial modes). Since the mode energy is set by the balance between excitation and damping (see e.g. Hekker and Christensen-Dalsgaard, 2017), the reduction observed in those so-called suppressed dipole-mode stars could be the result of inhibited excitation or additional damping. In their study, Coppée et al. (2024) find that the radial-mode amplitudes and linewidths of the suppressed dipole-mode stars are consistent with those of red giants with typical dipole modes. This result indicates that the radial modes are unaffected by the mechanism causing the mode suppression[1]. This means that the excitation and convective damping of the radial modes are similar in stars with typical and reduced dipole-mode amplitudes. Assuming similar excitation of all modes, Coppée et al. (2024) conclude that the mode suppression is due to additional damping.

Fuller et al. (2015) propose a theoretical framework in which the additional damping (the magnetic greenhouse effect) results in full dissipation of the mode energy entering the g-mode cavity. In this general full dissipation framework (independent of the source of the additional damping), all observed modes are pure pressure modes and the observed non-radial mode visibility is proportional to the ratio of the radial mode damping rate to non-radial mode damping rate (see Mosser et al., 2017a, and references therein). Additionally, the visibility can be expressed as a function of the average damping rate, frequency spacing of the radial modes and the coupling between the mode cavities (see Fuller et al., 2015; Mosser et al., 2017a, and references therein). Fuller et al. (2015) find that their predictions for the dipole-mode visibility in the full dissipation framework are in line with the observations of Mosser et al. (2012). Stello et al. (2016a,b) confirm the agreement between the theoretical visibility range and the observed visibilities for their sample of RGB stars with suppressed dipole modes. The theoretical predictions reproduce the reducing impact of the additional damping on the dipole-mode visibility as the star ascends the red giant branch (RGB, Stello et al., 2016a,b). Cantiello et al. (2016) extend the analysis of Fuller et al. (2015) by predicting the dipole-mode visibility for core-He-burning (CHeB) stars. Furthermore, Rui and Fuller (2023) and Cantiello et al. (2016) confirm the conclusions from Fuller et al. (2015) that the observed mode suppression can be caused by the dissipation of the mode energy in the g-mode cavity.

The validity of the full dissipation framework has however been challenged by Mosser et al. (2017a). These authors find evidence for the presence of mixed modes in the power spectra of more than a hundred suppressed dipole-mode stars. Moreover, these authors show that their observed visibility is larger than predicted in the full dissipation framework using the average damping rate and frequency spacing of the radial mode and coupling between the mode cavities. Additionally, Mosser et al. (2017a) and Arentoft et al. (2017) independently find that observed visibilities for CHeB stars are not in agreement with the predictions of Cantiello et al. (2016). Fuller et al. (2015) suggest that the stars for which the predicted visibility is lower than the observed visibility are undergoing partial mode-energy dissipation in the g-mode cavity. Such a framework was developed by Loi and Papaloizou (2017, 2018); Loi (2020); Müller et al. (2025).

In this study, we aim to verify the validity of the full dissipation framework and its extent by comparing the predictions of this framework to the features of the suppressed dipole-mode stars. To this end, we analysed the power spectra and computed the observed visibility of the non-radial modes of these stars.

In Sect. 3.2, we summarise the effects of the full dissipation framework on the mode properties of suppressed dipole-mode stars. We specify the methods we used to obtain the global asteroseismic parameters and individual mode properties in Sect. 3.3. We present the results of our tests pertaining to the validity and the extent of the full dissipation framework in Sect. 3.4 and more general results in Sect. 3.5. We dedicate Sects 3.6 and 3.7 to the discussion and the conclusions of our study.

---

[1] For clarity, we use mode suppression to describe the reduced mode amplitudes, while we refer to the mode-energy loss as dissipation.

3.2. The full dissipation framework

The main assumption in the full dissipation framework is that the mode energy entering the g-mode cavity is fully dissipated due to a strong additional damping mechanism. To determine the effects of this additional damping on the mode properties, we investigate the energy in an oscillation mode. We define for this purpose the normalised visibility v_{nl} of a non-radial oscillation mode of spherical degree l in the acoustic radial order n as

$$v_{nl} \equiv \frac{A_{nl}^2}{A_{n0}^2 \mathcal{G}_l}, \tag{3.1}$$

with A_{nl} the amplitude of the mode, A_{n0} the amplitude of the radial mode of the same acoustic radial order and $\mathcal{G}_l$ a geometrical factor depending on spherical degree, limb-darkening effects and the bolometric correction. In this study, we use the mean observed visibility of stars with typical dipole modes as the geometrical factor $\mathcal{G}_l$ in Eq. (3.3) ($\mathcal{G}_1 \approx 1.35$ and $\mathcal{G}_2 \approx 0.688$, see e.g. Mosser et al., 2012; Stello et al., 2016b). These values are roughly comparable to the theoretical mode visibilities computed by Ballot et al. (2011) for pure p-modes considering the spectral response function of the *Kepler* instrumentation.

We interpret the normalised visibility (Eq.(3.1)) as a measure of the energy of a mode of spherical degree l relative to the energy of the radial mode in the same acoustic radial order. If the effect of the damping in the central regions of the star is negligible, Mosser et al. (2012, 2017a) show that the total normalised visibility v_{nl} for an acoustic radial order n is equal to

$$\mathrm{v}_{nl} \equiv \sum_{i=1}^{\mathcal{N}} v_{nl}^i = 1, \tag{3.2}$$

where v_{nl}^i is the normalised visibility of mixed mode i in the acoustic radial order and $\mathcal{N}$ the number of mixed modes in the considered acoustic radial order. This result implies that all the mixed modes of degree l associated with the acoustic radial order of the radial mode have a combined mode energy (not considering core damping) similar to the radial mode of the same acoustic radial order. In other words, we do not expect the total normalised visibility v_{nl} to be larger than unity. Moreover, Eq. (3.2) implies that any additional form of damping results in a lower total normalised visibility (i.e. $\mathrm{v}_{nl} < 1$). This means that the total normalised visibility should always be smaller than unity in the full dissipation framework as we assume a strong additional source of damping to cause the dissipation.

To aid in the application of the visibility measurements in observed stars, we further define the normalised visibility of a star v_l as the weighted average (i.e. weighted by the energy in the radial modes) of the visibility of the five acoustic radial orders closest to the frequency of maximum oscillation power $\nu_{\max}$ (see Sect. 3.3):

$$v_l \equiv \sum_{k=n_{\max}-2}^{n_{\max}+2} w_k \frac{A_{kl}^2}{A_{k0}^2 \mathcal{G}_l}\ , \tag{3.3}$$

with $w_k = A_{k0}^2/A_0^2$ the fractional contribution of each radial mode to the total radial-mode power A_0^2 (i.e. the sum of the squared radial-mode amplitudes of the five most central acoustic radial orders) and $n_{\max}$ the acoustic radial order closest to $\nu_{\max}$. We note that Eq. (3.3) is equivalent to the ratio of the total mode energy in the modes with spherical degree l to the total mode energy in the radial modes.

3.2.1. Normalised visibility as a function of linewidth ratio

Benomar et al. (2014) derive an expression relating mode amplitude, mode inertia I_{nl} and mode linewidth Γ_{nl} of a non-radial mode of spherical degree l to those of the closest radial mode in the same radial acoustic order n:

$$A_{nl}^2 I_{nl}^2 \Gamma_{nl} = A_{n0}^2 I_{n0}^2 \Gamma_{n0} \mathcal{G}_l. \tag{3.4}$$

The full dissipation of the mode energy entering the g-mode cavity implies that we only observe one mode of spherical degree l per acoustic radial order as the observed modes do not have a mixed character. In other words, all the observed oscillation modes in this framework are pure pressure modes. We can therefore assume for these modes that $I_{nl} \simeq I_{n0}$ (see e.g. Mosser et al., 2017a). Using this assumption and Eq. (3.4), we rewrite Eq. (3.1) as

$$v_{nl} = \frac{A_{nl}^2}{A_{n0}^2 \mathcal{G}_l} = \frac{\Gamma_{n0}}{\Gamma_{nl}} \left(\frac{I_{n0}}{I_{nl}} \right)^2 \simeq \frac{\Gamma_{n0}}{\Gamma_{nl}}. \tag{3.5}$$

Similarly as for the normalised visibility of a star (Eq. (3.3)), we compute the linewidth ratio Γ_0/Γ_l of a star as

$$\frac{\Gamma_0}{\Gamma_l} \equiv \sum_{k=n_{\max}-2}^{n_{\max}+2} w_k \frac{\Gamma_{k0}}{\Gamma_{kl}} \, . \tag{3.6}$$

Combining Eqs (3.3), (3.5) and (3.6), we expect the normalised visibility of pure pressure modes to be equal to the ratio of the radial-mode linewidth to the non-radial mode linewidth:

$$v_l = \frac{\Gamma_0}{\Gamma_l}. \tag{3.7}$$

From the results of Mosser et al. (2012, 2017a), we expect the visibility to be equal to 1 if we only consider surface damping. Following our definitions and Eq. (3.7), the linewidth ratio should also be equal to 1. We can understand this when we consider the relation between the mode linewidth and the mode damping rate ($\eta_l = \pi \Gamma_l$, see e.g. Houdek et al., 1999; Hekker and Christensen-Dalsgaard, 2017). If we neglect the contribution of the core damping (similarly as for Eq. (3.2)), the mode damping rate η_l of a non-radial pure pressure mode is close to the radial-mode damping rate η_0 (i.e. $\eta_l \simeq \eta_0$). We therefore expect that in the case of no additional damping the visibility of pure pressure modes given by Eq. (3.7) is equal to

$$v_l = \frac{\Gamma_0}{\Gamma_l} = \frac{\eta_0}{\eta_l} \simeq 1. \tag{3.8}$$

To derive Eq. (3.8), we only assumed that all modes are pure pressure modes. However, in the full dissipation framework, the pure pressure modes are the result of an additional source of damping. We therefore expect in this framework that the mode damping rate of the non-radial mode is larger than in the case of only surface damping ($\eta_l > \eta_0$). This means that the linewidth ratio defined in Eq. (3.6) should be smaller than unity in the full dissipation framework. We therefore predict that the total normalised visibility and the linewidth ratio are directly related to each other (i.e. due to their pure pressure-mode character) and both smaller than one (i.e. due to the additional source of damping).

3.2.2. Normalised visibility as a function of the radial-mode properties and the coupling between mode cavities

Using the relation between mode linewidth and mode-damping rate, we find from Eq. (3.5) that

$$v_{nl} \simeq \frac{\Gamma_{n0}}{\Gamma_{nl}} = \left(\frac{\eta_{nl}}{\eta_{n0}}\right)^{-1} = \left(\frac{\eta_{nl}}{\pi\Gamma_{n0}}\right)^{-1}. \tag{3.9}$$

Takata (2016) derive an expression for the damping rate η_{nl} of non-radial modes in the case of energy leaking into the g-mode cavity and being dissipated. This expression for the damping rate depends on the coupling factor q_l (i.e. how strongly the mode cavities couple which acts as a proxy for the fraction of energy transmitted to the g-mode cavity) and the large frequency separation $\Delta\nu$ (see Sect. 3.3). Introducing the expression for the damping rate, we obtain the general expression for the average normalised visibility v_l (see our Eq. (3.3), and also Mosser et al., 2017a):

$$v_l \simeq \left[1 - \ln\left(\frac{1-q_l}{1+q_l}\right)\frac{\Delta\nu}{\pi\Gamma_0}\right]^{-1}. \tag{3.10}$$

In the limit of a thick evanescent zone (i.e. $q_l \ll 1$, see e.g. Unno et al., 1989, for more information), the expression in Eq. (3.10) becomes

$$v_l \simeq \left(1 + \frac{2q_l\Delta\nu}{\pi\Gamma_0}\right)^{-1} = (1 + 4q_l\Delta\nu\tau)^{-1}, \tag{3.11}$$

with the radial-mode lifetime $\tau = (2\pi\Gamma_0)^{-1}$ (see Fuller et al., 2015; Mosser et al., 2017a, and references therein).

3.3. Frequency analysis

Here we provide a description of the methods we used to obtain the global asteroseismic parameters (i.e. $\nu_{\max}$ and $\Delta\nu$) and individual mode properties (i.e. the mode frequency ν_{nl}, the mode linewidth Γ_{nl}, and the mode amplitude A_{nl}) needed to compute the different definitions of normalised visibility. We performed the frequency analysis of the light curves of the stars in our sample with our peakbagging code TACO (Tools for the Automated Characterisation of Oscillations, Hekker et al., in prep.).

Firstly, we fitted the power density spectrum (PDS) with a global model comprising the broad contribution of the oscillations and of the background (see Kallinger et al., 2014, for more details):

$$P_{\mathrm{B}}(\nu) = P_{\mathrm{n}} + \mu(\nu)^2\left(P_{\mathrm{bgr}}(\nu) + P_{\mathrm{g}}\exp\left[-\frac{(\nu-\nu_{\max})^2}{2\sigma_{\mathrm{env}}{}^2}\right]\right). \tag{3.12}$$

Here, P_{n} is the white noise and $\mu(\nu)$ the apodization[2] (the attenuation resulting from the fact that the integration times are not infinitely short). The stellar contribution to the background signal $P_{\mathrm{bgr}}(\nu)$ is modelled with three granulation components (see e.g. Kallinger et al., 2014). The contribution from the oscillations called the oscillation power envelope is described with a Gaussian function. The centre of the power envelope $\nu_{\max}$, called the frequency

---

[2] The apodization is typically represented by $\eta(\nu)$, here a different symbol has been chosen as to not be confused with the mode-damping rate.

of maximum oscillation power, is an important global seismic parameter. The other two parameters, P_g and σ_env, are respectively the height and standard deviation of the oscillation power envelope.

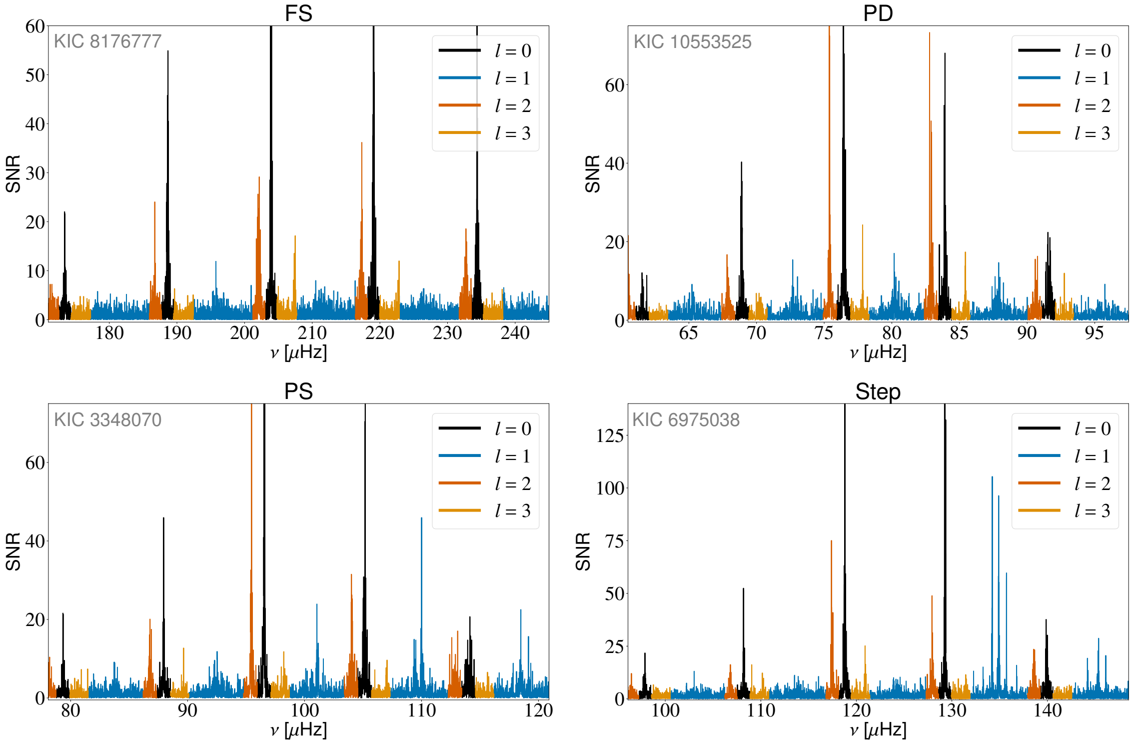

Figure 3.1: Typical examples of morphology categories as observed in the PDS of RGB suppressed dipole-mode stars: Full suppression (FS, top-left), P-dominated modes only (PD, top-right panel), Partial suppression (PS, bottom-left panel), and Step suppression (Step, bottom-right panel). See text for more details of the definition of the morphologies.

Secondly, we applied the peak detection method developed by García Saravia Ortiz de Montellano et al. (2018) to detect the resolved and unresolved modes in the PDS normalised by the background model (terms $P_\mathrm{n} + \mu^2 P_\mathrm{bgr}$ in Eq. (3.12)). To each individual resolved mode we fitted a Lorentzian function

$$P_{nl}(\nu) = \frac{2A_{nl}^2}{\pi\Gamma_{nl}} \frac{1}{1 + \left(\frac{2(\nu-\nu_{nl})}{\Gamma_{nl}}\right)^2}, \tag{3.13}$$

with ν_{nl}, A_{nl} and Γ_{nl} the central frequency, mode amplitude and mode linewidth (i.e the full-width at half maximum of the peak). To each unresolved mode we fitted a squared sinc function

$$P_{nl}(\nu) = \frac{A_{nl}^2}{\delta\nu} \operatorname{sinc}^2\left(\pi\frac{\nu-\nu_{nl}}{\delta\nu}\right), \tag{3.14}$$

with $\delta\nu$, the frequency resolution of the power spectrum. We optimised the fit with a Maximum Likelihood Estimation and obtain an estimate of lower limits of the uncertainties for each peak from the Hessian matrix.

Lastly, we identified the radial, quadrupole and octupole modes starting from the central radial order using the Universal Pattern (UP, Mosser et al., 2011b) as a guide and eventually determined $\Delta\nu$ (large frequency separation between successive radial modes) from a linear fit through the identified radial modes.

3.4. Testing the predictions of full dissipation framework

To test the validity and the extent of the full dissipation framework, we used the stars selected by Coppée et al. (2024). In addition, we also incorporated all suppressed dipole-mode stars from Arentoft et al. (2017) as well as a set of potential suppressed dipole-mode stars from the APOKASC2 catalogue (Pinsonneault et al., 2018) identified using the Shannon entropy (Shannon, 1948) of their power density spectra (see Choi et al., subm., for more information). For this study, we computed the normalised visibility of the dipole and quadrupole modes of the stars in our sample (i.e. Eq. (3.3)), as well as visibility thresholds, below which only suppressed dipole-mode stars are found (see also Coppée et al., 2024).

In Sect. 3.2, we highlighted three main observable implications of the additional source of damping in the full dissipation framework. We expect to not observe mixed non-radial modes (i.e. only one mode of degree $l > 0$ per acoustic radial order). For this one mode, the normalised visibility is expected to be smaller than one and to be proportional to the ratio of the radial-mode linewidth to the non-radial mode-linewidth (Eq. (3.7)). We can furthermore confront our measurements to the predicted normalised visibility based on the radial-mode linewidth, large frequency separation and the coupling factor. Here, we assess the validity of the full dissipation framework for suppressed dipole-mode stars by verifying if these three implications hold for these stars.

3.4.1. Mixed dipole-mode detection

Our first test of the full dissipation framework involves the detection of mixed non-radial modes in the power spectra of suppressed dipole-mode stars. To facilitate the presentation of our results in the remainder of this paper, we divided our sample in three main PDS morphology categories (see Fig. 3.1) based on the number of dipole modes per radial acoustic order observed in the PDS of the star: no dipole modes (full suppression or FS category), one dipole mode (pressure-dominated dipole modes or the PD category) or at least two dipole modes (partially suppressed dipole-mode stars or PS category) We define these categories in the following paragraphs.

3.4.1.1 Full suppression (FS)

For this type of PDS morphology, we do not detect any significant modes in the predicted dipole-mode frequency range in contrast with the radial-, quadrupole- and octupole-mode frequency ranges (see top-left panel of Fig. 3.1). We categorise all stars where no dipole mode is detected in any of the five most central acoustic radial orders as fully suppressed. It is important to note that this morphology is only observed in RGB stars and not in CHeB stars.

3.4.1.2 Pressure-dominated dipole modes only (PD)

In the spectra of the stars in this category, we find clear signatures of one dipole mode per radial order (see top-right panel of Fig. 3.1). We consider stars with exactly one mode (and never more than one) in one or more acoustic radial order for our PD category.

From the asymptotic theory we know that the coupling between mode cavities as well as glitches can cause the frequencies of mixed modes to differ from the asymptotic frequencies (see Mosser et al., 2017a, and references therein for more information). The observed modes can therefore be considered as pure p-modes if, within uncertainty, the observed and asymptotic pure p-mode frequencies are consistent with each other. To this end, we computed the asymptotic pure p-mode frequencies using the UP. We fitted these frequencies to the observed frequencies to obtain an estimate of the small frequency separation between radial and nominal dipole modes $\delta\nu_{01}$ (see e.g. Mosser et al., 2011b). The residuals of the fit of asymptotic frequencies to the observed frequencies are shown in units of $\Delta\nu$ in Fig. 3.2 for a typical star in the PD category. Similar to Mosser et al. (2017a), we use a typical uncertainty due to the noise contribution (highlighted areas in Fig. 3.2) to determine the agreement between observed and asymptotic frequencies and so whether these stars belong in the PD category.

3.4.1.3 Partial suppression (PS)

Stars in this category show the typical set of radial and non-radial modes, with reduced power in the non-radial modes (see bottom-left panel of Fig. 3.1). We categorised stars as PS if we detected at least two dipole modes in one of the five most central acoustic radial orders (i.e. closest to $\nu_{\max}$).

3.4.1.4 Step suppression (Step)

In our sample, two RGB stars have a peculiar morphology combining PS and FS morphology: we find no significant dipole modes below a threshold frequency and significant dipole modes with reduced power above this frequency for two stars (see bottom-right panel of Fig. 3.1). This step-suppression (Step) morphology should be interpreted as a special case within the PS category. These stars were first detected by eye and confirmed by comparing the behaviour of the visibility per radial order as a function of frequency.

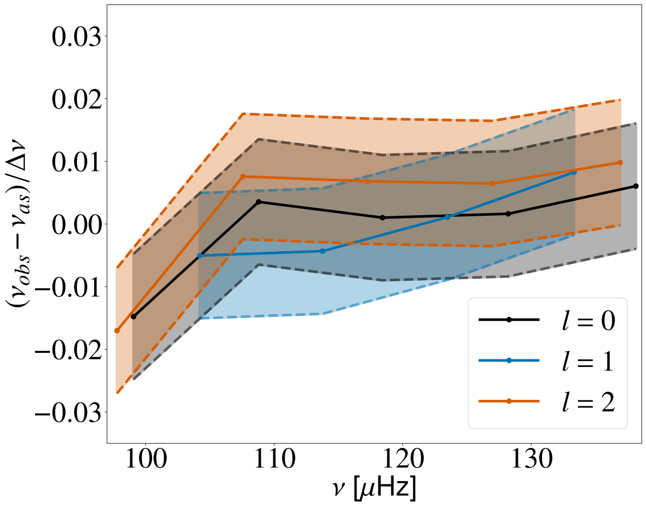

Figure 3.2: Difference between observed and asymptotic frequency of pure p-modes as a function of mode frequency for spherical degrees $l = 0, 1, 2$ (in black, blue and orange respectively). We highlight the noise-uncertainty intervals for each spherical degree.

We find that about 10% of our stars are categorised as FS stars and almost 10% of the stars in our sample (1 CHeB and 38 RGB stars) are PD stars. Furthermore, the fact that no dipole modes were detected in the PDS of the FS stars indicates that a strong additional damping is occuring in the core. From Eq. (3.7), strong additional damping ($\eta_l \gg \eta_0$) would indeed result in a very low mode visibility ($v_l \ll 1$). The stars in the FS and PD category can thus be described within the full dissipation framework. However, we detected mixed dipole modes in the remaining 80% of our sample, the PS stars. The detection of mixed modes in the PDS of the PS stars provides an indication that the full dissipation framework is not valid for these stars.

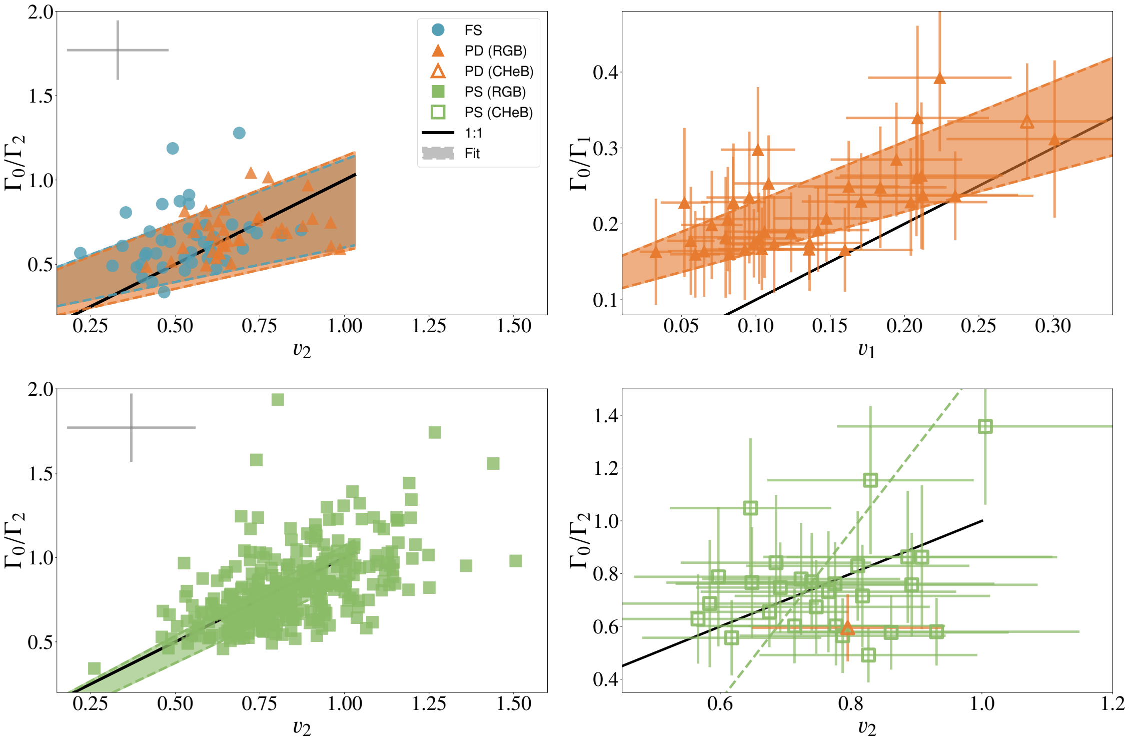

Figure 3.3: Weighted linewidth ratio of non-radial to radial mode as a function of the observed normalised visibility. *Top-left:* quadrupole-mode properties of the RGB stars in the FS and PD category. *Top-right:* dipole-mode properties of the stars in the PD category (RGB and CHeB stars indicated by full and open markers). *Bottom-left:* quadrupole-mode properties of the RGB stars in the PS category. *Bottom-right:* quadrupole-mode properties of the CHeB stars in the PD and PS category. We highlight the one-to-one proportionality expected in the full dissipation framework (black solid line) and the measured slope m (dashed lines and highlighted areas set by a 1 sigma uncertainty). Because of the large uncertainty on m and c for the quadrupole-mode properties of the PS CHeB stars, we only show the results of the linear fit (without highlighting the area set by the uncertainties on the fit parameters). The typical uncertainty on the measurements is shown in the top-left corner of the panels for the RGB stars (i.e. left column).

3.4.2. Comparison with linewidth ratios

The second test of the full dissipation framework consist of comparing the observed normalised visibility v_l with the linewidth ratio Γ_0/Γ_l. According to Eq. (3.7) the normalised visibility is directly proportional to the linewidth ratio for pure pressure modes. Moreover, any additional source of damping will reduce the normalised visibility v_l. In the case of full dissipation, we therefore not only expect that the constant of proportionality is close to 1, but also that the values of the linewidth ratio and the normalised visibility are smaller than 1. This constant of proportionality can be seen as the slope m of a linear fit with the intercept c set to zero. However, considering the uncertainties on the normalised visibility and linewidth ratios, we fitted a linear relation with a non-zero intercept $g(x) = mx + c$ to the datapoints (see Table 3.1) to estimate the constant of proportionality. We also computed the Pearson correlation coefficient (Pearson, 1895, see Table 3.1) to assess the linearity of the relation between normalised visibility and linewidth ratio.

3.4.2.1 FS category

Our average linewidth ratios of the quadrupole modes (Γ_0/Γ_2) are in line with the observed quadrupole-mode visibility v_2 (see top-left panel in Fig. 3.3) for most of the FS stars. Two stars have a high linewidth ratio (i.e. larger than one). These stars have narrow and weaker quadrupole modes due to a low signal-to noise level. These narrow quadrupole modes directly impact the average linewidth ratio. The values of v_2 and Γ_0/Γ_2 of all FS stars are consistent within three sigmas with the one-to-one relation and these values are predominantly smaller than one. From this, we deduced that the linewidth ratio and normalised quadrupole-mode visibility of the FS stars seem to be in line with the predictions of the full dissipation framework.

Table 3.1: Results of the linear fit and correlation coefficient for the different morphologies and mode degrees.

PDS morphology	m	c	Correlation
FS (l = 2, RGB)	0.58± 0.17	0.28± 0.09	0.25
PD (l = 1, RGB)	0.66± 0.13	0.13± 0.02	0.66
PD (l = 2, RGB)	0.62± 0.17	0.24± 0.11	0.31
PS (l = 2, RGB)	1.01± 0.06	-0.05± 0.05	0.55
PS (l = 2, CHeB)	3.2± 1.3	-1.6± 1.0	0.30

3.4.2.2 PD category

For the dipole modes of the stars in the PD category, the correlation coefficient indicates that the correlation is strong (see top-right panel in Fig. 3.3). At the low observed dipole-mode visibilities, it becomes complex to distinguish between narrow features and the global shape of a mode. In some cases, the procedure for the mode-fitting only considers these narrow features which results in smaller linewidths and amplitudes. This in turn translates into a larger linewidth ratio and smaller observed visibility. We therefore see a larger number of PD stars in that part of the parameter space (see very low visibility part of the top-right panel in Fig. 3.3). All observations for the dipole modes of the stars in the PD category are consistent within three sigmas with the predicted one-to-one line (black solid line), are all smaller than one and the correlation is strong. We conclude that our dipole-mode properties are in line with the predictions of the full dissipation framework.

Our linewidth ratio (Γ_0/Γ_2) and observed visibility v_2 of the PD stars are consistent within three sigmas with the predicted one-to-one relation. The slope m as well as well as c indicate that the relation between the average linewidth ratio (Γ_0/Γ_2) and the observed visibility v_2 (see top-right panel in Fig. 3.3) is in line with the predicted relation in the full dissipation framework. From our results for the quadrupole modes, we conclude that our quadrupole-mode properties of the stars in the PD category are consistent with the predictions in the full dissipation framework.

Our observed dipole-mode and quadrupole-mode properties for the stars in the PD category seem to indicate that these stars can be described within the full dissipation framework.

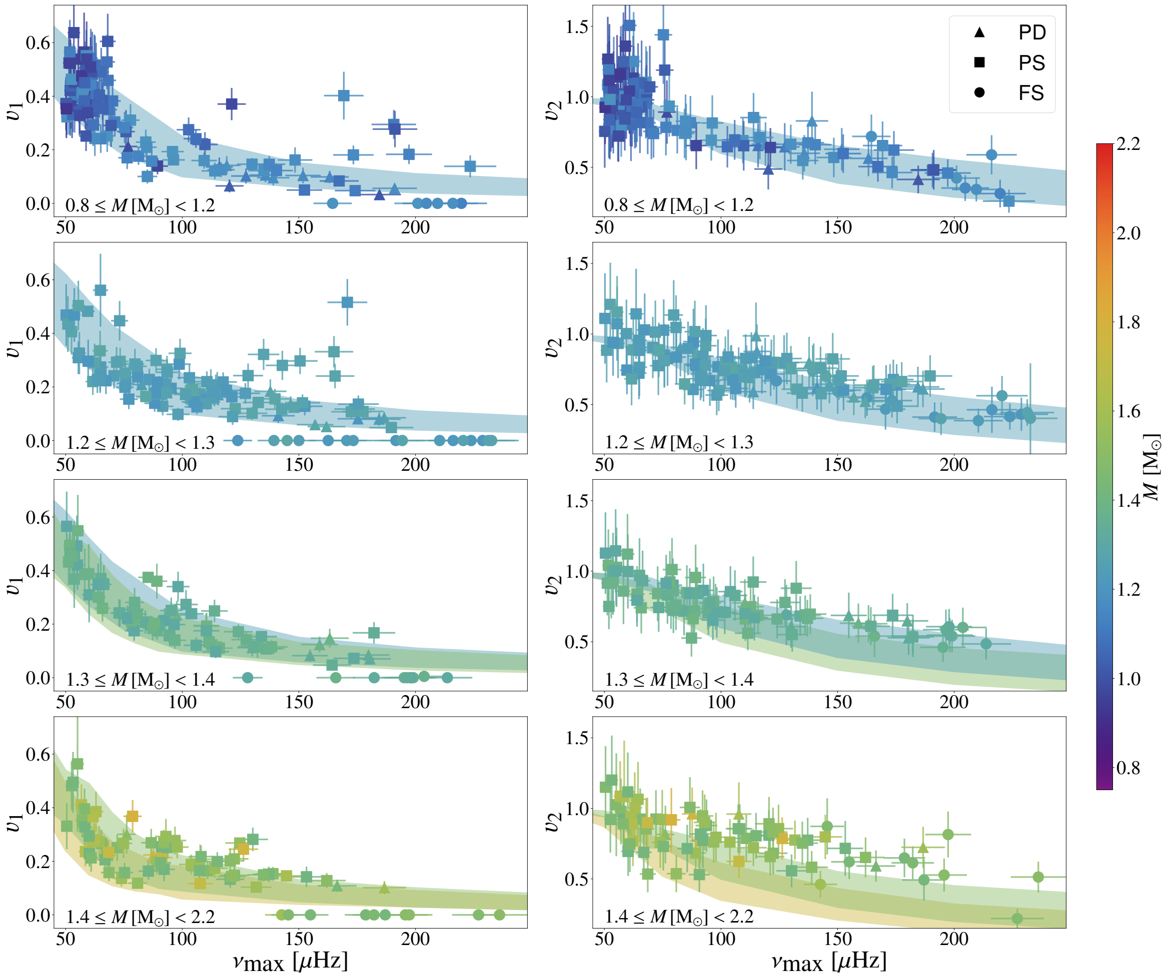

Figure 3.4: Normalised visibility v_1 (left column) and v_2 (right column) as a function of $\nu_{\max}$ for the RGB stars in our sample, colour-coded by mass. For clarity, we subdivided our sample in mass bins (increasing mass from top to bottom). The highlighted regions show the predicted visibility ranges from Cantiello et al. (2016) for a mass of 1.25 (blue), 1.5 (green) and 1.75 (ochre) M$_\odot$.

3.4.2.3 PS category

The observed quadrupole-mode visibility v_2 and the average linewidth ratio of radial and quadrupole modes are close to the one-to-one line for PS stars in the RGB and CHeB phase (see bottom panels in Fig. 3.3 and Table 3.1). The correlation is more pronounced for the RGB stars (see Table 3.1). The fit parameters m and c for the PS RGB stars are consistent with their expected values within one sigma, confirming that our measurements are in agreement with the one-to-one line. In addition to m and c, we find that normalised visibility and linewidth ratio of the quadrupole modes for each star in the PS category are consistent within three sigma with the one-to-one relation. We therefore conclude that the quadrupole-mode properties of the PS RGB stars in line with the predictions of the full dissipation framework.

Due their low number of CHeB stars in the PS category and the fact that the measurements of these stars are grouped together, a linear fit is not really meaningful. Since we find that normalised visibility and linewidth ratio of the quadrupole modes for each star in the PS category are consistent within three sigma with the one-to-one relation and that their values are predominantly smaller than one, we conclude that our results for the quadrupole modes of the PS CHeB stars are in agreement with the predictions in the full dissipation framework.

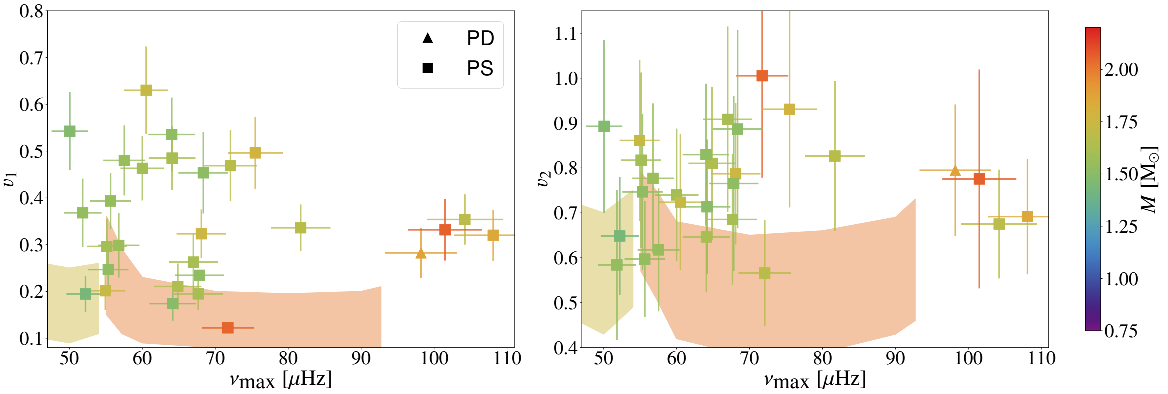

Figure 3.5: Same as in Fig. 3.4, now for the CHeB stars in our sample. The coloured highlighted regions show the predicted visibility ranges from Cantiello et al. (2016) for a mass of 1.75 (ochre) and 2 M$_\odot$ (red).

For about one quarter of the PS stars (typically at low $\nu_{\rm max}$), we find that, within two sigmas, their linewidth ratio and visibility of the quadrupole modes are close to unity. These two quantities are expected to be close to unity for pure pressure quadrupole modes only affected by convective damping (see Sect. 3.2 as well as Mosser et al., 2017a, and references therein). Our results thus indicate that the quadrupole modes of these stars are not strongly, if at all, affected by the additional source of damping. As their linewidth ratio and visibility still follow the predicted behaviour of pure pressure modes, it suggests that the quadrupole modes in these stars are pure pressure modes.

3.4.2.4 Significance of correlation coefficients

The Pearson correlation coefficient measures if the relationship between two quantities is linear (Pearson, 1895). To determine the significance of the correlation coefficient (and the linear relationship) for the different PDS categories. We constructed for each subsample, 2000 realisations of the observed visibilities and linewidth ratios by perturbing these parameters within their uncertainties (i.e. with a Monte Carlo approach). We then computed the correlation coefficients for each realisation. We always find correlation coefficients larger than zero indicating a positive linear relationship between the observed visibility and linewidth ratio. We also computed the p-value of the Kolmogorov-Smirnov test (Hodges, 1958) i.e. the probability that the correlation coefficient is zero (the null hypothesis). We find that in more than 70% of the realisations we can reject the null hypothesis (p-value below 5%), confirming that the correlation coefficient is most likely non-zero.

3.4.3. Comparison with predicted visibility

The third test of the full dissipation framework is the comparison between the observed normalised visibility and the predicted visibility ranges based on asteroseismic observables (i.e. Eqs (3.10) or (3.11)). We show the normalised dipole- and quadrupole-mode visibility of the RGB and CHeB stars in our sample as a function of $\nu_{\max}$ in Figs 3.4 and 3.5. In addition to the observed visibilities, we also show the predicted visibility ranges from Cantiello et al. (2016). We note that these predictions are based on the assumption of a thick evanescent zone (i.e. Eq. (3.11)), thought to be valid only for the most evolved RGB stars (i.e. low $\nu_{\max}$ RGB stars, see e.g. Pinçon et al., 2020). The general expression (Eq. (3.10)) derived using the formalism of Takata (2016) should be valid for all red giants. The visibilities predicted using this general expression or in the thick-evanescent region limit are consistent within the reported uncertainties (see Mosser et al., 2017a, using their own observed q_l for both expressions). Our conclusions should therefore be independent of the selected expression to compute the predicted visibility (for the same coupling factor q_l). However, we note that the estimate of q_l from models considering the general formalism for the coupling (e.g. Takata, 2016) may differ significantly from the observed q_l. Considering this formalism for the coupling will consequently affect the predicted visibility (i.e. through Eq. (3.10)).

3.4.3.1 RGB stars

By definition the visibility of stars in the FS category is zero (i.e. no detected dipole modes). The true normalised visibility is most likely very small but not necessarily zero. These cases of very strong suppression do not seem to fit within the predicted visibility ranges from Cantiello et al. (2016). This is most likely due to the fact that Eq. (3.11) can never be zero for any finite values of Γ_0, $\Delta\nu$ and q_1. From Eq. (3.10), we expect a zero visibility in the limit of total coupling between the mode cavities ($q_l = 1$). The observed quadrupole-mode visibility of the FS stars are in turn larger than predicted from Eq. (3.11) for the higher mass stars in the FS category (see the bottom-right panel in Fig. 3.4). The quadrupole-mode visibility for these higher mass stars are in line with the predicted range within two sigmas.

We find that the dipole-mode visibility measurements of the RGB stars in the PD category are within the predicted range from Eq. (3.11) (see left column of Fig. 3.4). In other words, the observed values for the visibility of these stars are consistent with the predictions in the full dissipation framework (in the thick evanescent zone limit). Similarly as for the dipole modes, our observed quadrupole-mode visibilities are in line with the predictions of Cantiello et al. (2016) within two sigmas (see right column of Fig. 3.4).

Most of the stars in the PS category (about 90%) fall within the predicted dipole-mode visibility range, especially at lower $\nu_{\max}$ (i.e. more evolved RGB stars, see Fig. 3.4). Although their PDS morphology suggests that the full dissipation framework is not valid for these stars, their observed visibility seems to be impacted similarly as expected in the full dissipation framework. The higher than predicted visibilities for the remaining 10% of PS stars also suggest the presence of a mechanism that can cause partial dissipation of the energy in the g-mode cavity of RGB stars as proposed by Mosser et al. (2017a). We indeed expect dipole modes to retain their mixed character in the case of partial dissipation and thus to have more energy (i.e. larger mode amplitudes and thus higher visibility) than in the full dissipation framework. The interplay between the efficiency of the damping mechanism (determining how much mode energy is dissipated) and the coupling factor (determining how much mode energy enters the g-mode cavity) therefore predominantly influence the properties of the stars in the PS category.

3.4.3.2 CHeB stars

For the CHeB stars in our sample (see both panels of Fig. 3.5), our dipole-mode and quadrupole-mode visibility measurements are not in agreement with the predictions from Cantiello et al. (2016) (except for one PS star). This inconsistency is most likely due to the fact that the weak coupling assumption is not valid for CHeB stars (see e.g. Hekker et al., 2018). A similar discrepancy between predicted and observed dipole-mode visibility for CHeB stars has already been pointed out by Mosser et al. (2017a) and Arentoft et al. (2017). Additionally, we also do not find CHeB stars in the FS category, although we expect stronger coupling between the mode cavities than on the RGB.

3.5. Comparison mass and rotation distributions with literature values

In this section, we highlight our results that do not directly relate to the full dissipation framework. These results are set in the context of previous studies in the literature (e.g. Fuller et al., 2015; Cantiello et al., 2016; Stello et al., 2016b; Mosser et al., 2017a).

3.5.1. Mass distribution

We computed the asteroseismic masses with the scaling relation using the reference values from Themeßl et al. (2018). We found that our distribution peaks around 1.25 $M_\odot$ and contains masses up to 1.8 $M_\odot$ (see green histogram in Fig. 3.6). The previously reported mass distributions for RGB stars (Stello et al., 2016a; Mosser et al., 2017a) peak around 1.6 $M_\odot$ and are almost not populated below 1.3 $M_\odot$ (see orange histogram with masses from Stello et al., 2016a). The main difference between the studies is the choice of the reference values (from Themeßl et al., 2018; Mosser et al., 2013, or solar reference values). Several studies on binary systems suggest that the reference value for the large frequency separation should be lower than previously presumed (see e.g. Hekker, 2020, for an overview of reference values). We also compared our distribution with the distribution based on the masses from Hon et al. (2024) (blue histogram). For their grid-based emulator approach, the authors used the masses from Yu et al. (2018) (grey histogram). For the subset of stars that are in both samples, we find that the mass estimates are similar. The distribution of this subset of stars computed with their mass estimates peaks around 1.35 $M_\odot$. All these results suggest that the previously reported masses are an overestimation of the true stellar mass.

3.5.2. Rotation

We only observe rotational splittings in a small fraction of the set of partially suppressed dipole-mode stars (less than 8%). Evidently, we do not expect observable rotation signatures in the FS morphology. We potentially could detect rotational signatures in the PDS of PD stars. However, their modes would mainly affected by the rotation in the outer regions of the star (see e.g. Goupil et al., 2013). From observations the rotation rates in the outer regions of the stars are lower than the core rotation rates (see e.g. Deheuvels et al., 2014). We therefore expect small rotational signatures in the PDS of PD stars and at the observed low visibility they are most likely not observable. The overall observed fraction of stars showing rotation in our sample is thus most likely an underestimate of the true fraction of stars with a typical rotation rate. Based on the work from Gehan et al. (2018), we expect a significantly larger number of stars showing rotational evidence in their power spectra (about 15% of their stars).

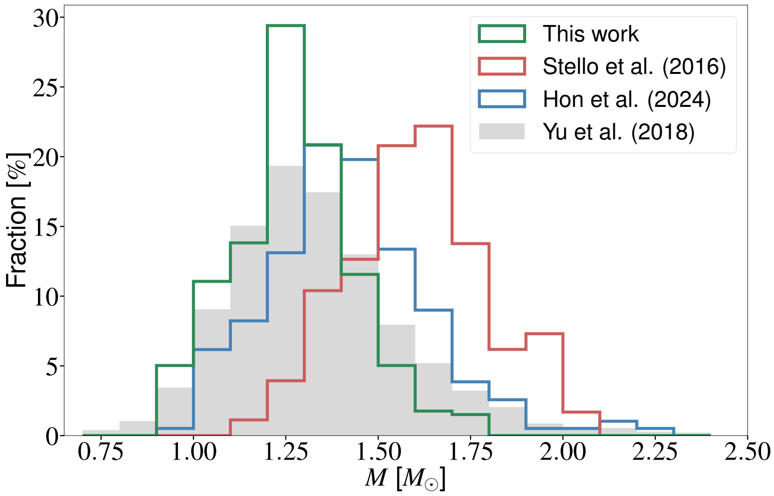

Figure 3.6: Mass distribution for the RGB stars in our sample obtained from scaling relation with reference values from Themeßl et al. (2018, in green), from masses published by Stello et al. (2016a, in orange) and Hon et al. (2024, in blue). The overall mass distribution of RGB stars from Yu et al. (2018, in grey) is shown in the background.

3.6. Discussion

3.6.1. Visibility measurements in the literature

We compared our observed visibility and radial-mode linewidths with previous observations (Mosser et al., 2012; Stello et al., 2016a,b; Mosser et al., 2017a). We find that our observations are comparable to the visibility measurements found in the literature (see Appendix B.1). We note that these previous studies computed visibility by integrating the PDS over the frequency ranges relevant for the different spherical degrees. The comparison with these studies therefore also confirms that our method to determine the visibility using fitted amplitudes is valid. A major difference with literature values is that our approach can not result in a negative visibility (see e.g. Stello et al., 2016b). The stars with negative values in the literature were found to be part of the FS (Full Suppression) category (i.e. very low visibility).

Mosser et al. (2017a) find a discrepancy between their observed and predicted v_1. They compute the predicted visibility for the stars in their sample from both the general expression and the expression in the thick evanescent zone limit (i.e. Eqs (3.10) and (3.11)) using their observed Γ_0, $\Delta\nu$ and q_1. The authors even obtained rotational splittings and period spacings for a vast majority of the stars in their sample. Their results indicate that the dipole-mode properties of their set of stars cannot be described within the full dissipation framework. We find that the RGB stars from the set of 71 stars for which they obtained coupling factors are all part of the PS category. We therefore confirm that for the dipole modes of these stars the full dissipation assumption breaks down. However, for about one third of these stars, we find that their observed visibility is within one sigma of the predicted visibility range from Cantiello et al. (2016). If we rewrite Eqs (3.10) and (3.11) to compute the coupling factor q_l that is needed to match the observed visibility, we find values below the observed range of coupling factors on the RGB (see e.g. Mosser et al., 2017b). These stars are an example of the theoretical case where the combined effect of efficiency of the damping and the coupling between the mode cavities have to be considered to properly describe the observations of the stars in the PS category. In other words, we need to investigate these stars within the partial dissipation framework (see e.g. Müller et al., in prep.). Our results as well as the results by Mosser et al. (2017a) also show that visibility alone is not enough to constrain the additional damping mechanism at play in suppressed dipole-mode stars.

3.6.2. Quadrupole-mode properties consistent with full dissipation framework

In previous studies in the literature, it has been shown that the additional damping mechanism is related to the coupling between the mode cavities (Stello et al., 2016a,b) and that its onset is frequency-dependent (so-called step suppression, see bottom-right panel of Fig. 3.1 and Mosser et al., 2017a). In this study, we furthermore find that the quadrupole-mode properties of almost all RGB stars in our sample can be described by the full dissipation framework, even if the dipole-mode properties of the star do not fit within this framework. Our results thus suggest that the efficiency of the additional damping mechanism depends on the spherical degree of the considered modes. Additionally, we can also conclude from our results that when the dipole-mode properties of a star are consistent with the predictions of the full dissipation framework, so are the quadrupole-mode properties of the same star. This means that the onset of the additional damping mechanism is also degree-dependent, which is consistent with theoretical predictions for different implementations of the source of additional damping (e.g. Fuller et al., 2015; Loi, 2020; Müller et al., 2025).

3.6.3. Comparison with linewidth ratios of radial to quadrupole modes

When comparing the linewidth ratio and normalised visibility of quadrupole modes for the different PDS categories (see Section 3.4.2), we find that these properties are almost always in line with the properties of pure pressure modes. Because of the weak coupling for the quadrupole modes, it is not straightforward to resolve the (potential) mixed quadrupole modes and in particular the g-dominated quadrupole modes. We therefore expect that the observed properties are predominantly determined by the properties of the p-dominated quadrupole modes. This explains why even at visibilities close to unity the properties of the quadrupole modes are in line with those of pure quadrupole pressure modes.

In the full dissipation framework we expect that the additional damping will reduce the observed visibility and increase the linewidth of the quadrupole modes (as linewidth is directly related to the mode damping rate). The linewidth of a mode can however also be broadened by the contribution of unresolved mixed modes or rotational multiplets. We previously mentioned that the coupling is supposedly weak and that rotational features are less frequently observed than expected for typical red giants, suggesting that these contributions are small. We furthermore expect that at lower visibility, these additional contributions to the observed linewidth will be affected more strongly and therefore be negligible in comparison to the contribution of additional damping experienced by the p-dominated quadrupole mode.

3.6.4. Relation between morphology and evolution along the RGB

We show the distribution of the different morphologies in Fig. 3.7 for different $\nu_{\max}$-regimes. The stars in the FS category are mainly located at high $\nu_{\max}$ values (dominant morphology for $\nu_{\max} \geq 140\,\mu\mathrm{Hz}$). At lower $\nu_{\max}$ in our sample ($50\,\mu\mathrm{Hz} \leq \nu_{\max} < 100\,\mu\mathrm{Hz}$) the PS category dominates the distribution. We find the stars from the PD category mainly at the higher $\nu_{\max}$ end of the distribution ($\nu_{\max} \geq 100\,\mu\mathrm{Hz}$). Since $\nu_{\max}$ is decreasing as a star ascends the RGB (i.e. evolution goes from right to left in Fig. 3.7), the observed morphology seems to be linked to the evolution along the RGB.

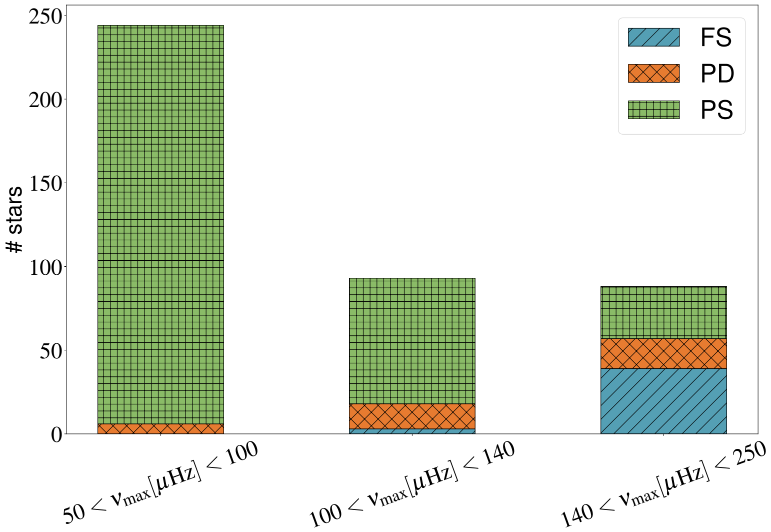

Figure 3.7: Distribution of morphologies in different $\nu_{\max}$-ranges for RGB stars.

To understand why these morphologies dominate at different stages along the RGB, we take a closer look at evolutionary changes that could affect the observed suppression of the mode amplitudes. The main evolutionary change determining the reduced visibility is the evolution of the coupling between the two mode cavities (Stello et al., 2016b). The coupling factor q_l (i.e. how strongly the mode cavities are coupled, see e.g. Hekker and Christensen-Dalsgaard, 2017, for more information) mainly determines the fraction of the total mode energy that can be dissipated in the central regions of the star. A larger q_l (i.e. stronger coupling) allows for a stronger effect of the additional damping on the modes, since a larger fraction of mode energy can be dissipated in the inner regions. The extent of the evanescent zone between the mode cavities determines how strong the coupling between the cavities is (Shibahashi, 1979; Unno et al., 1989; Hekker et al., 2018). As the star ascends the RGB, it is expected that the coupling factor decreases in the observed frequency range (e.g. Dupret et al., 2009). A lower $\nu_{\max}$ (i.e. more evolved on the RGB) can therefore be related to a weaker coupling between the mode cavities allowing less energy to be dissipated. We hence expect more stars in the PS category (i.e. partially suppressed) at lower $\nu_{\max}$ as the coupling is supposedly weaker. This is exactly what we see in the distribution of the stars in the PS category in Fig. 3.7.

We can expect that the stars with the highest ν_{max} (at the start of the RGB) have a rather strong coupling between the mode cavities (see e.g. Mosser et al., 2017b), leading to a large amount of mode energy that can be dissipated. This is also reflected in the observations as the stars undergoing the strongest dissipation, mainly stars of the FS category, have a high ν_{max} (see Fig. 3.4 and e.g. Stello et al., 2016b; Mosser et al., 2017a). We emphasise here that next to q_l, the efficiency of the damping mechanism also plays a role in the amount of energy the modes lose. As even the energy of the dipole mode in the p-mode cavity is dissipated, we can interpret fully suppressed dipole-mode stars as stars with a high coupling factor and an efficient additional damping mechanism acting in their central regions.

We also find stars from the PD and PS categories at high ν_{max}. These early RGB stars are expected to have a relatively strong coupling for RGB stars. From observations, we indeed see a spread in the coupling factors at a given ν_{max} (see e.g. Mosser et al., 2017b). These variations in the coupling factors affect the observed visibility and can explain the observed spread at high ν_{max}.

RGB stars with low ν_{max} have a relatively weak coupling between mode cavities (compared to earlier in their evolution). If the damping mechanism is efficient, we expect that the energy that reaches the central regions of the star is lost completely. On the other hand, if the damping mechanism is less efficient, only a fraction of the total energy in the core is lost. This difference in efficiency would be visible in the power spectrum through the absence or the presence of g-dominated mixed dipole modes (i.e. PD or PS morphology observed in the PDS). We note that the observed dipole-mode frequencies of the stars in the PD category do not show signs of mixed character (i.e. coupling between the mode cavities). Their observed normalised visibility however clearly indicates energy dissipation is occurring in the central regions of the star. This means that the damping is so efficient that the modes in the g-mode cavity cannot couple with the modes in the p-mode cavity. In other words, we do not observe coupling through the presence of mixed modes, while the coupling factor q_l is expected to be non-zero as per the reduced visibilities.

For the CHeB stars, we expect higher coupling strengths than for RGB stars (see e.g. Mosser et al., 2017a). As we do not observe CHeB stars with fully suppressed dipole modes, the additional damping mechanism does not seem to be efficient enough to completely dissipate the energy in the g-mode cavity.

As the coupling factor q_l of a star also decreases with spherical degree l, we expect quadrupole and higher degree modes to be less affected by the damping mechanism. This connection between coupling factor and mode suppression has already been discussed for the observed (Stello et al., 2016b; Mosser et al., 2017a) and predicted (Fuller et al., 2015; Cantiello et al., 2016) normalised visibility.

3.6.5. Difference in mass distributions

The mass distribution of RGB stars appears to peak at lower mass than reported in previous studies (see e.g. Stello et al., 2016a,b; Mosser et al., 2017a). The observed mass distribution is similar to the mass distribution of all *Kepler* red giants. We also note that the observed mass distribution encompasses the same mass range as the stars for which magnetic splittings (i.e. direct measurement of a core-magnetic field, see e.g. Deheuvels, 2024) have been determined. The observed mass distribution is thus in line with the hypothesis of a core-magnetic field as the additional damping mechanism in suppressed dipole-mode stars as proposed by Fuller et al. (2015). Additionally, Bugnet et al. (2021) conclude from their study that low- ($M \lesssim 1.1\mathrm{M}_{\odot}$) and intermediate-mass ($M \gtrsim 1.1\mathrm{M}_{\odot}$) stars are able to develop a significant core-magnetic field. This result indicates that the mass is not a determining factor for the development of a strong core-magnetic field.

3.6.6. Observed distribution of rotational features

The lack of rotational signatures in suppressed dipole-modes can be the result of the amplitude suppression. These stars could however also be very slow rotators (splittings of about 0.1 μHz, see e.g. Gehan et al., 2018) as the angular momentum transport in these stars may be affected by the damping mechanism as well. It has for example been shown that core-magnetic fields can influence the redistribution of angular momentum in a star (Fuller et al., 2019). Alternatively, a merger scenario could explain our observations, as low rotation rates (along with a strong magnetic field) are the expected properties of merger products (see e.g. Schneider et al., 2020; Rui and Fuller, 2021). If we assume further that the merger occurs on the main sequence, we do not expect the asteroseismic properties of the merger product to differ significantly from the properties of a genuine single star with similar mass (Rui and Fuller, 2021). Lastly, the observed lack of rotational features could be due to the inclination at which we observe these stars preventing us from resolving the rotational multiplets. The latter seems highly unlikely, as we expect an isotropic distribution of the inclinations (see e.g. Kuszlewicz et al., 2019).

3.7. Conclusions

We conducted this study to assess the validity of the full dissipation framework for describing the suppressed dipole-mode stars. To this purpose we analysed the power spectra of these stars searching for signs of mixed non-radial modes, compared the observed normalised visibility to the linewidth ratio and to the visibility predicted within the theoretical framework. We found that about 20% of our sample has mode properties completely consistent with the predictions of the full dissipation framework. The dipole-mode properties of the remaining 80% of our sample suggest only partial dissipation as mixed dipole modes are observed. For most of these stars, their quadrupole-mode properties however imply that the full dissipation framework is still valid for modes with a higher spherical degree. Our results thus indicate that the full dissipation framework is needed to explain (part of) the properties of suppressed dipole-mode stars. As it does not encompass all suppressed dipole-mode stars, our results suggest that the additional damping mechanism at play in these stars should allow a combination of partial and full dissipation of the mode energy entering the g-mode cavity. The onset and the effect of the damping mechanism should furthermore depend on the spherical degree.

In summary, our findings are in line with a damping mechanism causing partial to full dissipation of the energy entering the g-mode cavity depending on frequency and spherical degree of the modes as well as the evolutionary stage of the star. These constraints have to be considered for the further development of potential damping mechanism in the partial dissipation framework. Loi and Papaloizou (2017); Loi (2020); Müller et al. (2025) show that the presence of a core magnetic field can lead to an additional source of damping in the partial dissipation framework. We further explore the implications of a core-magnetic field in the partial dissipation framework in detail (see Müller et al., in prep.).

Acknowledgments Original paper acknowledgements. We acknowledge funding from the ERC Consolidator Grant DipolarSound (grant agreement # 101000296).

4

Magnetic shift and mode suppression in non-radial modes of red giants

Authors Quentin Coppée, Jonas Müller and Saskia Hekker

Chapter info This chapter is the last paper I wrote as part of my doctoral studies. At the time of writing, this paper is close to submission. I was the main author of this work and I computed, analysed and interpreted the results. The original idea of this project came from my colaborator Jonas Müller and myself. Jonas Müller computed the stellar models used in this work. Together with Saskia Hekker, they helped me with the interpretation of the results in the form of useful suggestions and comments.

Abstract The effect of a magnetic field in the core on the oscillation modes of red giants can be described in two regimes: the weak- and strong-field regime. The threshold between the two regimes is the so-called critical field strength. In the strong-field regime, we expect the energy of the mode in the g-mode cavity to be dissipated. In the weak-field regime, we expect the mixed-mode frequencies to be shifted to higher frequencies. As the critical field strength decreases with spherical degree, a subset of red giants should have magnetic frequency shifts in their dipole modes, while the g-mode contribution in their quadrupole modes is fully dissipated. In this regard, finding stars with dipole and quadrupole modes in the weak- and strong-field regime is valuable, as these stars are interesting testing grounds to observationally link the presence of a magnetic field (through the dipole modes) with mode suppression (through the quadrupole modes) in red giants.

In this study, we aim to observationally confirm the link between mode-energy dissipation and the presence of a strong magnetic field in the core of the star. To this end, we determined the dipole-mode frequency shifts in the power spectra of eleven stars from the literature known to have significant magnetic shifts and to show negligible rotational effects. We also verified whether the quadrupole-mode properties of these stars (i.e. mode amplitude, mode linewidth) are consistent with predictions in the full dissipation framework. Based on the measured magnetic shift and the observed non-radial modes we estimated the minimal magnetic field strength of the magnetic field in the core of the stars. By comparing these estimated magnetic field strength to the critical field strength of the quadrupole modes,

we assessed the observational confirmation that the observed magnetic field can cause the observed mode suppression in the quadrupole modes.

For eight stars in our sample, our results indicate full dissipation of the g-mode contribution in their quadrupole modes. The magnetic field estimates of these stars are all larger than the quadrupole-mode critical magnetic field. In other words, we expect the quadrupole modes to be in the strong-field regime which is directly confirmed by the quadrupole-mode properties (i.e. full dissipation). We thus found observational evidence that mode suppression is caused by magnetic field in the core of red giants.

The remaining three stars show signs of partial dissipation in the quadrupole modes in the form of quadrupole-mode doublets. These doublets can be interpreted as p-dominated quadrupole modes or as magnetically shifted quadrupole modes. If we consider the first interpretation, only two of the three stars have magnetic field estimates that can explain the partial dissipation observed in the quadrupole modes. If we however consider the second interpretation, the quadrupole-mode properties of all three stars can be explained by the presence of a magnetic field in their core. We note that these quadrupole-mode magnetic shifts, if confirmed theoretically, would be the first observations of this effect in quadrupole modes.

We conclude that the estimates of the magnetic field strength obtained from the dipole-mode magnetic shifts are consistent with the magnetic field strength required to explain the quadrupole-mode visibility for ten of the eleven stars in our sample. The values for the remaining star are also consistent with the presence of a strong magnetic field if the observed quadrupole-mode doublets are magnetically shifted modes. We thus found strong indications that the observed mode-energy dissipation can be linked to the presence of a core-magnetic field. Moreover, we confirm that the combination of dipole and quadrupole-mode properties is a promising prospect to further understand and constrain magnetic fields in red giants.

4.1. Introduction

In Sect. 1.2.3, we introduced the effect of a magnetic field in the core on the oscillation modes of a red giant. We identified two regimes based on the threshold field strength defined as the critical field strength $B_{\mathrm{crit},l}$, which depends on the spherical degree l of the oscillation mode (see Eq. (1.41) and Fuller et al., 2015; Rui and Fuller, 2023). In the weak-field regime ($B < B_{\mathrm{crit},l}$), the non-radial modes should be shifted to higher frequencies (see e.g. Bugnet et al., 2021; Mathis et al., 2021; Li et al., 2022). If the magnetic perturbation is the only effect on the frequencies, we can estimate the strength of the magnetic field from the observed frequency shifts (Deheuvels et al., 2023). Finding signs of these magnetic frequency shifts are strong indications that a magnetic field is present in the core of the star (see e.g. Li et al., 2022, 2023; Deheuvels et al., 2023; Hatt et al., 2024).

In the strong-field regime ($B > B_{\mathrm{crit},l}$), the mode-energy in the g-mode cavity is fully dissipated. This means that the oscillation modes in this regime can be described within the full dissipation framework (see Sect. 3.2).

As the critical field strength decreases with spherical degree, the critical field strength for the dipole modes $B_{\mathrm{crit},1}$ is always larger than that for the quadrupole modes $B_{\mathrm{crit},2}$. There is therefore a magnetic field strength in between $B_{\mathrm{crit},1}$ and $B_{\mathrm{crit},2}$ where the magnetic field would cause full mode-energy dissipation in the g-mode cavity of the quadrupole modes (i.e. strong-field regime) and frequency shifts in the dipole modes (i.e. weak-field regime).

Red giants harbouring a magnetic field with such a field strength would be a interesting testing ground for the magnetic effects on solar-like oscillations. These stars would indicate observationally that a magnetic field in the core of a red giant causes mode-energy dissipation in the g-mode cavity. To this end, we selected the sample of stars from Deheuvels et al. (2023). The power spectra of these stars do not have strong indications of rotation allowing for a straightforward estimation of the magnetic field strength. Furthermore, all these stars have confirmed magnetic shifts in the dipole modes Deheuvels et al. (2023) and two of the stars (KIC 3109742 and KIC 6975038, a step-suppression star, see Sect. 3.4.1) even show signs of energy dissipation in the dipole modes. These stars are therefore good candidates to asses the observational link between mode-energy dissipation and the presence of a magnetic field in the stellar core.

We outline our methodology to obtain the global asteroseismic parameters and individual mode properties (frequencies, linewidths and amplitudes) of the stars in Sect. 4.2. We describe how we obtained the magnetic shift and consequently the field strength estimate in Sect. 4.3. In Sect. 4.4, we discuss the quadrupole-mode properties of the stars in our sample and whether these properties are consistent with the full dissipation of the energy in the g-mode cavity. In Sect. 4.7, we compare the magnetic-field estimates to the dipole- and quadrupole-mode critical magnetic fields. We dedicate Sect. 4.8 to the conclusions of our study.

4.2. Frequency analysis

We used our peakbagging code TACO (Tools for the Automated Characterisation of Oscillations, Hekker et al., in prep.) to analyse the light curves of our stars. In the following section, we outline how we determined the frequency of maximal oscillation power $\nu_{\rm max}$ and the large frequency separation $\Delta\nu$ for each star as well as the mode frequency ν_{nl}, the mode linewidth Γ_{nl}, and the mode amplitude A_{nl} of the individual modes detected in the power spectra of the stars in our sample. These steps are similar to the steps discussed in Sect. 3.3.

Firstly, we fitted our background model (Eq. (1.20)) together with an power envelope to the power density spectrum of the star using the following expression (see Sect. 1.2.2 for more information):

$$P_{\rm B}\left(\nu\right) = P_{\rm n} + \eta^2(\nu)\left(P_{\rm bgr}(\nu) + P_{\rm g}\exp\left[-\frac{(\nu-\nu_{\rm max})^2}{2{\sigma_{\rm env}}^2}\right]\right). \tag{4.1}$$

Secondly, we detected resolved and unresolved modes in the power spectrum, normalised by the background model without the power envelope, using the peak detection method developed by García Saravia Ortiz de Montellano et al. (2018). Each individual resolved mode was fitted with a Lorentzian function

$$P_{nl}\left(\nu\right) = \frac{2A_{nl}^2}{\pi\Gamma_{nl}}\frac{1}{1+\left(\frac{2(\nu-\nu_{nl})}{\Gamma_{nl}}\right)^2}, \tag{4.2}$$

with ν_{nl}, A_{nl} and Γ_{nl} the central frequency, mode amplitude and mode linewidth (i.e the full-width at half maximum of the peak). Each unresolved mode was fitted with squared sinc function

$$P_{nl}\left(\nu\right) = \frac{A_{nl}^2}{\delta\nu}\,\mathrm{sinc}^2\left(\pi\frac{\nu-\nu_{nl}}{\delta\nu}\right), \tag{4.3}$$

with $\delta\nu$, the frequency resolution of the power spectrum. Using a Maximum Likelihood Estimation, we optimised the fit and estimated lower limits of the uncertainties for the parameters of every peak from the Hessian matrix.

We lastly performed the mode identification of the detected modes using the Universal Pattern (UP, Mosser et al., 2011b) as a guide starting from the central radial order. The mode identification is focussed on the radial, quadrupole and octupole modes, as the remaining modes are dipole modes. We eventually determined $\Delta\nu$ (large frequency separation between successive radial modes) from a linear fit through the identified radial modes.

Table 4.1: Fitted parameters for the stars in our sample. Uncertainties are set by the 25th and 75th percentile of the posterior distributions of the MCMC approach.

	$\Delta\Pi_1$	ε_g	$\delta\nu_{01}$	$\delta\nu_{\mathrm{mag,eff}}$
KIC	[s]		[μHz]	[μHz]
6182668	$83.21^{+2.51}_{-1.35}$	$0.08^{+0.26}_{-1.00}$	$0.03^{+0.23}_{-0.72}$	$5.05^{+0.51}_{-0.44}$
9474201	$82.02^{+0.20}_{-0.37}$	$-0.15^{+0.33}_{-0.45}$	$0.5^{+0.06}_{-0.04}$	$4.67^{+0.13}_{-0.21}$
6842204	$84.56^{+16.08}_{-9.87}$	$0.41^{+0.57}_{-0.65}$	$-0.11^{+0.54}_{-0.58}$	$1.22^{+3.46}_{-1.22}$
8560280	$78.59^{+1.32}_{-2.18}$	$-0.2^{+0.24}_{-0.68}$	$-0.01^{+0.10}_{-0.25}$	$2.38^{+0.48}_{-0.34}$
8689270	$79.94^{+0.24}_{-8.18}$	$0.21^{+0.06}_{-0.41}$	$0.11^{+1.23}_{-0.01}$	$0.08^{+0.20}_{-0.08}$
3216736	$77.78^{+0.13}_{-5.64}$	$-0.25^{+0.87}_{-0.50}$	$-0.13^{+0.04}_{-0.15}$	$2.66^{+2.28}_{-0.08}$
5180345	$77.23^{+0.13}_{-13.23}$	$0.31^{+0.49}_{-0.41}$	$-0.04^{+0.05}_{-0.54}$	$2.11^{+1.55}_{-0.07}$
6975038	$68.51^{+6.35}_{-2.55}$	$0.27^{+0.88}_{-0.95}$	$0.14^{+0.54}_{-0.28}$	$3.96^{+0.86}_{-0.38}$
3109742	$75.05^{+0.61}_{-6.09}$	$-0.25^{+0.53}_{-0.32}$	$-0.07^{+0.07}_{-0.55}$	$1.59^{+2.14}_{-0.29}$
6614684	$73.41^{+1.73}_{-6.60}$	$-0.2^{+0.99}_{-0.38}$	$-0.20^{+0.18}_{-0.31}$	$1.42^{+1.98}_{-0.08}$
7728945	$72.85^{+0.95}_{-7.90}$	$0.03^{+0.42}_{-0.37}$	$-0.19^{+0.30}_{-0.36}$	$0.99^{+1.92}_{-0.46}$

4.3. Magnetic shift determination

In this section, we describe how we determined the magnetic shift from the observed dipole modes by fitting the perturbed asymptotic mixed-mode frequencies (Eq. 1.40) to the observed frequencies using an Markov chain Monte Carlo (MCMC) approach, similar to Deheuvels et al. (2023). We recall Eq. (1.40) obtained from the approach developed by Mathis et al. (2021); Bugnet (2022):

$$\nu_{\mathrm{obs}} = \nu + \frac{1}{2}\left(\frac{\nu_{\mathrm{max}}}{\nu}\right)^3 \zeta(\nu)\delta\nu_{\mathrm{mag,eff}}\,, \tag{4.4}$$

with the effective magnetic shift $\delta\nu_{\mathrm{mag,eff}}$ defined as

$$\delta\nu_{\mathrm{mag,eff}} \equiv (|m|+1)\,\delta\nu_{\mathrm{mag}}. \tag{4.5}$$

Here m is the azimuthal order of the oscillation mode and $\delta\nu_{\rm mag}$ is the intrinsic magnetic shift measured at $\nu_{\rm max}$.

The asymptotic frequencies ν of the mixed dipole modes depend on the mode coupling factor q_1, the period spacing $\Delta\Pi_1$, the gravitational offset ε_g and the small frequency separation for the dipole modes $\delta\nu_{01}$ (see Eq. (1.17) and e.g. Hekker and Christensen-Dalsgaard, 2017). To reduce the number of fitting parameters, we estimated the coupling factors q_1 following the method developed by Vrard et al. (2016) and kept these fixed. From the method of Vrard et al. (2016), we simultaneously obtained an estimate for $\Delta\Pi_1$ which was used as initial value for this parameter. We estimated the initial value of $\delta\nu_{01}$ using the scaling relation as a function of $\Delta\nu$ from Mosser et al. (2018), while the initial value of ε_g was set to 0.25 (see Takata, 2016; Mosser et al., 2018).

We chose uniform priors for the fitting parameters $\Delta\Pi_1$, $\delta\nu_{01}$, and $\delta\nu_{\rm mag,eff}$. For ε_g we set up a Gaussian prior with a mean of 0.28 and a spread of 0.12 (see Deheuvels et al., 2023, and references therein). The best-fit values for all four fitting parameters are listed in Table 4.1. We set the 25th and 75th percentile of the posterior distributions of the MCMC approach as the uncertainties on the best-fit values.

4.4. Magnetic field-strength constraints from quadrupole-mode properties

We can assess the full dissipation of the g-mode character in quadrupole modes by comparing the observed relation between the average normalised visibility v_2 and the average linewidth ratio Γ_0/Γ_2 to the prediction in the full dissipation framework (see e.g. Mosser et al., 2017a, and Chapter 3 of this thesis). We recall that the predicted relation is

$$v_2 = \frac{\Gamma_0}{\Gamma_2}. \tag{4.6}$$

We computed v_2 and Γ_0/Γ_2 in a similar fashion as in Chapter 3 of this thesis, namely

$$v_2 = \sum_{k=n_{\rm max}-2}^{n_{\rm max}+2} w_k \frac{A_{k2}^2}{A_{k0}^2 \mathcal{G}_2} \tag{4.7}$$

and

$$\frac{\Gamma_0}{\Gamma_2} = \sum_{k=n_{\rm max}-2}^{n_{\rm max}+2} w_k \frac{\Gamma_{k0}}{\Gamma_{k2}}\ . \tag{4.8}$$

Here A_{k2} (Γ_{k2}) is the amplitude (linewidth) of the quadrupole mode in acoustic radial order k, A_{k0} (Γ_{k0}) the amplitude (linewidth) of the radial mode of the same acoustic radial order, $w_k = A_{k0}^2/A_0^2$ the fractional contribution of each radial mode to the total radial-mode power A_0^2 (i.e. the sum of the squared radial-mode amplitudes of the five most central acoustic radial orders), $n_{\rm max}$ the acoustic radial order closest to $\nu_{\rm max}$ and $\mathcal{G}_2$ a geometrical factor considering the effects of spherical degree, limb-darkening and the instrumentation (see e.g. Ballot et al., 2011). For this study, we adopted $\mathcal{G}_2 \approx 0.688$ (see e.g. Mosser et al., 2012; Stello et al., 2016b).

In Fig. 4.1, we show the linewidth ratio Γ_0/Γ_2 as a function of the normalised visibility v_2. In a few stars (triangular markers in Fig. 4.1), we find indications of two quadrupole modes per radial order, suggesting that the g-mode contribution to the quadrupole modes

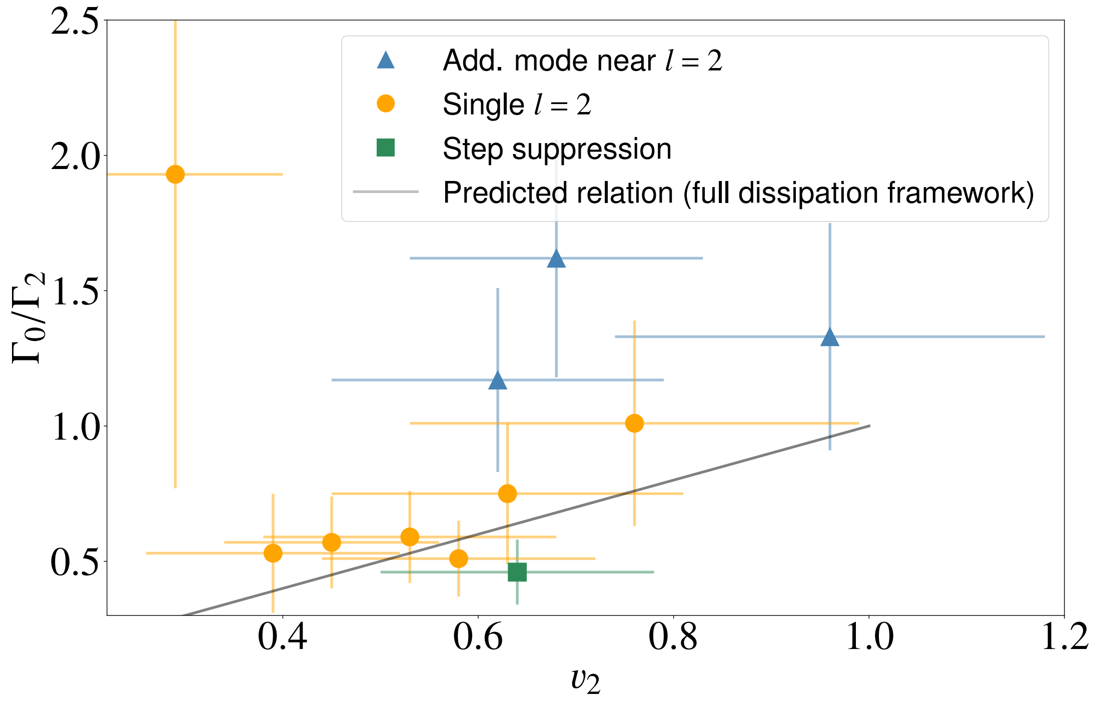

Figure 4.1: Linewidth ratio as a function of the normalised visibility for the quadrupole modes. The markers indicates the number of detected quadrupole modes in an acoustic radial order (dots for quadrupole-mode singlets and triangles for quadrupole mode doublets). The step-suppression star (KIC 6975038) is highlighted with a square marker. The grey solid line shows the predicted one-to-one relation between the linewidth ratio and the normalised visibility in case of full dissipation of the g-mode character.

is not completely dissipated. This is confirmed by the values of their measured visibility and linewidth ratio, as these values are not in line with the predicted relation assuming full dissipation of the g-mode contribution (solid line in Fig. 4.1). One of these stars has an observed visibility close to one, suggesting that the modes of this star are not strongly affected, if at all, by an additional source of damping.

Except for one star at low visibility, we also see in Fig. 4.1 that the stars with one quadrupole mode per acoustic radial order (circles and square markers) have quadrupole-mode properties consistent with the prediction in the case of full dissipation of the g-mode character. The star at low visibility has only three observed acoustic radial orders with unexpectedly small and narrow quadrupole modes. The low-visibility of the quadrupole modes is however a strong sign of mode-energy dissipation.

4.5. Azimuthal order of observed non-radial modes

As mentioned in Sect. 1.2.3.1 and repeated in Sect. 4.3, the intrinsic magnetic shift $\delta\nu_{\mathrm{mag}}$, needed to estimate the magnetic field strength, can be obtained from the effective magnetic shift $\delta\nu_{\mathrm{mag,eff}}$ if the azimuthal order m of the observed modes is known, $\delta\nu_{\mathrm{mag}} = \delta\nu_{\mathrm{mag,eff}} / (|m| + 1)$. In this section, we deduce the azimuthal order m of the dipole modes with the help of the quadrupole modes.

In general, we expect dipole triplets and quadrupole quintuplets when we consider linear perturbations of rotational or magnetic nature (see e.g. Goupil et al., 2013; Bugnet et al., 2021). Since we observe dipole-mode singlets together with quadrupole-mode singlets or doublets, we also have to consider the effect of the inclination angle i on the mode amplitudes (Gizon and Solanki, 2003). The mode amplitude of an oscillation mode of spherical degree l and azimuthal order m is reduced by a factor $\mathcal{E}_{lm}(i)$ (see Fig. 4.2 and Gizon and Solanki, 2003) defined as

$$\mathcal{E}_{lm}(i) = \frac{(l-|m|)!}{(l+|m|)!} P_l^{|m|}(\cos i)^2, \tag{4.9}$$

with $P_l^{|m|}$ the associated Legendre functions of spherical degree l and azimuthal order $|m|$.

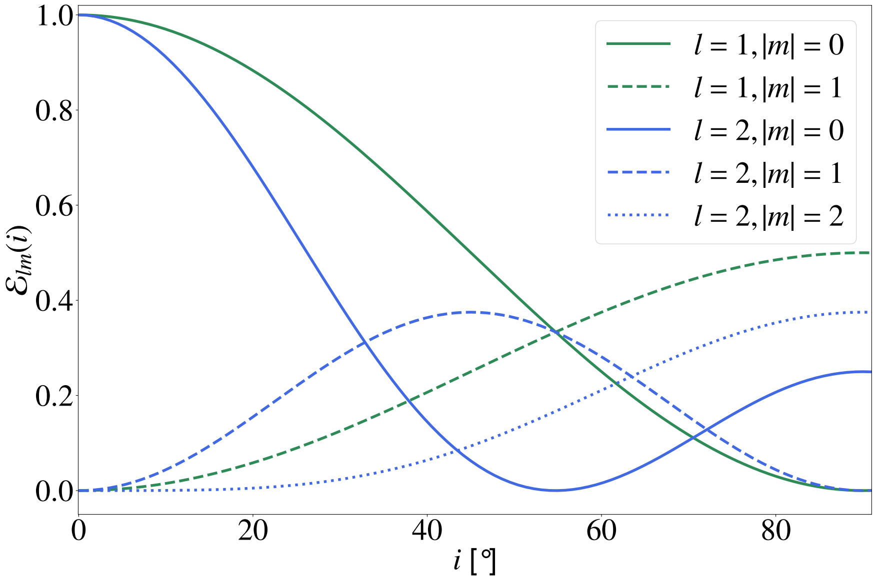

Figure 4.2: Factor $\mathcal{E}_{lm}$ for dipole (green) and quadrupole (blue) modes as a function of the inclination angle i. The azimuthal order $|m|$ of the mode is indicated by the linestyle.

If the effect of rotation is negligible and we consider magnetic perturbation (as expected for the stars in our sample), we detect dipole-mode singlets at an inclination angle close to 0° or 90° (see Fig. 4.2). In the first case ($i \simeq 0°$) we expect to observe a quadrupole-mode singlet while in the latter ($i \simeq 90°$) we would detect a quadrupole doublet. We can therefore deduce that the 8 stars with dipole- and quadrupole-mode singlets are seen pole-on ($i \simeq 0°$). From Fig. 4.2, we deduce that the azimuthal order of the dipole and quadrupole modes of stars with dipole- and quadrupole-mode singlets is 0.

If we assume that the quadrupole doublets observed in the three stars are of magnetic nature, we can conclude that these stars are seen equator-on ($i \simeq 90°$). We deduce from Fig. 4.2 that $|m| = 1$ for the observed dipole-mode singlets, while the quadrupole modes have azimuthal orders $|m| = 0$ or $|m| = 2$. We however also have to consider that the quadrupole-mode doublets in these three stars could be two p-dominated quadrupole modes resulting from the mode coupling between the two mode cavities. In this case, both modes have the same azimuthal order. From this result and the fact that we observe dipole-mode singlets, we conclude that in this assumption the three remaining stars are seen pole-on and furthermore that $|m| = 0$ for the observed dipole and quadrupole modes.

Up until now we neglected the effect of rotation on the observed oscillation modes. We can confirm this assumption based on the observed non-radial modes. If rotation would affect the modes, we would only expect to observe dipole-mode singlets at an inclination angle i close to 0°. This is indeed the only configuration where we observe dipole singlets (i.e. $m = 0$ or zonal dipole mode, see full green curve in Fig. 4.2). At these low inclination angles only the zonal ($m = 0$) quadrupole modes should be visible (full blue curve in Fig. 4.2). The zonal dipole and quadrupole modes are however unaffected by the rotational perturbation (see e.g. Aerts et al., 2010). As we do observe frequency shifts, we conclude that rotation alone cannot account for the observed dipole and quadrupole modes.

We also assumed that both modes in the quadrupole-mode doublets are indeed quadrupole modes. If one of these modes was not of quadrupolar nature, we would expect that they are of dipolar nature with a strongly g-dominated mode character based on the observed frequency patterns (see e.g. the behaviour of the ζ-function in Hekker and Christensen-Dalsgaard, 2017). These modes are typically unresolved and would have narrow widths of the order of the frequency resolution of the power spectrum (see Sect. 1.2.2.2). The observed additional modes have observed linewidths of the same order as the radial and quadrupole modes in the neighbouring acoustic radial orders. These linewidths suggest that the modes most likely have a p-dominated character. As the observed dipole-mode frequency patterns do not seem to agree with the frequencies of these additional modes, we concluded that the additional modes are most likely quadrupole modes.

4.6. Magnetic field estimation

Following the discussion in Sect. 4.5, eight stars have dipole modes with azimuthal order $|m| = 0$. The intrinsic magnetic shift for these stars is equal to the measured effective magnetic shift ($\delta\nu_{\mathrm{mag}} = \delta\nu_{\mathrm{mag,eff}}/\,(|0| + 1) = \delta\nu_{\mathrm{mag,eff}}$). For the remaining three stars, we have two valid interpretations for which the azimuthal order of the observed dipole modes is either 0 or 1. In the latter case, the intrinsic magnetic shift is equal to half the measured effective magnetic shift, $\delta\nu_{\mathrm{mag}} = \delta\nu_{\mathrm{mag,eff}}/\,(|1| + 1) = \delta\nu_{\mathrm{mag,eff}}/2$.

We estimated the minimal magnetic field strength B of the field in our stars by computing (see Li et al., 2022; Deheuvels et al., 2023)

$$B = \frac{32\mu_0\pi^5}{3}\frac{\delta\nu_{\mathrm{mag}}\nu_{\mathrm{max}}^3}{\mathcal{I}} \tag{4.10}$$

with μ_0 the magnetic permeability in vacuum and $\mathcal{I}$ defined as

$$\mathcal{I} = \frac{\int_G \left(\frac{N}{r}\right)^3 \frac{dr}{\rho}}{\int_G \left(\frac{N}{r}\right) dr}. \tag{4.11}$$

Here N is the buoyancy frequency (Eq. (1.6)), ρ the mass density, r the radial coordinate, and the integrals are taken over the g-mode cavity.

To calculate the factor $\mathcal{I}$, we require knowledge of the inner structure of the stars (i.e. radial profiles of the buoyancy frequency N and the density ρ). We therefore computed three evolutionary tracks (see Müller et al., in prep.) with varying stellar mass ($M_* = 1$, 1.25 and 1.5 $M_\odot$) and solar metallicity ($Z_{\mathrm{init}} = 0.02$) using version r23.05.1 of the publicly available stellar evolution code MESA (Modules for Experiments in Stellar Evolution Paxton et al., 2011, 2013, 2015, 2018, 2019; Jermyn et al., 2023). For each star we used the radial profiles of N and ρ of the selected model for which mass and $\nu_{\max}$ were the closest to the observed mass from Yu et al. (2018) and our estimate of $\nu_{\max}$.

The estimates of the magnetic field strength from Eq. 4.10 are shown in Fig. 4.3 and listed in Table 4.2. We note that the use of stellar models and the assumptions used to derive Eq. 4.10 (see Li et al., 2022) renders the determination of the uncertainty on the magnetic field strength estimate difficult. We estimated the uncertainty reported in this study through error propagation of the uncertainty on $\nu_{\max}$ and $\delta\nu_{\mathrm{mag}}$ (see Tables 4.1 and 4.2).

For the three stars with partial dissipation in the quadrupole modes, we only listed the magnetic field estimate in the case that the quadrupole-mode doublets are two p-dominated modes (i.e. $m = 0$ for the dipole modes). We also computed the magnetic field estimates in the case the doublets are caused by magnetic shifts (open triangles in Fig. 4.3).

Table 4.2: Global asteroseismic parameters and magnetic field strength estimates for the stars in our sample.

KIC	$\nu_{\max}$ [μHz]	$\Delta\nu$ [μHz]	M ^{a} [$\mathrm{M}_{\odot}$]	B_* [kG]
6182668	220.53 ± 11.03	16.42 ± 0.82	1.24 ± 0.09	653^{+117}_{-111}
9474201	201.24 ± 10.06	15.02 ± 0.75	1.53 ± 0.09	486^{+74}_{-76}
6842204	178.60 ± 8.93	14.07 ± 0.70	1.26 ± 0.06	230^{+124}_{-116}
8560280	164.60 ± 8.23	13.53 ± 0.68	1.11 ± 0.06	308^{+39}_{-32}
8689270	163.15 ± 8.16	13.36 ± 0.67	1.14 ± 0.05	57^{+73}_{-29}
3216736	148.91 ± 7.45	12.48 ± 0.62	1.23 ± 0.08	241^{+210}_{-37}
5180345	139.01 ± 6.95	11.89 ± 0.59	1.17 ± 0.07	188^{+141}_{-29}
6975038	121.19 ± 6.06	10.54 ± 0.53	1.29 ± 0.08	194^{+51}_{-35}
3109742	102.01 ± 5.10	9.17 ± 0.46	1.32 ± 0.09	88^{+119}_{-21}
6614684	91.12 ± 4.56	8.15 ± 0.41	1.56 ± 0.10	61^{+86}_{-10}
7728945	90.82 ± 4.54	8.26 ± 0.41	1.51 ± 0.09	51^{+99}_{-25}

[a] Masses from Yu et al. (2018).

4.7. Comparison field strength and magnetic field regimes

In this section, we assess if the observed full or partial dissipation of the g-mode character observed in the quadrupole modes of the stars in our sample can be explained by the magnetic field in the core causind dipole-mode frequency shifts. To this end, we can compare the estimated magnetic field strength B to the critical magnetic field for the quadrupole modes $B_{\mathrm{crit},2}$. In the case of full or dissipation of the g-mode character, we expect respectively that $B > B_{\mathrm{crit},2}$ (strong-field regime) and $B < B_{\mathrm{crit},2}$ (weak-field regime). For this study, we defined the critical magnetic field for modes of degree l at the radial coordinate r_H, the location

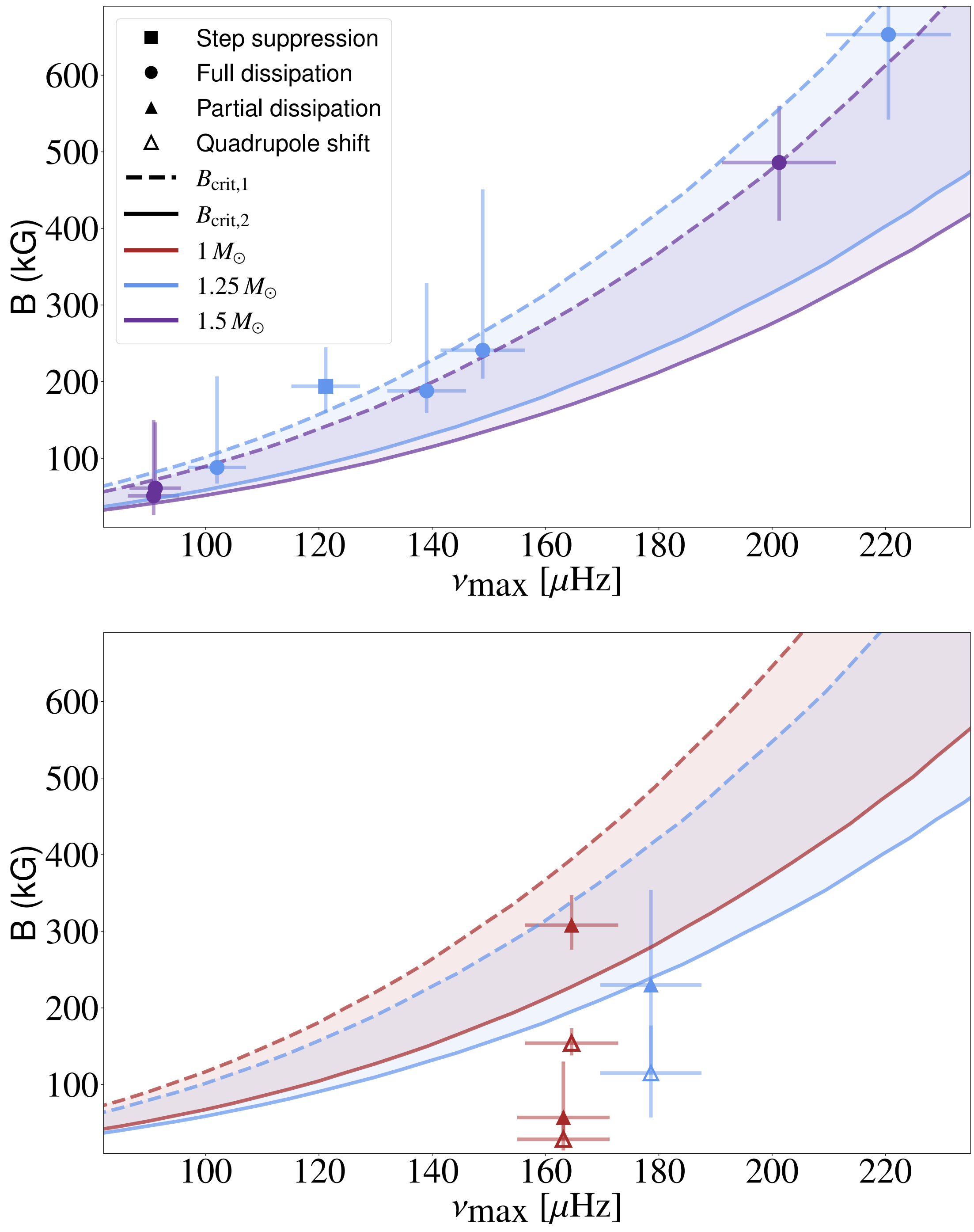

Figure 4.3: Magnetic field estimated from the observed magnetic shifts in the dipole modes as a function of ν_{max} for stars with masses close to 1 (red), 1.25 (blue) and 1.5 $M_\odot$ (purple). The critical magnetic field strength for dipole and quadrupole modes are indicated with a dashed and full curve respectively, while the markers distinguish the stars with quadrupole singlets (dots and squares, top panel) or doublets (triangle, bottom panel). The star KIC 6975038 (square) shows clear signs of mode suppression in the dipole modes. We highlighted the region between the two critical magnetic fields in each panel.

of the hydrogen-burning shell, (Fuller et al., 2015)

$$B_{\mathrm{crit}} = 2\pi^2 \sqrt{\mu_0 \rho} \frac{\nu_{\mathrm{max}}^2}{\sqrt{l(l+1)}N} r_H. \tag{4.12}$$

In Fig. 4.3, we plot the magnetic field strength estimates as well as the critical magnetic field for the dipole and quadrupole modes, colour-coded by mass. We firstly remark that the star KIC 6975038 (square in top panel of Fig. 4.3) is the only star with an estimated magnetic field larger than the critical magnetic field of the dipole modes (dashed lines in Fig. 4.3). If the core-magnetic field would cause the additional damping and the corresponding dissipation of the g-mode cavity, we would expect that not only the quadrupole but also the dipole modes are affected. This is confirmed observationally, as the star is known to exhibit dipole-mode suppression at lower frequencies in its power spectrum (see Step-suppression star in Fig. 3.1 in Chapter 3). We note that the magnetic-shift determination was performed using only the dipole modes at higher frequencies ($\nu > 130\mu$Hz).

For the stars with full dissipation in the quadrupole modes (dots in top panel of Fig. 4.3), we expect that their magnetic field is in between the dipole-mode and quadrupole-mode critical field strength, assuming that the mode-energy dissipation is caused by the magnetic field. This is exactly the range in which we find their magnetic field estimates in Fig. 4.3 (see highlighted regions).

The magnetic field strength estimates for the three stars with partial dissipation in the quadrupole modes are shown in the bottom panel of Fig. 4.3 in the case that the doublets are actual p-dominated without magnetic shifts (full triangles). Two of these estimates are consistent with the expected field strength regime for these stars (weak field regime, $B < B_{\mathrm{crit},2}$). If we however consider that these quadrupole-mode doublets are the results of magnetic shifts, we found that the magnetic field estimates of all three stars are consistent with the weak-field regime as expected from the partially dissipated g-mode character in the quadrupole modes.

We found that ten of the eleven stars (or all stars if we consider magnetic shifts in the quadrupole modes) have magnetic field estimates consistent with the mode-energy dissipation in the quadrupole modes. In other words, the observed mode-energy dissipation and frequency shifts can be explained by a magnetic field with the same field strength located in the core of the star.

4.8. Conclusions

In this study, we analysed a sample of stars with known magnetic shifts and lack of rotational effects (Deheuvels et al., 2023). By determining the intrinsic magnetic shift causing the observed frequency shifts in the dipole modes, we were able to estimate the magnetic field strength of the fields in the core of the stars. As the observed shifts can only be explained through a magnetic shift, we can assume that magnetic fields are indeed present in the core of the stars in our sample. From the quadrupole-mode properties of the stars, we were able to distinguish two subsets: eight stars show sign of full dissipation of the g-mode character in the quadrupole modes, while the remaining three show signs of partial dissipation. From the comparison of the magnetic field estimates for the stars in the two subsets to the critical field strength (threshold field strength between full and partial dissipation due to the magnetic field, see e.g. Fuller et al., 2015) of the quadrupole modes, we concluded that these estimates are in line with the observed full and partial dissipation of the mode-energy in the g-mode cavity of the quadrupole modes. We furthermore conclude that for the first time, two distinct magnetic effects in the dipole and quadrupole modes be explained by a magnetic field with the same field strength located in the core of the star. Further observational results like the results presented in this study are needed to strengthen the observational link between the presence of a core-magnetic field and mode suppression. We expect that new candidates can be found among the stars of the PS category (see Chapter 3).

We report three potential cases of quadrupole-mode doublets that could be due to magnetic shifts. A thorough theoretical analysis based on the work of Mathis et al. (2021); Bugnet et al. (2021); Bugnet (2022) could confirm if these doublets are of magnetic nature. If this can be confirmed, it would be the first observational evidence for quadrupole-mode magnetic shifts.

We also confirm that the theoretical developments of Mathis et al. (2021); Bugnet (2022) can be used to describe magnetic shift as well as the approach developed by Li et al. (2022); Deheuvels et al. (2023). As suggested by Bugnet et al. (2024), the quadrupole modes contain key informations about the magnetic field and a thorough analysis of their properties can be beneficial for our understanding of core-magnetism.

Acknowledgments We acknowledge funding from the ERC Consolidator Grant DipolarSound (grant agreement # 101000296).

5

Conclusions and outlook

In this chapter, I summarise the main results and conclusions of the research presented in Chapters 2, 3, and 4. I furthermore discuss interesting remaining open questions that still have to be addressed.

The main aim of this thesis is to obtain observational constraints on the mechanism causing the mode suppression in the non-radial modes of suppressed dipole-mode stars. A subsequent aim is to confirm or disprove that the observed mode suppression is the result of a magnetic field in the core of the star using the new observational constraints. In this regard, we used the predictions of the full and partial dissipation framework developed for magnetic fields in the core of red giants by Fuller et al. (2015); Cantiello et al. (2016); Rui and Fuller (2023) and Loi and Papaloizou (2017); Loi (2020); Müller et al. (2025) respectively.

We confirmed in Chapter 2 that the observed mode suppression in suppressed dipole-mode stars is caused by an additional source of damping in the core of the star. In summary, we found that the distributions of the radial-mode damping rates (i.e. the linewidth) and the radial-mode energy (i.e. the squared amplitude) are similar for stars with low and typical dipole-mode visibility. Since the mode energy is set by the balance of mode damping and mode excitation, we deduced that the mode excitation for the radial modes is unaffected by the mechanism responsible for the low mode amplitudes. Assuming that the excitation is the same for all modes, independent of spherical degree, the low visibility is not caused by a lack of excitation but merely by additional damping. As the radial-mode damping is also unaffected by the additional damping mechanism, we concluded that this additional source of damping is most likely localised in the central regions of the star. Based on our observations, we thus expect the presence of an additional source of damping in the central regions of red giants with low dipole-mode visibility. This is also in line with the full and partial dissipation frameworks, since the main assumption of these frameworks is that an additional damping process dissipates the mode energy in the g-mode cavity of red giants.

As the partial dissipation framework has to be confirmed to hold under more general assumptions (see e.g Loi and Papaloizou, 2018, considering rotational and magnetic effects simultaneously), we focused on one of the limits of the framework, the full dissipation framework (see e.g. Fuller et al., 2015), for which several predictions can be tested (see Chapter 3). With our results, we confirmed just as Mosser et al. (2017a) that the normalised visibility is not enough to characterise a suppressed dipole-mode star. The morphology, or in other words the number of detected dipole modes per radial order, must also be taken into account. We conclude from our study that about 20% of the stars in our sample can be explained in the full dissipation framework, indicating that the partial dissipation framework is indeed needed and more importantly that the full dissipation limit has to be taken into account. For the remaining 80% we find that the dipole-mode properties are not in line with the predictions of the framework. However, for about 75% of them, their quadrupole-mode properties suggest that the full dissipation framework can still be valid, at least for higher spherical degree. This indicates that the additional damping mechanism has a threshold and an efficiency that both depend on spherical degree. These results are consistent with the *magnetic greenhouse effect* proposed by Fuller et al. (2015).

In Chapter 4 we showed that for ten out of eleven red giants with clear magnetic shifts, the mode properties of dipole and quadrupole modes can be explained by a magnetic field with the same field strength located in the core of the stars. We conclude from this study that the observed mode-energy dissipation is consistent with the presence of a strong magnetic field in the core of the star. After the step-suppression star discussed by Deheuvels et al. (2023), these are the first stars with strong observational indications of mode-energy dissipation due to a magnetic field in the core of the star. Our sample is small and should be extended with stars from the PS category (partially suppressed dipole-mode stars, see Chapter 3). We also confirmed observationally that the combination of dipole and quadrupole modes can be important to constrain the (configuration of) the magnetic field (see also Bugnet et al., 2024).

In Chapter 4 we also mentioned the possibility that the observed quadrupole-mode doublets in the stars with quadrupole-mode partial dissipation could be interpreted as magnetically shifted quadrupole modes. If this can be theoretically confirmed, it would be the first observational case of quadrupole magnetic shifts. A more in-depth analysis of these stars and of the theoretical predictions of Mathis et al. (2021) are required to understand these quadrupole-mode doublets.

In Chapter 3 and 4 we found several observational constraints that can be used in the further developments of the partial dissipation framework (see e.g. Müller et al., in prep.). It would be interesting to compare the future predictions of this framework to stars showing a combination of magnetic and rotational frequency shifts. In general, finding more stars with magnetic shifts would be helpful to confirm the link between mode suppression and core magnetic fields.

In our study, we also found that the suppressed dipole-mode stars show less clear signs of rotation than expected. This observation can also be interpreted as a sign of the presence of a core-magnetic field. Fuller et al. (2019) have indeed shown that core-magnetic fields can influence the angular momentum redistribution. Alternatively, we expect merger products to have low rotation rates (along with a strong magnetic field) (see e.g. Schneider et al., 2020; Rui and Fuller, 2021). Rui and Fuller (2021) showed that if the merger happens on the main sequence, the asteroseismic properties of the merger product are very similar to that of a genuine single star. It would be valuable to simulate such a low-mass merger on the main sequence and follow its evolution until the CHeB phase. This could further confirm if strong magnetic fields can be formed. More importantly, it would also explain why we would only observe strong magnetic fields in this small fraction of the whole set of red giants observed by *Kepler* (see e.g. Yu et al., 2018). From Bugnet et al. (2021), we know that almost all low-mass stars are able to develop a significant core-magnetic field, but it is still unknown how magnetic fields strong enough to cause mode-energy dissipation can form.

Overall, in this thesis, I investigated the suppressed dipole-mode stars and found important observational constraints that should be considered in the further developments of the partial dissipation framework. I furthermore confirmed observationally that a magnetic field in the core can indeed explain the mode-energy dissipation in oscillation modes of red giants. The future of magneto-asteroseismology of red giants seems very promising.

A

Appendices for Chapter 2: The radial modes of stars with suppressed dipole modes

A.1. Comparison of ν_{max} and $\Delta\nu$ with literature values

In this section we compare the values of ν_{max} and $\Delta\nu$ obtained with our code to the values found in the literature. We find agreement between our results and the data from Vrard et al. (2018) and Kallinger (2019) for the stars we have in common with their samples (about 70% of our samples). We show in Fig. A.1 and A.2 as well as in Fig. A.3 and A.4 the difference in ν_{max} and $\Delta\nu$ between our results for our low-visibility sample, S_c and S_p and the data published by respectively Kallinger (2019) and Vrard et al. (2018) as a function of their uncertainties. We defined the uncertainty on the difference in ν_{max} as one $\Delta\nu$ and on the difference in $\Delta\nu$ as the combination of the individual uncertainties in quadrature (similar to e.g. in Eq. 2.5). We find that our values for ν_{max} are within 1 Δ_ν and Δ_ν within 3σ of the given uncertainties. The few outliers in the differences of $\Delta\nu$ are caused by a different number of detected radial modes.

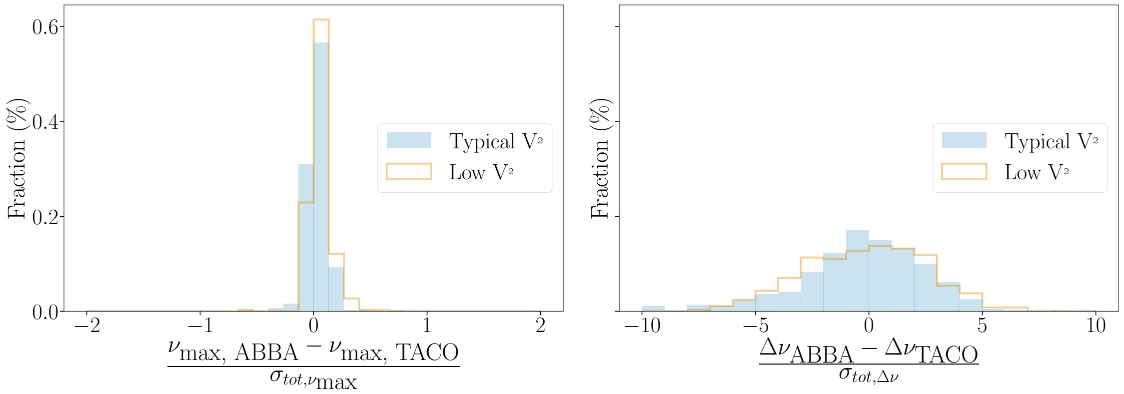

Figure A.1: Difference between the ν_{max} (left) and $\Delta\nu$ (right) derived in this work and the results of ABBA (Kallinger, 2019) expressed in σ for stars in the low-visibility sample (orange) and S_c (blue).

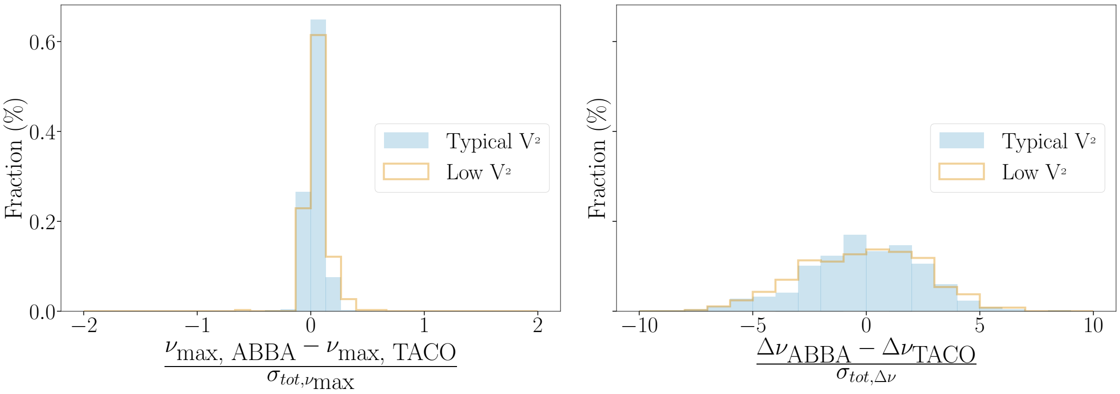

Figure A.2: Same as in Fig. A.1, but now for S_p (blue).

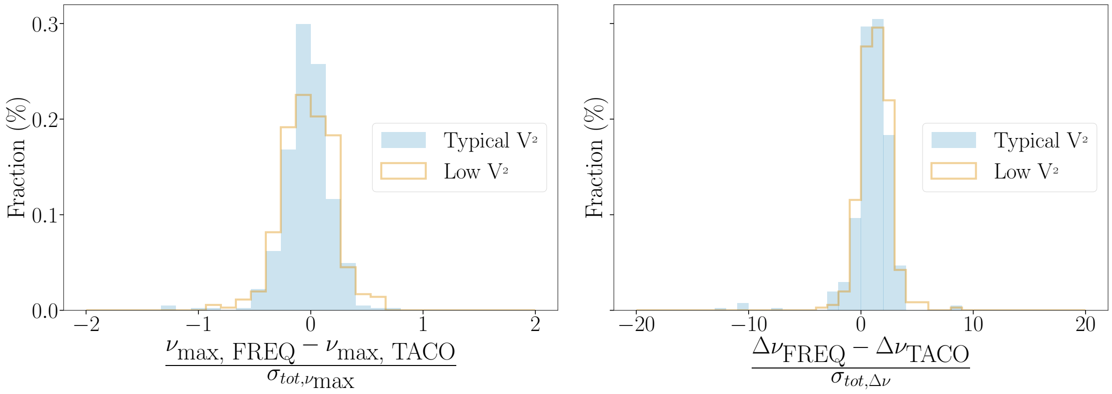

Figure A.3: Same as in Fig. A.1, but now for a comparison with the FREQ results (Vrard et al., 2018).

A.2. Comparison of individual linewidths, amplitudes, and heights with literature values

In this section we compare the values of the linewidths, amplitudes and heights obtained with our code to the values found in the literature. Kallinger (2019) and Vrard et al. (2018) do not report values for the heights of the detected peaks. We therefore computed the heights using Eq. 2.8 with the reported values for the linewidths and amplitudes. We find that our results are in agreement with the values from Kallinger (2019, see our Figs. A.5 and A.6). By comparing our results of our low-visibility sample and our control samples with the values of Vrard et al. (2018, see our Figs. A.7 and A.8), we find that our linewidths are about 40% narrower than their linewidths (i.e. there is an offset between the two sets of parameters). A similar offset is as expected also observed in the mode heights. These values for the linewidths and heights are, however, still within 3σ, three times the combined uncertainty in quadrature. By comparing the linewidths obtained by Vrard et al. (2018) and Kallinger (2019), we also observe that the linewidths in Vrard et al. (2018) are systematically broader. Our results are overall in agreement with the values from Vrard et al. (2018) for the

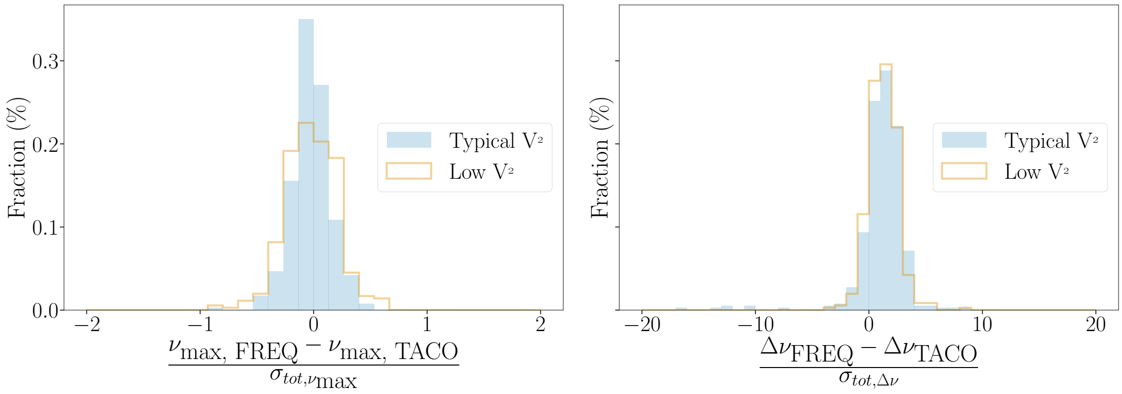

Figure A.4: Same as in Fig. A.3, but now for S_p (blue).

stars present in both samples. Our distributions of our radial-mode parameters are therefore consistent with the distributions obtained with the values of Vrard et al. (2018) and Kallinger (2019) for the stars we have in common.

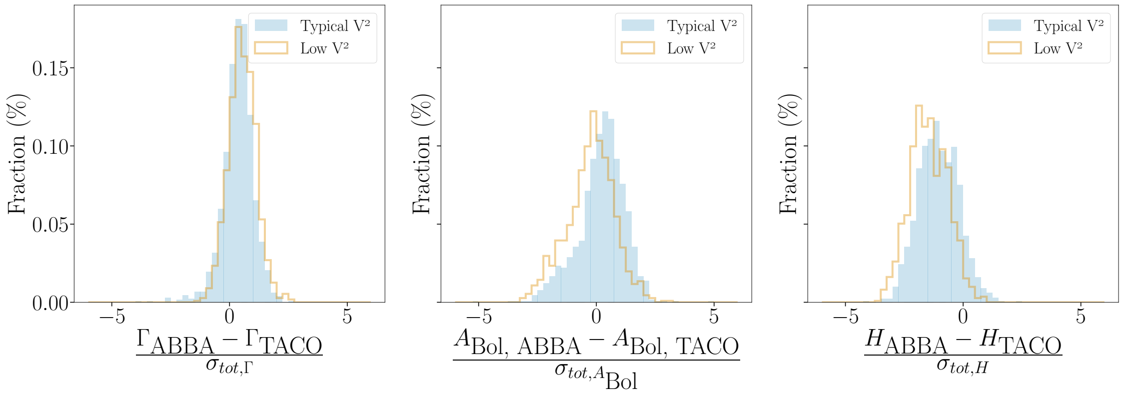

Figure A.5: Difference between the linewidths (left), bolometric amplitudes (middle), and heights (right) based on our results and the Kallinger (2019) data for stars in the low-visibility sample (orange) and S_c (blue).

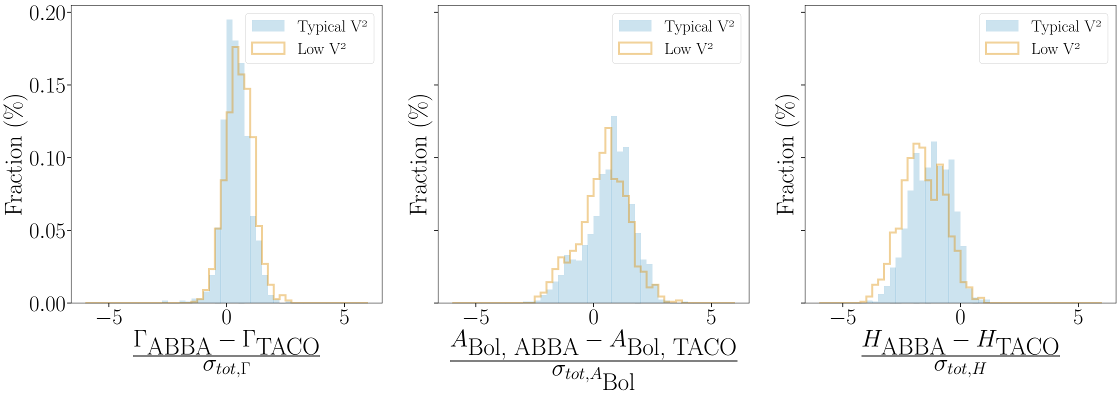

Figure A.6: Same as in Fig. A.5, but now for S_p (blue).

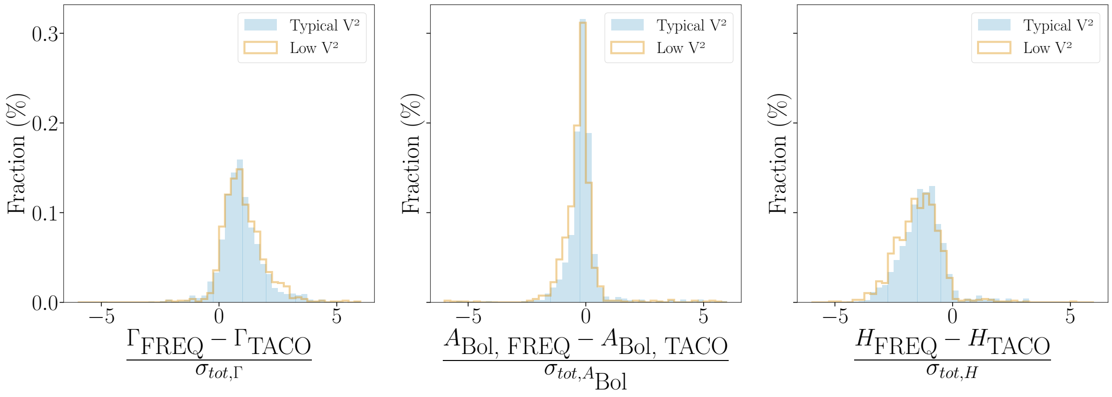

Figure A.7: Same as in Fig. A.5, but now for the comparison with the FREQ results (Vrard et al., 2018).

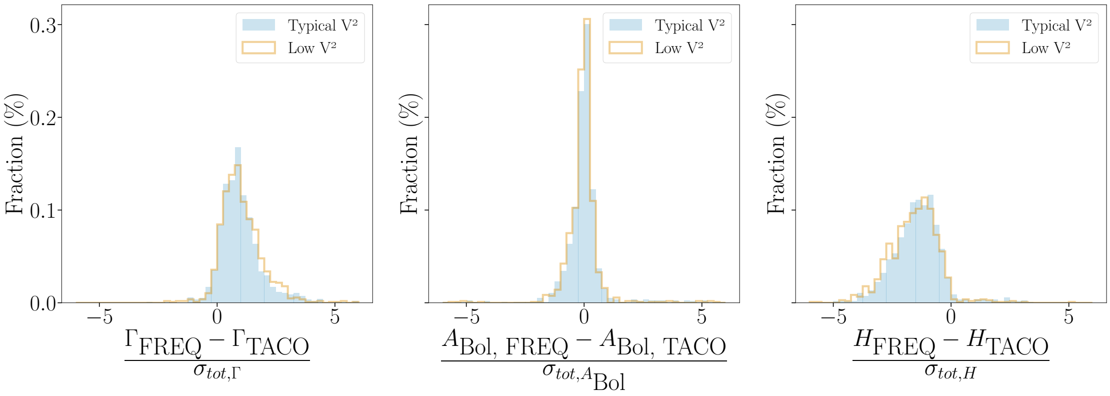

Figure A.8: Same as in A.7, but now for S_p (blue).

B

Appendices for Chapter 3: Full and partial dissipation of g-mode character in the non-radial modes of suppressed dipole-mode stars

B.1. Comparison of visibility measurements with literature

In this section, we compare the visibility measurements computed in this study to the visibility measurements found in the literature. The main difference in our approach is that we use fitted amplitudes instead of amplitudes obtained by integrating the PDS over specific frequency ranges (see Stello et al., 2016b; Mosser et al., 2017a, for more information). For this comparison, we compute the absolute value of difference between their and our visibility measurements Δv_l in units of the combined uncertainty on the measurements. We note that we take an uncertainty of 10% on the measurements from (Stello et al., 2016b; Mosser et al., 2017a) as no specific uncertainty is mentioned. This chosen uncertainty is in line with the reported typical uncertainties. We consider agreement between the measurements if the ratio of the difference to the combined uncertainty is smaller than three.

Only one star we have in common with the sample of Mosser et al. (2017a) has significantly different dipole-mode visibility (see Fig. B.1). We also find that our results for the dipole-mode visibility are in agreement with the values from Stello et al. (2016b) for about 95% of the stars we have in common with their sample. The few stars for which we don't find agreement seem to have a high noise level in their PDS or a negative visibility measurement in the literature (see e.g. Stello et al., 2016b). The high noise level will contribute to a larger dipole-mode visibility (i.e. the noise contribution is integrated together with the contribution of the modes). According toStello et al. (2016b) their negative visibility measurements are due to their background determination. A too large background model will indeed result in a negative contribution to the integral computed to obtain the mode amplitudes. Our measurements and the associated uncertainties for these stars are often small leading to large differences in uncertainty units (see stars with $\Delta v_1/\sigma_1$ around 5 and 8 in Fig. B.1).

Our quadrupole-mode visibility measurements are in agreement with the measurements of Stello et al. (2016b) (see Fig. B.2). We conclude from this comparison that our measurements are comparable to the measurements presented in the literature.

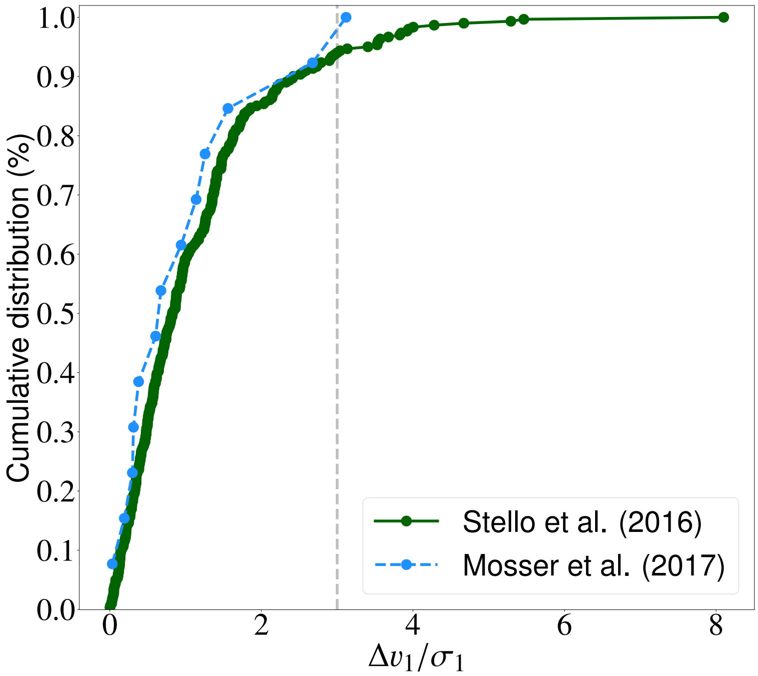

Figure B.1: Cumulative distribution of the difference between the dipole-mode visibilities Δv_1 based on our results and the data of Stello et al. (2016b) (green) and Mosser et al. (2017a) (blue) in units of combined uncertainty σ_1. The grey dashed line indicates the 3-sigma acceptance limit.

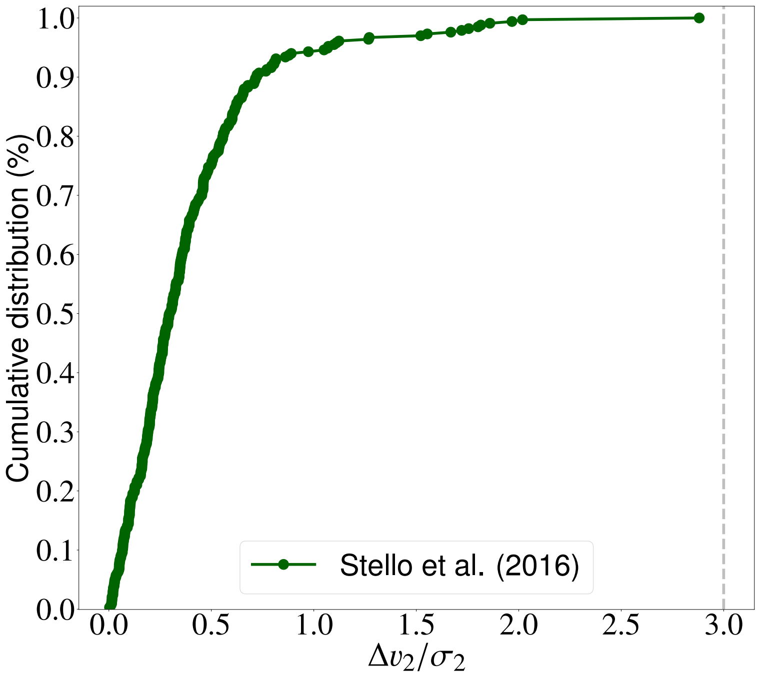

Figure B.2: Same as Fig. B.1, now for the quadrupole-mode visibility measurements.

List of publications

Papers used in this thesis:

[1] **Coppée, Q.**; Müller, J.; Bazot, M.; Hekker, S.; 2024; **A&A, 690 A324**; *The radial modes of stars with suppressed dipole modes*

[2] **Coppée, Q.**; Müller, J.; Choi, J. Y.; Hekker, S.; submitted to A&A; *Full and partial dissipation of the g-mode character in the non-radial modes of suppressed dipole-mode stars*

[3] **Coppée, Q.**; Müller, J.; Hekker, S.; soon to be submitted; *Magnetic shift and mode suppression in non-radial modes of red giants*

Papers not used in this thesis:

[1] Müller, J. ; **Coppée, Q.** ; Hekker, S.; 2024; **A&A, 696 A134**; *Oscillations of red giant stars with magnetic damping in the core: I. Dissipation of mode energy in dipole-like magnetic fields*

[2] Choi, J. Y.; Espinoza-Rojas, F.; **Coppée, Q.** ; Hekker, S.; submitted to A&A; *Power density spectra morphologies of seismically unresolved red-giant asteroseismic binaries*

[3] Kluska, J. ; Van Winckel, H. ; **Coppée, Q.** ; Oomen, G. -M. ; Dsilva, K. ; Kamath, D. ; Bujarrabal, V. ; Min, M. ; 2022; **A&A, 658 A36**; *A population of transition disks around evolved stars: Fingerprints of planets. Catalog of disks surrounding Galactic post-AGB binaries*

Bibliography

Abdurro'uf, Accetta, K., Aerts, C., Silva Aguirre, V., Ahumada, R., Ajgaonkar, N., Filiz Ak, N., Alam, S., Allende Prieto, C., Almeida, A., et al., "The Seventeenth Data Release of the Sloan Digital Sky Surveys: Complete Release of MaNGA, MaStar, and APOGEE-2 Data," *The Astrophysical Journal Supplement Series*, vol. 259, no. 2, 35, 2022, doi:10.3847/1538-4365/ac4414.

Aerts, C., Christensen-Dalsgaard, J., and Kurtz, D. W., *Asteroseismology*, Springer Dordrecht, 2010, doi:10.1007/978-1-4020-5803-5.

Arentoft, T., Brogaard, K., Jessen-Hansen, J., Silva Aguirre, V., Kjeldsen, H., Mosumgaard, J. R., and Sandquist, E. L., "Convective-core Overshoot and Suppression of Oscillations: Constraints from Red Giants in NGC 6811," *Astrophysical Journal*, vol. 838, no. 2, 115, 2017, doi:10.3847/1538-4357/aa63f7.

Baglin, A., Auvergne, M., Boisnard, L., Lam-Trong, T., Barge, P., Catala, C., Deleuil, M., Michel, E., and Weiss, W., "CoRoT: a high precision photometer for stellar ecolution and exoplanet finding," in "36th COSPAR Scientific Assembly," vol. 36, p. 3749, 2006.

Ballot, J., Barban, C., and van't Veer-Menneret, C., "Visibilities and bolometric corrections for stellar oscillation modes observed by Kepler," *Astronomy & Astrophysics*, vol. 531, A124, 2011, doi:10.1051/0004-6361/201016230.

Balmforth, N. J., "Solar pulsational stability - III. Acoustical excitation by turbulent convection," *Monthly Notices of the Royal Astronomical Society*, vol. 255, p. 639, 1992, doi:10.1093/mnras/255.4.639.

Basu, S. and Chaplin, W. J., *Asteroseismic Data Analysis. Foundations and Techniques*, Princeton University Press, 2018.

Beck, P. G., Bedding, T. R., Mosser, B., Stello, D., Garcia, R. A., Kallinger, T., Hekker, S., Elsworth, Y., Frandsen, S., Carrier, F., et al., "Kepler Detected Gravity-Mode Period Spacings in a Red Giant Star," *Science*, vol. 332, no. 6026, p. 205, 2011, doi:10.1126/science.1201939.

Beck, P. G., Mathis, S., Kallinger, T., García, R. A., and Benbakoura, M., "Observations of tides and circularization in red-giant binaries from Kepler photometry," in "EAS Publications Series," *EAS Publications Series*, vol. 82, pp. 119–125, 2019, doi:10.1051/eas/1982012.

Bedding, T. R., Mosser, B., Huber, D., Montalbán, J., Beck, P., Christensen-Dalsgaard, J., Elsworth, Y. P., García, R. A., Miglio, A., Stello, D., et al., "Gravity modes as a way to distinguish between hydrogen- and helium-burning red giant stars," *Nature*, vol. 471, no. 7340, pp. 608–611, 2011, doi:10.1038/nature09935.

Benomar, O., Belkacem, K., Bedding, T. R., Stello, D., Di Mauro, M. P., Ventura, R., Mosser, B., Goupil, M. J., Samadi, R., and Garcia, R. A., "Asteroseismology of Evolved Stars with Kepler: A New Way to Constrain Stellar Interiors Using Mode Inertias," *The Astrophysical Journal Letters*, vol. 781, no. 2, L29, 2014, doi:10.1088/2041-8205/781/2/L29.

Blanton, M. R., Bershady, M. A., Abolfathi, B., Albareti, F. D., Allende Prieto, C., Almeida, A., Alonso-García, J., Anders, F., Anderson, S. F., Andrews, B., et al., "Sloan Digital Sky Survey IV: Mapping the Milky Way, Nearby Galaxies, and the Distant Universe," *The Astronomical Journal*, vol. 154, no. 1, 28, 2017, doi:10.3847/1538-3881/aa7567.

Borucki, W. J., Koch, D., Basri, G., Batalha, N., Brown, T., Caldwell, D., Caldwell, J., Christensen-Dalsgaard, J., Cochran, W. D., DeVore, E., et al., "Kepler Planet-Detection Mission: Introduction and First Results," *Science*, vol. 327, no. 5968, p. 977, 2010, doi:10.1126/science.1185402.

Bowman, D. M., Burssens, S., Simón-Díaz, S., Edelmann, P. V. F., Rogers, T. M., Horst, L., Röpke, F. K., and Aerts, C., "Photometric detection of internal gravity waves in upper main-sequence stars. II. Combined TESS photometry and high-resolution spectroscopy," *Astronomy & Astrophysics*, vol. 640, A36, 2020, doi:10.1051/0004-6361/202038224.

Brown, T. M., Gilliland, R. L., Noyes, R. W., and Ramsey, L. W., "Detection of Possible p-Mode Oscillations on Procyon," *Astrophysical Journal*, vol. 368, p. 599, 1991, doi:10.1086/169725.

Bugnet, L., "Magnetic signatures on mixed-mode frequencies. II. Period spacings as a probe of the internal magnetism of red giants," *Astronomy & Astrophysics*, vol. 667, A68, 2022, doi:10.1051/0004-6361/202243167.

Bugnet, L., Das, S. B., and Einramhof, L., "Unveiling complex magnetic field configurations in red-giant stars," in "8th TESS/15th Kepler Asteroseismic Science Consortium Workshop," p. 65, 2024, doi:10.5281/zenodo.13373924.

Bugnet, L., Prat, V., Mathis, S., Astoul, A., Augustson, K., García, R. A., Mathur, S., Amard, L., and Neiner, C., "Magnetic signatures on mixed-mode frequencies. I. An axisymmetric fossil field inside the core of red giants," *Astronomy & Astrophysics*, vol. 650, A53, 2021, doi:10.1051/0004-6361/202039159.

Cantiello, M., Fuller, J., and Bildsten, L., "Asteroseismic Signatures of Evolving Internal Stellar Magnetic Fields," *Astrophysical Journal*, vol. 824, no. 1, 14, 2016, doi:10.3847/0004-637X/824/1/14.

Chaplin, W. J., Bedding, T. R., Bonanno, A., Broomhall, A. M., García, R. A., Hekker, S., Huber, D., Verner, G. A., Basu, S., Elsworth, Y., et al., "Evidence for the Impact of Stellar Activity on the Detectability of Solar-like Oscillations Observed by Kepler," *The Astrophysical Journal Letters*, vol. 732, no. 1, L5, 2011, doi:10.1088/2041-8205/732/1/L5.

Chaplin, W. J. and Miglio, A., "Asteroseismology of Solar-Type and Red-Giant Stars," *Annual Review of Astronomy and Astrophysics*, vol. 51, no. 1, pp. 353–392, 2013, doi:10.1146/annurev-astro-082812-140938.

Christensen-Dalsgaard, J. and Gough, D. O., "Towards a heliological inverse problem," *Nature*, vol. 259, no. 5539, pp. 89–92, 1976, doi:10.1038/259089a0.

Coppée, Q., Müller, J., Bazot, M., and Hekker, S., "The radial modes of stars with suppressed dipole modes," *Astronomy & Astrophysics*, vol. 690, A324, 2024, doi:10.1051/0004-6361/202450037.

De Ridder, J., Barban, C., Baudin, F., Carrier, F., Hatzes, A. P., Hekker, S., Kallinger, T., Weiss, W. W., Baglin, A., Auvergne, M., et al., "Non-radial oscillation modes with long lifetimes in giant stars," *Nature*, vol. 459, no. 7245, pp. 398–400, 2009, doi:10.1038/nature08022.

Deheuvels, S., "Seismic constraints on magnetic fields inside stars," , 2024, doi:10.5281/zenodo.13373930.

Deheuvels, S., Ballot, J., Beck, P. G., Mosser, B., Østensen, R., García, R. A., and Goupil, M. J., "Seismic evidence for a weak radial differential rotation in intermediate-mass core helium burning stars," *Astronomy & Astrophysics*, vol. 580, A96, 2015, doi:10.1051/0004-6361/201526449.

Deheuvels, S., Doğan, G., Goupil, M. J., Appourchaux, T., Benomar, O., Bruntt, H., Campante, T. L., Casagrande, L., Ceillier, T., Davies, G. R., et al., "Seismic constraints on the radial dependence of the internal rotation profiles of six Kepler subgiants and young red giants," *Astronomy & Astrophysics*, vol. 564, A27, 2014, doi:10.1051/0004-6361/201322779.

Deheuvels, S., Li, G., Ballot, J., and Lignières, F., "Strong magnetic fields detected in the cores of 11 red giant stars using gravity-mode period spacings," *Astronomy & Astrophysics*, vol. 670, L16, 2023, doi:10.1051/0004-6361/202245282.

Dupret, M. A., Belkacem, K., Samadi, R., Montalban, J., Moreira, O., Miglio, A., Godart, M., Ventura, P., Ludwig, H. G., Grigahcène, A., et al., "Theoretical amplitudes and lifetimes of non-radial solar-like oscillations in red giants," *Astronomy & Astrophysics*, vol. 506, no. 1, pp. 57–67, 2009, doi:10.1051/0004-6361/200911713.

Eddington, A. S., *The Internal Constitution of the Stars*, 1926.

Elsworth, Y., Hekker, S., Johnson, J. A., Kallinger, T., Mosser, B., Pinsonneault, M., Hon, M., Kuszlewicz, J., Miglio, A., Serenelli, A., et al., "Insights from the APOKASC determination of the evolutionary state of red-giant stars by consolidation of different methods," *Monthly Notices of the Royal Astronomical Society*, vol. 489, no. 4, pp. 4641–4657, 2019, doi:10.1093/mnras/stz2356.

Fuller, J., Cantiello, M., Stello, D., Garcia, R. A., and Bildsten, L., “Asteroseismology can reveal strong internal magnetic fields in red giant stars,” *Science*, vol. 350, no. 6259, pp. 423–426, 2015, doi:10.1126/science.aac6933.

Fuller, J., Piro, A. L., and Jermyn, A. S., “Slowing the spins of stellar cores,” *Monthly Notices of the Royal Astronomical Society*, vol. 485, no. 3, pp. 3661–3680, 2019, doi:10.1093/mnras/stz514.

García, R. A. and Ballot, J., “Asteroseismology of solar-type stars,” *Living Reviews in Solar Physics*, vol. 16, no. 1, 4, 2019, doi:10.1007/s41116-019-0020-1.

García, R. A., Pérez Hernández, F., Benomar, O., Silva Aguirre, V., Ballot, J., Davies, G. R., Doğan, G., Stello, D., Christensen-Dalsgaard, J., Houdek, G., et al., “Study of KIC 8561221 observed by Kepler: an early red giant showing depressed dipolar modes,” *Astronomy & Astrophysics*, vol. 563, A84, 2014, doi:10.1051/0004-6361/201322823.

García Saravia Ortiz de Montellano, A., Hekker, S., and Themeßl, N., “Automated asteroseismic peak detections,” *Monthly Notices of the Royal Astronomical Society*, vol. 476, no. 2, pp. 1470–1496, 2018, doi:10.1093/mnras/sty253.

Gaulme, P., Jackiewicz, J., Appourchaux, T., and Mosser, B., “Surface Activity and Oscillation Amplitudes of Red Giants in Eclipsing Binaries,” *Astrophysical Journal*, vol. 785, no. 1, 5, 2014, doi:10.1088/0004-637X/785/1/5.

Gehan, C., Mosser, B., Michel, E., Samadi, R., and Kallinger, T., “Core rotation braking on the red giant branch for various mass ranges,” *Astronomy & Astrophysics*, vol. 616, A24, 2018, doi:10.1051/0004-6361/201832822.

Gizon, L. and Solanki, S. K., “Determining the Inclination of the Rotation Axis of a Sun-like Star,” *Astrophysical Journal*, vol. 589, no. 2, pp. 1009–1019, 2003, doi:10.1086/374715.

Goldreich, P. and Keeley, D. A., “Solar seismology. II. The stochastic excitation of the solar p-modes by turbulent convection.” *Astrophysical Journal*, vol. 212, pp. 243–251, 1977, doi:10.1086/155043.

Goldreich, P. and Kumar, P., “The Interaction of Acoustic Radiation with Turbulence,” *Astrophysical Journal*, vol. 326, p. 462, 1988, doi:10.1086/166108.

Goupil, M. J., Mosser, B., Marques, J. P., Ouazzani, R. M., Belkacem, K., Lebreton, Y., and Samadi, R., “Seismic diagnostics for transport of angular momentum in stars. II. Interpreting observed rotational splittings of slowly rotating red giant stars,” *Astronomy & Astrophysics*, vol. 549, A75, 2013, doi:10.1051/0004-6361/201220266.

Grec, G., Fossat, E., and Pomerantz, M. A., “Full-Disk Observations of Solar Oscillations from the Geographic South-Pole - Latest Results,” , vol. 82, no. 1-2, pp. 55–66, 1983, doi:10.1007/BF00145545.

Hatt, E. J., Ong, J. M. J., Nielsen, M. B., Chaplin, W. J., Davies, G. R., Deheuvels, S., Ballot, J., Li, G., and Bugnet, L., “Asteroseismic signatures of core magnetism and rotation in hundreds of low-luminosity red giants,” *Monthly Notices of the Royal Astronomical Society*, vol. 534, no. 2, pp. 1060–1076, 2024, doi:10.1093/mnras/stae2053.

Hekker, S., "Scaling relations for solar-like oscillations: a review," *Frontiers in Astronomy and Space Sciences*, vol. 7, 3, 2020, doi:10.3389/fspas.2020.00003.

Hekker, S., Aerts, C., De Ridder, J., and Carrier, F., "Pulsations detected in the line profile variations of red giants. Modelling of line moments, line bisector and line shape," *Astronomy & Astrophysics*, vol. 458, no. 3, pp. 931–940, 2006, doi:10.1051/0004-6361:20065755.

Hekker, S., Angelou, G. C., Elsworth, Y., and Basu, S., "Mirror principle and the red-giant bump: the battle of entropy in low-mass stars," *Monthly Notices of the Royal Astronomical Society*, vol. 492, no. 4, pp. 5940–5948, 2020, doi:10.1093/mnras/staa176.

Hekker, S. and Christensen-Dalsgaard, J., "Giant star seismology," *The Astronomy and Astrophysics Review*, vol. 25, no. 1, 1, 2017, doi:10.1007/s00159-017-0101-x.

Hekker, S., Elsworth, Y., and Angelou, G. C., "Gravity mode offset and properties of the evanescent zone in red-giant stars," *Astronomy & Astrophysics*, vol. 610, A80, 2018, doi:10.1051/0004-6361/201731264.

Hekker, S., Kallinger, T., Baudin, F., De Ridder, J., Barban, C., Carrier, F., Hatzes, A. P., Weiss, W. W., and Baglin, A., "Characteristics of solar-like oscillations in red giants observed in the CoRoT exoplanet field," *Astronomy & Astrophysics*, vol. 506, no. 1, pp. 465–469, 2009, doi:10.1051/0004-6361/200911858.

Hodges, J. L., "The significance probability of the smirnov two-sample test," *Arkiv for Matematik*, vol. 3, no. 5, pp. 469–486, 1958, doi:10.1007/BF02589501.

Hon, M., Li, Y., and Ong, J., "Flow-Based Generative Emulation of Grids of Stellar Evolutionary Models," *arXiv e-prints*, arXiv:2407.09427, 2024, doi:10.48550/arXiv.2407.09427.

Houdek, G., Balmforth, N. J., Christensen-Dalsgaard, J., and Gough, D. O., "Amplitudes of stochastically excited oscillations in main-sequence stars," *Astronomy & Astrophysics*, vol. 351, pp. 582–596, 1999, doi:10.48550/arXiv.astro-ph/9909107.

Ivanov, P. B., Papaloizou, J. C. B., and Chernov, S. V., "A unified normal mode approach to dynamic tides and its application to rotating Sun-like stars," *Monthly Notices of the Royal Astronomical Society*, vol. 432, no. 3, pp. 2339–2365, 2013, doi:10.1093/mnras/stt595.

Jermyn, A. S., Bauer, E. B., Schwab, J., Farmer, R., Ball, W. H., Bellinger, E. P., Dotter, A., Joyce, M., Marchant, P., Mombarg, J. S. G., et al., "Modules for Experiments in Stellar Astrophysics (MESA): Time-dependent Convection, Energy Conservation, Automatic Differentiation, and Infrastructure," *The Astrophysical Journal Supplement Series*, vol. 265, no. 1, 15, 2023, doi:10.3847/1538-4365/acae8d.

Kallinger, T., "Release note: Massive peak bagging of red giants in the Kepler field," *arXiv e-prints*, arXiv:1906.09428, 2019.

Kallinger, T., De Ridder, J., Hekker, S., Mathur, S., Mosser, B., Gruberbauer, M., García, R. A., Karoff, C., and Ballot, J., "The connection between stellar granulation and oscillation as seen by the Kepler mission," *Astronomy & Astrophysics*, vol. 570, A41, 2014, doi:10.1051/0004-6361/201424313.

Kallinger, T., Hekker, S., Mosser, B., De Ridder, J., Bedding, T. R., Elsworth, Y. P., Gruberbauer, M., Guenther, D. B., Stello, D., Basu, S., et al., "Evolutionary influences on the structure of red-giant acoustic oscillation spectra from 600d of Kepler observations," *Astronomy & Astrophysics*, vol. 541, A51, 2012, doi:10.1051/0004-6361/201218854.

Kippenhahn, R., Weigert, A., and Weiss, A., *Stellar Structure and Evolution*, Springer Berlin, Heidelberg, 2013, doi:10.1007/978-3-642-30304-3.

Kjeldsen, H. and Bedding, T. R., "Amplitudes of stellar oscillations: the implications for asteroseismology." *Astronomy & Astrophysics*, vol. 293, pp. 87–106, 1995.

Koch, D. G., Borucki, W. J., Basri, G., Batalha, N. M., Brown, T. M., Caldwell, D., Christensen-Dalsgaard, J., Cochran, W. D., DeVore, E., Dunham, E. W., et al., "KEPLER MISSION DESIGN, REALIZED PHOTOMETRIC PERFORMANCE, AND EARLY SCIENCE," *The Astrophysical Journal Letters*, vol. 713, no. 2, p. L79, 2010, doi:10.1088/2041-8205/713/2/L79.

Kuhn, H. W., "The Hungarian method for the assignment problem," *Naval research logistics quarterly*, vol. 2, no. 1-2, pp. 83–97, 1955.

Kuhn, H. W., "Variants of the Hungarian method for assignment problems," *Naval research logistics quarterly*, vol. 3, no. 4, pp. 253–258, 1956.

Kuszlewicz, J. S., Chaplin, W. J., North, T. S. H., Farr, W. M., Bell, K. J., Davies, G. R., Campante, T. L., and Hekker, S., "Bayesian hierarchical inference of asteroseismic inclination angles," *Monthly Notices of the Royal Astronomical Society*, vol. 488, no. 1, pp. 572–589, 2019, doi:10.1093/mnras/stz1689.

Lecoanet, D., Vasil, G. M., Fuller, J., Cantiello, M., and Burns, K. J., "Conversion of internal gravity waves into magnetic waves," *Monthly Notices of the Royal Astronomical Society*, vol. 466, no. 2, pp. 2181–2193, 2017, doi:10.1093/mnras/stw3273.

Li, G., Deheuvels, S., Ballot, J., and Lignières, F., "Magnetic fields of 30 to 100 kG in the cores of red giant stars," *Nature*, vol. 610, no. 7930, pp. 43–46, 2022, doi:10.1038/s41586-022-05176-0.

Li, G., Deheuvels, S., Li, T., Ballot, J., and Lignières, F., "Internal magnetic fields in 13 red giants detected by asteroseismology," *Astronomy & Astrophysics*, vol. 680, A26, 2023, doi:10.1051/0004-6361/202347260.

Loi, S. T., "Magneto-gravity wave packet dynamics in strongly magnetized cores of evolved stars," *Monthly Notices of the Royal Astronomical Society*, vol. 493, no. 4, pp. 5726–5742, 2020, doi:10.1093/mnras/staa581.

Loi, S. T. and Papaloizou, J. C. B., "Torsional Alfv9n resonances as an efficient damping mechanism for non-radial oscillations in red giant stars," *Monthly Notices of the Royal Astronomical Society*, vol. 467, no. 3, pp. 3212–3225, 2017, doi:10.1093/mnras/stx281.

Loi, S. T. and Papaloizou, J. C. B., "Effects of a strong magnetic field on internal gravity waves: trapping, phase mixing, reflection, and dynamical chaos," *Monthly Notices of the Royal Astronomical Society*, vol. 477, no. 4, pp. 5338–5357, 2018, doi:10.1093/mnras/sty917.

Mathis, S., Bugnet, L., Prat, V., Augustson, K., Mathur, S., and Garcia, R. A., "Probing the internal magnetism of stars using asymptotic magneto-asteroseismology," *Astronomy & Astrophysics*, vol. 647, A122, 2021, doi:10.1051/0004-6361/202039180.

Michel, E., Baglin, A., Auvergne, M., Catala, C., Aerts, C., Alecian, G., Amado, P., Appourchaux, T., Ausseloos, M., Ballot, J., et al., "The Seismology Programme of CoRoT," in Fridlund, M., Baglin, A., Lochard, J., and Conroy, L. (editors), "The CoRoT Mission Pre-Launch Status - Stellar Seismology and Planet Finding," *ESA Special Publication*, vol. 1306, p. 39, 2006, doi:10.48550/arXiv.0811.1080.

Mosser, B., Barban, C., Montalbán, J., Beck, P. G., Miglio, A., Belkacem, K., Goupil, M. J., Hekker, S., De Ridder, J., Dupret, M. A., et al., "Mixed modes in red-giant stars observed with CoRoT," *Astronomy & Astrophysics*, vol. 532, A86, 2011a, doi:10.1051/0004-6361/201116825.

Mosser, B., Belkacem, K., Goupil, M. J., Michel, E., Elsworth, Y., Barban, C., Kallinger, T., Hekker, S., De Ridder, J., Samadi, R., et al., "The universal red-giant oscillation pattern. An automated determination with CoRoT data," *Astronomy & Astrophysics*, vol. 525, L9, 2011b, doi:10.1051/0004-6361/201015440.

Mosser, B., Belkacem, K., Pinçon, C., Takata, M., Vrard, M., Barban, C., Goupil, M. J., Kallinger, T., and Samadi, R., "Dipole modes with depressed amplitudes in red giants are mixed modes," *Astronomy & Astrophysics*, vol. 598, A62, 2017a, doi:10.1051/0004-6361/201629494.

Mosser, B., Elsworth, Y., Hekker, S., Huber, D., Kallinger, T., Mathur, S., Belkacem, K., Goupil, M. J., Samadi, R., Barban, C., et al., "Characterization of the power excess of solar-like oscillations in red giants with Kepler," *Astronomy & Astrophysics*, vol. 537, A30, 2012, doi:10.1051/0004-6361/20111735210.1086/141952.

Mosser, B., Gehan, C., Belkacem, K., Samadi, R., Michel, E., and Goupil, M. J., "Period spacings in red giants. IV. Toward a complete description of the mixed-mode pattern," *Astronomy & Astrophysics*, vol. 618, A109, 2018, doi:10.1051/0004-6361/201832777.

Mosser, B., Michel, E., Belkacem, K., Goupil, M. J., Baglin, A., Barban, C., Provost, J., Samadi, R., Auvergne, M., and Catala, C., "Asymptotic and measured large frequency separations," *Astronomy & Astrophysics*, vol. 550, A126, 2013, doi:10.1051/0004-6361/201220435.

Mosser, B., Pinçon, C., Belkacem, K., Takata, M., and Vrard, M., "Period spacings in red giants. III. Coupling factors of mixed modes," *Astronomy & Astrophysics*, vol. 600, A1, 2017b, doi:10.1051/0004-6361/201630053.

Mosser, B., Vrard, M., Belkacem, K., Deheuvels, S., and Goupil, M. J., "Period spacings in red giants. I. Disentangling rotation and revealing core structure discontinuities," *Astronomy & Astrophysics*, vol. 584, A50, 2015, doi:10.1051/0004-6361/201527075.

Müller, J., Coppée, Q., and Hekker, S., "Oscillations of red giant stars with magnetic damping in the core: I. Dissipation of mode energy in dipole-like magnetic fields," *Astronomy & Astrophysics*, vol. 696, A134, 2025, doi:10.1051/0004-6361/202553888.

Munkres, J., "Algorithms for the Assignment and Transportation Problems," *Journal of the Society for Industrial and Applied Mathematics*, vol. 5, no. 1, pp. 32–38, 1957, doi:10.1137/0105003.

Ong, J. M. J. and Basu, S., "Explaining Deviations from the Scaling Relationship of the Large Frequency Separation," *Astrophysical Journal*, vol. 870, no. 1, 41, 2019, doi:10.3847/1538-4357/aaf1b5.

Paxton, B., Bildsten, L., Dotter, A., Herwig, F., Lesaffre, P., and Timmes, F., "Modules for Experiments in Stellar Astrophysics (MESA)," *The Astrophysical Journal Supplement Series*, vol. 192, no. 1, 3, 2011, doi:10.1088/0067-0049/192/1/3.

Paxton, B., Cantiello, M., Arras, P., Bildsten, L., Brown, E. F., Dotter, A., Mankovich, C., Montgomery, M. H., Stello, D., Timmes, F. X., et al., "Modules for Experiments in Stellar Astrophysics (MESA): Planets, Oscillations, Rotation, and Massive Stars," *The Astrophysical Journal Supplement Series*, vol. 208, no. 1, 4, 2013, doi:10.1088/0067-0049/208/1/4.

Paxton, B., Marchant, P., Schwab, J., Bauer, E. B., Bildsten, L., Cantiello, M., Dessart, L., Farmer, R., Hu, H., Langer, N., et al., "Modules for Experiments in Stellar Astrophysics (MESA): Binaries, Pulsations, and Explosions," *The Astrophysical Journal Supplement Series*, vol. 220, no. 1, 15, 2015, doi:10.1088/0067-0049/220/1/15.

Paxton, B., Schwab, J., Bauer, E. B., Bildsten, L., Blinnikov, S., Duffell, P., Farmer, R., Goldberg, J. A., Marchant, P., Sorokina, E., et al., "Modules for Experiments in Stellar Astrophysics (MESA): Convective Boundaries, Element Diffusion, and Massive Star Explosions," *The Astrophysical Journal Supplement Series*, vol. 234, no. 2, 34, 2018, doi:10.3847/1538-4365/aaa5a8.

Paxton, B., Smolec, R., Schwab, J., Gautschy, A., Bildsten, L., Cantiello, M., Dotter, A., Farmer, R., Goldberg, J. A., Jermyn, A. S., et al., "Modules for Experiments in Stellar Astrophysics (MESA): Pulsating Variable Stars, Rotation, Convective Boundaries, and Energy Conservation," *The Astrophysical Journal Supplement Series*, vol. 243, no. 1, 10, 2019, doi:10.3847/1538-4365/ab2241.

Pearson, K., "Contributions to the Mathematical Theory of Evolution. II. Skew Variation in Homogeneous Material," *Philosophical Transactions of the Royal Society of London Series A*, vol. 186, pp. 343–414, 1895, doi:10.1098/rsta.1895.0010.

Pinçon, C., Goupil, M. J., and Belkacem, K., "Probing the mid-layer structure of red giants. I. Mixed-mode coupling factor as a seismic diagnosis," *Astronomy & Astrophysics*, vol. 634, A68, 2020, doi:10.1051/0004-6361/201936864.

Pinsonneault, M. H., Elsworth, Y. P., Tayar, J., Serenelli, A., Stello, D., Zinn, J., Mathur, S., García, R. A., Johnson, J. A., Hekker, S., et al., "The Second APOKASC Catalog: The Empirical Approach," *The Astrophysical Journal Supplement Series*, vol. 239, no. 2, 32, 2018, doi:10.3847/1538-4365/aaebfd.

Pinsonneault, M. H., Elsworth, Y. P., Tayar, J., Serenelli, A., Stello, D., Zinn, J., Mathur, S., Garcia, R. A., Johnson, J. A., Hekker, S., et al., "VizieR Online Data Catalog: APOKASC-2 catalog of Kepler evolved stars (Pinsonneault+, 2018)," *VizieR Online Data Catalog*, J/ApJS/239/32, 2019.

Ricker, G. R., Winn, J. N., Vanderspek, R., Latham, D. W., Bakos, G. Á., Bean, J. L., Berta-Thompson, Z. K., Brown, T. M., Buchhave, L., Butler, N. R., et al., "Transiting Exoplanet Survey Satellite (TESS)," in Oschmann, J. M., Jr., Clampin, M., Fazio, G. G., and MacEwen, H. A. (editors), "Space Telescopes and Instrumentation 2014: Optical, Infrared, and Millimeter Wave," *Society of Photo-Optical Instrumentation Engineers (SPIE) Conference Series*, vol. 9143, p. 914320, 2014, doi:10.1117/12.2063489.

Rui, N. Z. and Fuller, J., "Asteroseismic fingerprints of stellar mergers," *Monthly Notices of the Royal Astronomical Society*, vol. 508, no. 2, pp. 1618–1631, 2021, doi:10.1093/mnras/stab2528.

Rui, N. Z. and Fuller, J., "Gravity waves in strong magnetic fields," *Monthly Notices of the Royal Astronomical Society*, vol. 523, no. 1, pp. 582–602, 2023, doi:10.1093/mnras/stad1424.

Samadi, R., Belkacem, K., and Sonoi, T., "Stellar oscillations - II - The non-adiabatic case," in "EAS Publications Series," *EAS Publications Series*, vol. 73-74, pp. 111–191, 2015, doi:10.1051/eas/1573003.

Samadi, R. and Goupil, M. J., "Excitation of stellar p-modes by turbulent convection. I. Theoretical formulation," *Astronomy & Astrophysics*, vol. 370, pp. 136–146, 2001, doi:10.1051/0004-6361:20010212.

Schneider, F. R. N., Ohlmann, S. T., Podsiadlowski, P., Röpke, F. K., Balbus, S. A., and Pakmor, R., "Long-term evolution of a magnetic massive merger product," *Monthly Notices of the Royal Astronomical Society*, vol. 495, no. 3, pp. 2796–2812, 2020, doi:10.1093/mnras/staa1326.

Schonhut-Stasik, J., Huber, D., Baranec, C., Lamman, C., Salama, M., Jensen-Clem, R., Duev, D. A., Riddle, R., Kulkarni, S. R., and Law, N. M., "ROBO-AO Kepler Asteroseismic Survey. II. Do Stellar Companions Inhibit Stellar Oscillations?" *Astrophysical Journal*, vol. 888, no. 1, 34, 2020, doi:10.3847/1538-4357/ab50c3.

Shannon, C. E., "A mathematical theory of communication," *The Bell System Technical Journal*, vol. 27, no. 3, pp. 379–423, 1948, doi:10.1002/j.1538-7305.1948.tb01338.x.

Shibahashi, H., "Modal Analysis of Stellar Nonradial Oscillations by an Asymptotic Method," *Publications of the Astronomical Society of Japan*, vol. 31, pp. 87–104, 1979.

Stello, D., Cantiello, M., Fuller, J., Garcia, R. A., and Huber, D., "Suppression of Quadrupole and Octupole Modes in Red Giants Observed by Kepler *," *Publications of the Astronomical Society of Australia*, vol. 33, e011, 2016b, doi:10.1017/pasa.2016.9.

Stello, D., Cantiello, M., Fuller, J., Huber, D., García, R. A., Bedding, T. R., Bildsten, L., and Silva Aguirre, V., "A prevalence of dynamo-generated magnetic fields in the cores of intermediate-mass stars," *Nature*, vol. 529, no. 7586, pp. 364–367, 2016a, doi:10.1038/nature16171.

Takata, M., "Physical formulation of mixed modes of stellar oscillations," *Publications of the Astronomical Society of Japan*, vol. 68, no. 6, 91, 2016, doi:10.1093/pasj/psw093.

Tassoul, M., “Asymptotic approximations for stellar nonradial pulsations.” *The Astrophysical Journal Supplement Series*, vol. 43, pp. 469–490, 1980, doi:10.1086/190678.

Themeßl, N., Hekker, S., and Elsworth, Y., “Presence of mixed modes in red giants in binary systems,” in “European Physical Journal Web of Conferences,” *European Physical Journal Web of Conferences*, vol. 160, p. 05009, 2017, doi:10.1051/epjconf/201716005009.

Themeßl, N., Hekker, S., Southworth, J., Beck, P. G., Pavlovski, K., Tkachenko, A., Angelou, G. C., Ball, W. H., Barban, C., Corsaro, E., et al., “Oscillating red giants in eclipsing binary systems: empirical reference value for asteroseismic scaling relation,” *Monthly Notices of the Royal Astronomical Society*, vol. 478, no. 4, pp. 4669–4696, 2018, doi:10.1093/mnras/sty1113.

Townsend, R. H. D. and Teitler, S. A., “GYRE: an open-source stellar oscillation code based on a new Magnus Multiple Shooting scheme,” *Monthly Notices of the Royal Astronomical Society*, vol. 435, no. 4, pp. 3406–3418, 2013, doi:10.1093/mnras/stt1533.

Ulrich, R. K., “Determination of Stellar Ages from Asteroseismology,” *The Astrophysical Journal Letters*, vol. 306, p. L37, 1986, doi:10.1086/184700.

Unno, W., Osaki, Y., Ando, H., Saio, H., and Shibahashi, H., *Nonradial oscillations of stars*, 1989.

Vrard, M., Kallinger, T., Mosser, B., Barban, C., Baudin, F., Belkacem, K., and Cunha, M. S., “Amplitude and lifetime of radial modes in red giant star spectra observed by Kepler,” *Astronomy & Astrophysics*, vol. 616, A94, 2018, doi:10.1051/0004-6361/201732477.

Vrard, M., Mosser, B., and Samadi, R., “Period spacings in red giants. II. Automated measurement,” *Astronomy & Astrophysics*, vol. 588, A87, 2016, doi:10.1051/0004-6361/201527259.

Weinberg, N. N. and Arras, P., “Nonlinear Mixed Modes in Red Giants,” *Astrophysical Journal*, vol. 873, no. 1, 67, 2019, doi:10.3847/1538-4357/ab0204.

Weinberg, N. N., Arras, P., and Pramanik, D., “Damping of Oscillations in Red Giants by Resonant Mode Coupling,” *Astrophysical Journal*, vol. 918, no. 2, 70, 2021, doi:10.3847/1538-4357/ac0fdd.

Yu, J., Huber, D., Bedding, T. R., Stello, D., Hon, M., Murphy, S. J., and Khanna, S., “Asteroseismology of 16,000 Kepler Red Giants: Global Oscillation Parameters, Masses, and Radii,” *The Astrophysical Journal Supplement Series*, vol. 236, no. 2, 42, 2018, doi:10.3847/1538-4365/aaaf74.

Acknowledgments

I want to thank my supervisor, Saskia Hekker, for giving me the opportunity to start my academic career with a doctorate in the field of asteroseismology. I would like to thank you for all advice and your help over the years. Your dedication to research is inspiring and challenged me to work to the best of my capabilities. You always make time for someone when they need it and that's something I'll consider implementing during the rest of my career.

Without them, there would simply be no great Theory and Observations of Stars group at HITS, and therefore I would like to thank you all, TOSsers, past and current members, that made me grow, learn, laugh, but most importantly that supported me all along these four years. We were able to develop an incredible group chemistry that makes it very hard, if almost impossible, to really leave the group.

I also cannot forget all the wonderful friends that I met on this amazing journey. During a doctorate there are ups and downs. The ups were enjoyable and the downs less painful thanks to you! You made sure that I enjoyed my time during my PhD as well as making me feel at home in Heidelberg. I really hope that we can keep in touch for a long time!

I would also like to thank four of my Belgian friends, members of the infamous IvS FanClub (Aaron, Cis, Jan and Silke). During each of our own PhDs, we were there for each other and we let each other know that we were not alone in this adventure. Hopelijk tot binnenkort en op nog vele momenten samen!

Je voudrais profiter de l'occasion pour remercier ma famille, et en particulier mes parents et mon frère, qui m'ont toujours soutenu et encouragé, m'ont aidé à me construire pour devenir qui je suis aujourd'hui. Je ne pourrai jamais vous rendre tout ce que vous m'avez donné, mais je ferai de mon mieux ! J'ai aussi une pensée pour mes grands-parents, même s'ils ne sont plus tous parmi nous. Ils m'ont chacun à leur façon inspiré à suivre mes rêves.